RADIATION OF SEISMIC SURFACE-WAVES FROM FINITE MOVING SOURCES

Thesis by

Ari Ben-Menahem

In Partial Fulfillment of the Requirements

For the Degree of

Doctor of Philosophy

California Institute of Technology

Pasadena, California

1961

ACKNOWLEDGEMENT

Grateful acknowledgment is made to my research director Prof. Frank Press for his constant help and valuable advice in accomplishing this study. I have also had the benefit of stimulating discussions of this work with Prof. H. Benioff, Dr. K. Aki and Dr. H. Honda. Acknowledgement is due to Mr. M. Nafi Toksoz for performing the experimental model work, to Mr. G. David Harkrider for valuable criticism, to Mr. W. Stewart Smith for help in the programming and to the Western Data Processing Center at U.C.L.A. for allowing computing facilities. The experimental part of this study would not have been possible without data from Prof. Benioff's strain seismometer. A Fellowship granted by Mr. Herbert E. Linden of Beverly Hills, California is gratefully acknowledged.

ABSTRACT

A theory is proposed for the propagation of seismic surface-waves from finite moving sources. The method consists of obtaining, in the first place, basic solutions for surface displacements from directional sources. These solutions are integrated to obtain the effect of a moving fault with arbitrary dip angle. Displacements are evaluated for Rayleigh and Love-waves, at long ranges. It is shown that the dimensions of the source and the speed of rupture play an important role in the wave-pattern and cannot be ignored whenever the dimensions of the source are of the order of the radiation's dominant wave-length. It is demonstrated how this theory may lead to a derivation of the velocity of rupture and the fault-length from seismic records of a single station. Evidence is furnished both from two-dimensional model experiments and the Chilean Earthquake of May 1960.

TABLE OF CONTENTS

CHAPTER I

RAYLEIGH-WAVES FROM FINITE MOVING SOURCES

1.1 Introduction

There is no doubt that seismic records carry information about the Earthquake-source, such as: its dimensions, the speed of rupture and other parameters of interest. The point-source model is not sufficient for these purposes and one has to consider the finiteness of the source if one wishes to be able to interpret details of amplitude variation on a seismogram. Early attempts in this direction were made by Lamb (1) and Sezawa (2). Sezawa studied an extended source in the form of an infinite sheet. His results are of little value to our case, since he derived his results for infinite plane of sources and no propagating disturbance.

Knopoff and Gilbert (3) used the powerful "Knopoff-De Hoop representation theorem" to obtain first motions of body-waves from a disturbance propagating along an infinite line. However, using their method for finite regions incorporates unsurmountable integrations, even for the simplest cases, which obviously renders the method ineffective, except for initial motions.

In this chapter we investigate the effect of the finiteness of the seismic focus on the Rayleigh-wave pattern. The

equations of motion are solved for an internal harmonic concentrated force which points in an arbitrary direction. A fault-plane is then realized by moving this source along a line with finite speed and integrating the Rayleigh-pole contribution across a finite rectangle with an arbitrary strike and dip. Displacements are evaluated for long ranges and expressions are obtained for strike-slip and dip-slip fault types. Attention is mainly focused on a dipole-type motion of a vertical strike-slip model for which displacement has been actually computed and the results transformed into the time domain. It is found that the finiteness of the source plays a dominant role in the wave pattern whenever the wave-length is of the order of the fault dimensions or when the time of rupture is of the order of the period. It is also found that azimuthal distribution of amplitudes in that range depends strongly on the dimensions of the source and that the energy radiated in the direction of motion may highly exceed the amount radiated in the opposite direction. Not all possible faulting models are studied, but the method used is readily applicable to any special case.

1.2 Integral representation of the displacements due to a horizontal force

Consider an elastic half-space with a coordinate system as shown in figure 1. At the point x=0, y=0, z=h,

we put a harmonic point-source of magnitude L which is a simple force pointing in the direction of the x-axis. Following a method given by Yanovskaya (4) we describe this source in the form of a double Fourier-integral (5)

$$P_{xz} = \frac{L}{2\pi} e^{i\omega t} \int_{-\infty}^{\infty} \int_{-\infty}^{\infty} e^{i(\xi x + \eta y)} \, d\xi \, d\eta$$

(1-1)
$$P_{yz} = 0$$

$$P_{zz} = 0$$

To evaluate the displacement-field over the free surface of the half-space we have to solve the wave equations:

(1-2)
$$\nabla^2 \phi_i = \frac{1}{\alpha^2} \frac{\partial^2 \phi_i}{\partial t^2}$$

$$\nabla^2 \vec{\Psi}_i = \frac{1}{\beta^2} \frac{\partial^2 \vec{\Psi}_i}{\partial t^2} \qquad i = 1,2$$

where ϕ is the dilatation potential, $\vec{\Psi}(\Psi^{(x)}, \Psi^{(y)}, \Psi^{(z)})$ is the shear potential and the subscripts 1, 2 refer to the region above and below the source, respectively. We shall seek solutions of the form:

$$\left.\begin{aligned}
\phi_1 &= \frac{L}{2\pi} e^{i\omega t} \int_{-\infty}^{\infty}\int_{-\infty}^{\infty} \left(A_1 ch\,\gamma z + B_1 sh\,\gamma z\right) e^{i(sx+qy)}\, ds\, dq \\
\psi_1^{(x)} &= \frac{L}{2\pi} e^{i\omega t} \int_{-\infty}^{\infty}\int_{-\infty}^{\infty} \left(C_1^{(x)} ch\,\gamma' z + D_1^{(x)} sh\,\gamma' z\right) e^{i(sx+qy)}\, ds\, dq \\
\psi_1^{(y)} &= \frac{L}{2\pi} e^{i\omega t} \int_{-\infty}^{\infty}\int_{-\infty}^{\infty} \left(C_1^{(y)} ch\,\gamma' z + D_1^{(y)} sh\,\gamma' z\right) e^{i(sx+qy)}\, ds\, dq
\end{aligned}\right\} \quad z<h$$

$$\psi_1^{(z)} = 0$$

(1-3)

$$\left.\begin{aligned}
\phi_2 &= \frac{L}{2\pi} e^{i\omega t} \int_{-\infty}^{\infty}\int_{-\infty}^{\infty} A_2\, e^{-\nu z + i(sx+qy)}\, ds\, dq \\
\psi_2^{(x)} &= \frac{L}{2\pi} e^{i\omega t} \int_{-\infty}^{\infty}\int_{-\infty}^{\infty} C_2^{(x)} e^{-\nu' z + i(sx+qy)}\, ds\, dq \\
\psi_2^{(y)} &= \frac{L}{2\pi} e^{i\omega t} \int_{-\infty}^{\infty}\int_{-\infty}^{\infty} C_2^{(y)} e^{-\nu' z + i(sx+qy)}\, ds\, dq
\end{aligned}\right\} \quad z>h$$

$$\psi_2^{(z)} = 0 \qquad ; \quad \nu^2 = s^2+q^2-\kappa_\alpha^2 \qquad ; \quad \nu'^2 = s^2+q^2-\kappa_\beta^2$$

The displacements above the source are expressed in terms of these potentials (6):

$$u_x = \frac{\partial \phi_1}{\partial x} - \frac{\partial \psi_1^{(y)}}{\partial z} \tag{1-4}$$

$$u_y = \frac{\partial \phi_1}{\partial y} + \frac{\partial \psi^{(x)}}{\partial z} \tag{1-5}$$

$$u_z = \frac{\partial \phi_1}{\partial z} + \frac{\partial \psi^{(y)}}{\partial x} - \frac{\partial \psi^{(x)}}{\partial y} \tag{1-6}$$

Likewise, the stresses are expressed in terms of the potentials via the following relations (6):

$$P_{xz} = \mu\left(\frac{\partial u_x}{\partial z} + \frac{\partial u_z}{\partial x}\right) \tag{1-7}$$

$$P_{yz} = \mu\left(\frac{\partial u_z}{\partial y} + \frac{\partial u_y}{\partial z}\right) \tag{1-8}$$

$$P_{zz} = 2\mu\frac{\partial u_z}{\partial z} + \lambda\, \mathrm{div}\, \vec{u} \tag{1-9}$$

We express both the stresses and the displacements in terms of the potentials and subject them to the boundary conditions:

$$P_{xz}=0 \qquad P_{yz}=0 \qquad P_{zz}=0 \qquad \text{at } z = 0 \tag{1-10}$$

$$\left.\begin{array}{ll} u_x^{(1)} = u_x^{(2)} & P_{xz}^{(1)} - P_{xz}^{(2)} = P_{xz} \\ u_y^{(1)} = u_y^{(2)} & P_{yz}^{(1)} = P_{yz}^{(2)} \\ u_z^{(1)} = u_z^{(2)} & P_{zz}^{(1)} = P_{zz}^{(2)} \end{array}\right\} \quad \text{at } z = h \tag{1-11}$$

Thus we obtain nine equations in the nine coefficients A_1, A_2, $C_1^{(x)}$, $C_1^{(y)}$, $C_2^{(x)}$, $C_2^{(y)}$, $D_1^{(x)}$, $D_1^{(y)}$, B_1. After solving these in terms of s, q, ν and ν' we substitute the relevant coefficients into the expressions for the surface displacements which were obtained by substituting the set 1-3 into 1-4, 1-5 and 1-6:

$$(1\text{-}12)\qquad U_x = \frac{L}{2\pi} e^{i\omega t} \int_{-\infty}^{\infty}\int_{-\infty}^{\infty} \left(i\vartheta A_1 - \nu' D_1^{(y)}\right) e^{i(\vartheta x + \eta y)}\, d\vartheta\, d\eta$$

$$(1\text{-}13)\qquad U_y = \frac{L}{2\pi} e^{i\omega t} \int_{-\infty}^{\infty}\int_{-\infty}^{\infty} \left(i\eta A_1 + \nu' D_1^{(x)}\right) e^{i(\vartheta x + \eta y)}\, d\vartheta\, d\eta$$

$$(1\text{-}14)\qquad U_z = \frac{L}{2\pi} e^{i\omega t} \int_{-\infty}^{\infty}\int_{-\infty}^{\infty} \left(\nu B_1 + i\vartheta C_1^{(y)} - i\eta C_1^{(x)}\right) e^{i(\vartheta x + \eta y)}\, d\vartheta\, d\eta$$

We now change from the Fourier-transform to the Hankel-transform by the substitutions (7):

$$(1\text{-}15)\qquad \vartheta + i\eta = \kappa e^{i\alpha} \qquad\qquad x + iy = r e^{i\theta}$$

and then make use of some integral representations of the Bessel-functions (5).

$$(1\text{-}16)\qquad J_0(\kappa r) = \frac{1}{2\pi} \int_0^{2\pi} e^{i\kappa r \cos(\alpha - \theta)}\, d\alpha$$

$$(1\text{-}17)\qquad J_1(\kappa r) = \frac{1}{2\pi} \int_0^{2\pi} e^{i\kappa r \cos(\alpha - \theta) + i\left(\alpha - \theta - \frac{\pi}{2}\right)}\, d\alpha$$

to arrive at the expressions for the components of the displacement-vector in cylindrical coordinates, r, θ, z at z = 0:

$$(1\text{-}18)\qquad U_r = \frac{L\cos\theta}{2\pi\mu} e^{i\omega t} \int_0^{\infty} \frac{\kappa\nu'\left\{(2\kappa^2 - \kappa_\beta^2) e^{-\nu' h} - 2\kappa^2 e^{-\nu h}\right\}}{F(\kappa)} \left\{J_0(\kappa r) - \frac{1}{\kappa r} J_0(\kappa r)\right\} d\kappa$$

$$(1\text{-}19)\qquad u_\theta = \frac{L\sin\theta}{2\pi\mu r}\, e^{i\omega t}\int_0^\infty \frac{(2k^2-k_\beta^2)e^{-\nu' h} - 2k^2 e^{-\nu h}}{F(k)}\,\nu' J_1(kr)\,dk$$

$$(1\text{-}20)\qquad u_z = \frac{L\cos\theta}{2\pi\mu}\, e^{i\omega t}\int_0^\infty \frac{(2k^2-k_\beta^2)e^{-\nu h} - 2\nu\nu' e^{-\nu' h}}{F(k)}\,k^2 J_1(kr)\,dk$$

1.3 Evaluation of the Rayleigh displacements

We replace in equations 18-20 $2J_m(kr)$ by $H_m^{(1)}(kr) + H_m^{(2)}(kr)$ and integrate in the complex K plane as shown in figure 2. It is well known (8) that the residue at the Rayleigh-pole at $+\gamma k_\beta$, $\left(\gamma = \frac{1}{2}\sqrt{3+\sqrt{3}}\right)$ yields the surface-wave displacements and is given, e.g. for equation 1-20 in the form

$$(1\text{-}21)\qquad u_z = \frac{L\cos\theta}{2\pi\mu}\, e^{i\omega t}\,\frac{(2k_n^2-k_\beta^2)e^{-h\sqrt{k_n^2-k_\alpha^2}} - 2\sqrt{(k_n^2-k_\alpha^2)(k_n^2-k_\beta^2)}\,e^{-h\sqrt{k_n^2-k_\beta^2}}}{\frac{\partial F(k_n)}{\partial k_n}}\,\pi i\, k_n^2 H_1^{(2)}(k_n r)$$

where $k_n = \gamma k_\beta$ and πi arises from taking the principal value at the pole. The final results for all the components of the displacement are:

$$(1\text{-}22)\qquad u_r = \frac{iLC_3\cos\theta}{\mu}\,k_\beta\, e^{i\omega t}\left\{e^{-hk_n\alpha_1} - E_1 e^{-hk_n\alpha_2}\right\}\left\{H_0^{(2)}(k_n r) - \frac{1}{k_n r}H_1^{(2)}(k_n r)\right\}$$

$$(1\text{-}23)\qquad u_\theta = \frac{iLC_2\sin\theta}{\mu r}\, e^{i\omega t}\left\{e^{-hk_n\alpha_1} - E_1 e^{-hk_n\alpha_2}\right\}H_1^{(2)}(k_n r)$$

$$(1\text{-}24)\qquad u_z = \frac{-iLC_3\cos\theta}{\mu}\,k_\beta\, e^{i\omega t}\left\{e^{-hk_n\alpha_1} - E_2 e^{-hk_n\alpha_2}\right\}H_1^{(2)}(k_n r)$$

where C_1, C_2, C_3 are positive real constants, $\alpha_1 = \frac{\sqrt{\gamma^2-1}}{\gamma}$

$d_2=\frac{\sqrt{\gamma^2-\frac{1}{3}}}{\gamma}$ C_s - the shear velocity and C_R-the Rayleigh-wave velocity. Neglecting terms in $\frac{1}{r^{3/2}}$ and using the known approximation (9) $|\zeta| \gg |m|$

$$(1\text{-}25)\qquad H_m^{(2)}(\zeta) = \sqrt{\frac{2}{\pi\zeta}}\, e^{-i(\zeta - \frac{m\pi}{2} - \frac{\pi}{4})}\left\{1 + O(|\zeta|^{-1})\right\}$$

we get

$$(1\text{-}26)\qquad u_r = \frac{c_1' L}{\mu}\,\frac{\cos\theta}{\sqrt{r}}\,\sqrt{\kappa_\beta}\left\{e^{-h\kappa_n d_1} - E_1 e^{-h\kappa_n d_2}\right\} e^{i(\omega t - \kappa_n r + \frac{3\pi}{4})}$$

$$(1\text{-}27)\qquad u_\theta = \frac{c_2' L}{\mu}\,\frac{\sin\theta}{r^{3/2}}\,\frac{1}{\sqrt{\kappa_\beta}}\left\{e^{-h\kappa_n d_1} - E_1 e^{-h\kappa_n d_2}\right\} e^{i(\omega t - \kappa_n r - \frac{3\pi}{4})}$$

$$(1\text{-}28)\qquad u_z = \frac{c_3' L}{\mu}\,\frac{\cos\theta}{\sqrt{r}}\,\sqrt{\kappa_\beta}\left\{e^{-h\kappa_n d_1} - E_2 e^{-h\kappa_n d_2}\right\} e^{i(\omega t - \kappa_n r + \frac{\pi}{4})}$$

with $E_1=\frac{2\gamma^2}{2\gamma^2-1}$; $E_2=\frac{2\gamma^2-1}{2\sqrt{(\gamma^2-1)(\gamma^2-\frac{1}{3})}}$ and C_1', C_2', C_3'-positive real constants.

1.4 A model for a vertical strike-slip fault

Consider now our previous point-source, situated at depth h below the free surface, whose Rayleigh displacements are given by equations 1-22 - 1-24. Suppose that we have similiar sources distributed continuously from z = h_1 to z = h_2 (see fig. 3) thus filling the interval h on the z axis. Let these sources act simultaneously. The integrated effect at a point P (situated on the free surface), for u_z say, is from equation 1-24

$$(1\text{-}29)\qquad u_z = \frac{iLc_3}{\mu}\,\kappa_\beta \cos\theta\, e^{i\omega t} H_1^{(2)}(\kappa_n r)\,\frac{1}{\Delta h}\int_{h_1}^{h_2}\left(e^{-h\kappa_n d_1} - E_2 e^{-h\kappa_n d_2}\right) dh$$

(since there is no phase effect due to the differences in depth)

$$(1\text{-}30)\qquad U_z = \frac{iLC_3}{\gamma d_1 \mu}\cos\theta\, e^{i\omega t} H_1^{(2)}(k_n r)\,\frac{\left(e^{-h_1 k_n d_1} - e^{-h_2 k_n d_1}\right) - \gamma_2\left(e^{-h_1 k_n d_2} - e^{-h_2 k_n d_2}\right)}{\Delta h}$$

The reason for introducing the factor $\frac{1}{\Delta h}$ in front of equation 1-29 is to enable us to fall back on the expression for the point-source as $h_2 \longrightarrow h_1$.

Assume further that this segment of sources Δh, starts at some time $t_o = 0$ to move to the right (fig. 3), in the plane xz, with a finite speed V, up to the coordinate $x = b$, radiating as it moves. Taking into consideration the variation both in r and t, we get for the u_z component:

$$(1\text{-}31)\qquad U_z^R = \frac{2iC_3}{d_1 N_3}\, q_z(\omega)\,\frac{1}{b}\int_0^b \cos\theta\, H_1^{(2)}(k_n r)\, e^{i\omega\left(t-\frac{\xi}{V}\right)}\, d\xi$$

with

$$r^2 = y^2 + (x-\xi)^2 \quad ; \quad \cos\theta = \frac{x-\xi}{r}$$

$$(1\text{-}31')\qquad q_z(\omega) = \frac{N_3 L}{2\gamma\mu(\Delta h)}\left\{\left(e^{-h_1 k_n d_1} - e^{-h_2 k_n d_1}\right) - \gamma_2\left(e^{-h_1 k_n d_2} - e^{-h_2 k_n d_2}\right)\right\}$$

In order to evaluate equation 1-31 we make use of the "multiplication formulae" of the Bessel-functions (9), namely:

$$(1\text{-}32)\qquad B_m(\vartheta R) = \vartheta^m \sum_{M=0}^{\infty} \frac{B_{m+M}(R)}{M!}\left\{\frac{(1-\vartheta^2)}{2} R\right\}^M \qquad 1 > |1-\vartheta^2|$$

The geometry in figure 3 and figure 4 yields $R = K_n r_o$

$r = r_o\left(1 - 2\frac{\xi}{r_o}\cos\theta_o + \frac{\xi^2}{r_o^2}\right)^{\frac{1}{2}}$. We choose $\vartheta^2 = 1 - \frac{2}{r_o}\cos\theta_o + \frac{\xi^2}{r_o^2}$ so that

$|1-\vartheta^2| = \left|\frac{\xi}{r_o}\left(2\cos\theta_o - \frac{\xi}{r_o}\right)\right| < 1$ for $\frac{\xi}{r_o} < 1$. Substituting this into equation 1-32 and 1-32 into 1-31 and neglecting terms of the order $\left(\frac{\xi}{r_o}\right)^2$, we obtain for the integral (which we denote J for brevity),

$$(1\text{-}33) \qquad J = \frac{1}{b}\int_0^b \vartheta\cos\theta\, e^{i\omega\left(t-\frac{\xi}{V}\right)}\left\{\sum_{M=0}^{\infty}\frac{(K_n\xi\cos\theta)^M}{M!}H^{(2)}_{1+M}(K_n r_o)\right\}d\xi$$

Hence,

$$(1\text{-}34) \qquad J = \frac{\cos\theta_o}{\sqrt{r_o}}\sqrt{\frac{2}{\pi K_n}}\left\{\frac{e^{iK_n b(\cos\theta_o - c_R/V)} - 1}{K_n b(\cos\theta_o - c_R/V)}\right\}e^{i(\omega t - K_n r_o + \frac{3\pi}{4})} + O\left[(K_n r_o)^{-3/2}\right]$$

where terms higher than $\frac{1}{\sqrt{r_o}}$ have been neglected in accord with equation 1-25. In addition it is assumed that the extension of the source is small as compared with the range r_o. These assumptions are summed up as:

$$(1\text{-}35) \qquad \frac{\omega r_o}{c_R} \gg 1 \qquad (1\text{-}36) \qquad \left(\frac{b}{r_o}\right) \ll 1$$

Simplifying equation 1-34 and repeating the former technique for the other components, we obtain the parallel expressions for U_r^R and U_θ^R; the results are:

$$(1\text{-}37) \qquad U_r^R = \frac{2\cos\theta_o}{\sqrt{K_\beta r_o}}\, g_r(\omega)\frac{\sin X_R}{X_R}\, e^{i(\varphi_R - \frac{\pi}{4})}$$

$$(1\text{-}38) \qquad U_\theta^R = \frac{\sin\theta_o}{(K_\beta r_o)^{3/2}}\, g_\theta(\omega)\frac{\sin X_R}{X_R}\, e^{i(\varphi_R + \frac{\pi}{4})}$$

$$(1\text{-}39)\qquad U_z^R = \frac{2\cos\theta_0}{\sqrt{K_\beta r_0}}\, g_z(\omega)\, \frac{\sin X_R}{X_R}\, e^{i(\varphi_R - \frac{3\pi}{4})} \qquad \omega \neq 0$$

where N_i are some real positive constants and

$$(1\text{-}40)\qquad X_R = \frac{\omega b}{2c_R}\left(\frac{c_R}{V} - \cos\theta_0\right) \qquad (1\text{-}41)\qquad \varphi_R = \omega\left(t - \frac{r_0}{c_R}\right) - X_R$$

$$(1\text{-}42)\qquad g_r(\omega) = \frac{N_1}{2N_2}\, g_\theta(\omega) = \frac{N_1 L}{2\pi\mu(\Delta h)}\left\{\left(e^{-h_1 k_n d_1} - e^{-h_2 k_n d_1}\right) - \gamma_1\left(e^{-h_1 k_n d_2} - e^{-h_2 k_n d_2}\right)\right\}$$

The ratio $\frac{c_R}{V}$ is not subjected to any theoretical limitations.

1.5 A model for a vertical dip-slip fault

We shall now calculate the Rayleigh displacements for the case of a vertical dip-slip fault-plane (fig. 5). We shall make use of the results given by Pekeris (8) for a vertical concentrated point-source. Transforming his results (which were originally given for a step time dependence of the source) back into the steady-state source, we find:

$$(1\text{-}43)\qquad u_r = \frac{-L}{2\pi\mu}\, e^{i\omega t} \int_0^\infty \frac{2\nu\nu' e^{-\nu h} - (2k^2 - k_\beta^2) e^{-\nu' h}}{F(k)}\, J_1(kr)\, k^2\, dk$$

$$(1\text{-}44)\qquad u_\theta = 0$$

$$(1\text{-}45)\qquad u_z = \frac{L}{2\pi\mu}\, e^{i\omega t} \int_0^\infty \frac{(2k^2 - k_\beta^2) e^{-\nu h} - 2k^2 e^{-\nu' h}}{F(k)}\, J_0(kr)\, \nu k\, dk$$

On using the method of section 1.3 we get for the Rayleigh displacements:

$$u_r = \frac{-iLC_3}{\mu} K_\beta e^{i\omega t} H_1^{(2)}(K_n r)\left\{ e^{-hK_n d_1} - E_2 e^{-hK_n d_2} \right\} \tag{1-46}$$

$$u_z = \frac{iLC_4}{\mu} K_\beta e^{i\omega t} H_0^{(2)}(K_n r)\left\{ e^{-hK_n d_1} - E_1 e^{-hK_n d_2} \right\} \tag{1-47}$$

The realization of the fault-plane in this case is done in the following way: a horizontal line of sources which extends from x = 0 to x = b starts to radiate at some time $t_o = 0$. This line segment then moves downward in the z direction from $z = h_1$ to $z = h_2$, with a velocity V, radiating as it moves. The computation of the displacement at some point $P(\Theta, r)$ on the free surface involves two integrations:

$$U_r^R = \frac{-iLC_3}{\mu b(\Delta h)} K_\beta \int_{h_1}^{h_2}\int_0^b \left(e^{-hK_n d_1} - E_2 e^{-hK_n d_2}\right) H_1^{(2)}(K_n r)\, e^{i\omega\left(t - \frac{h-h_1}{V}\right)}\, dh\, d\xi \tag{1-48}$$

$$U_z^R = \frac{iLC_4}{\mu b(\Delta h)} K_\beta \int_{h_1}^{h_2}\int_0^b \left(e^{-hK_n d_1} - E_1 e^{-hK_n d_2}\right) H_0^{(2)}(K_n r)\, e^{i\omega\left(t - \frac{h-h_1}{V}\right)}\, dh\, d\xi \tag{1-49}$$

with $$r = r_0\left(1 - 2\frac{\xi}{r_0}\cos\theta_0 + \frac{\xi^2}{r_0^2}\right)^{\frac{1}{2}}$$

Following our previous method (equations 1-32 to 1-35) we get, to first approximation:

$$i e^{i\omega t}\frac{1}{b}\int_0^b H_0^{(2)}(K_n r)\, d\xi = \sqrt{\frac{2}{\pi K_n r_0}}\frac{\sin Y_R}{Y_R} e^{i\left(\psi_R + \frac{3\pi}{4}\right)} \tag{1-50}$$

$$-i e^{i\omega t}\frac{1}{b}\int_0^b H_1^{(2)}(K_n r)\, d\xi = \sqrt{\frac{2}{\pi K_n r_0}}\frac{\sin Y_R}{Y_R} e^{i\left(\psi_R + \frac{\pi}{4}\right)} \tag{1-51}$$

with

$$(1\text{-}52)\qquad \gamma_R = \frac{\omega b \cos\theta_0}{2c_R} \qquad\qquad \psi_R = \omega\left(t - \frac{r_0}{c_R}\right) + \gamma_R \qquad\qquad \omega \neq 0$$

the second integration over h is exact. The final results are

$$(1\text{-}53)\qquad U_z^R = \frac{\angle c_4'}{\mu\sqrt{r_0}}\sqrt{K_\beta}\,\frac{\sin\gamma_R}{\gamma_R}\left\{\frac{\sin\Theta_1}{\Theta_1}e^{i\Theta_1 - h_1\kappa_n d_1} - E_1\frac{\sin\Theta_2}{\Theta_2}e^{i\Theta_2 - h_1\kappa_n d_2}\right\}e^{i\left(\psi_R + \frac{3\pi}{4}\right)}$$

$$(1\text{-}54)\qquad U_r^R = \frac{\angle c_3'}{\mu\sqrt{r_0}}\sqrt{K_\beta}\,\frac{\sin\gamma_R}{\gamma_R}\left\{\frac{\sin\Theta_1}{\Theta_1}e^{i\Theta_1 - h_1\kappa_n d_1} - E_2\frac{\sin\Theta_2}{\Theta_2}e^{i\Theta_2 - h_1\kappa_n d_2}\right\}e^{i\left(\psi_R + \frac{\pi}{4}\right)}$$

with

$$(1\text{-}55)\qquad \Theta_1 = \frac{(h_2 - h_1)\omega}{2c_R}\left\{i\frac{\sqrt{\gamma^2 - 1}}{\gamma} - \frac{c_R}{v}\right\}\ ,\quad \Theta_2 = \frac{(h_2 - h_1)\omega}{2c_R}\left\{i\frac{\sqrt{\gamma^2 - 1/3}}{\gamma} - \frac{c_R}{v}\right\}$$

Note that Θ_1 and Θ_2 are complex. For the sake of numerical computations it is useful to use the relations: $(\zeta = \bar{x} + i\bar{y})$

$$(1\text{-}56)\qquad \frac{\sin\zeta}{\zeta} = \frac{\sqrt{\sin^2\bar{x}\,ch^2\bar{y} + sh^2\bar{y}\cos^2\bar{x}}}{\sqrt{\bar{x}^2 + \bar{y}^2}}\,e^{i\,tg^{-1}\left\{\frac{\bar{y} + \bar{x}\,ctg\bar{x}\,th\bar{y}}{\bar{x} - \bar{y}\,ctg\bar{x}\,th\bar{y}}\right\}}$$

When dealing with high frequencies, the previous equations may be simplified due to the fact that $d_2 \simeq 2d_1$ and the term involving Θ_2 in equations 1-53 and 1-54 becomes insignificant. We also observe that in case that $\frac{c_R}{v} \gg \frac{\sqrt{\gamma^2 - 1}}{\gamma}$

i.e., $v \ll c_R$, may be taken as real. In the opposite case $v \gg c_R$, it may be considered pure imaginary. For either long periods, or $b \longrightarrow 0$ ~~or~~, $h_1 \longrightarrow h_2$ we fall back on the point-source solution.

1.6 Dip-slip fault with arbitrary dip angle

Consider a fault-plane striking in the direction of the y axis, and dipping at an angle δ with respect to the free surface (fig. 6). Let a simple force $\overrightarrow{L}$, pointing along the fault, be localized at each point of a segment y = 0 to y = c (which is parallel to the y axis at depth $z = h_1$). We may split the force $\overrightarrow{L}$ into a vertical component and a horizontal component,

(1-57) $$L_x = |L| \cos\delta$$

(1-58) $$L_z = |L| \sin\delta$$

We shall first compute the three components U_r^R, U_θ^R and U_z^R due to L_x. Making use of equations 1-22 - 1-24, we have:

(1-59) $$\left(U_r^R\right)_x = \frac{iLC_1}{\mu\bar{\sigma}c} K_\beta \int_0^{\bar{\sigma}}\int_0^c \left\{e^{-K_n d_1 (h_1 + \xi\sin\delta)} - E_1 e^{-K_n d_2 (h_1+\xi\sin\delta)}\right\} \cos\theta\, H_0^{(2)}(K_n r)\, e^{i\omega\left(t-\frac{\xi}{V}\right)} d\eta\, d\xi$$

(1-60) $$\left(U_\theta^R\right)_x = \frac{iLC_2}{\mu\bar{\sigma}c} \int_0^{\bar{\sigma}}\int_0^c \left\{e^{-K_n d_1 (h_1 + \xi\sin\delta)} - E_1 e^{-K_n d_2 (h_1+\xi\sin\delta)}\right\} \frac{\sin\theta}{r} H_1^{(2)}(K_n r)\, e^{i\omega\left(t-\frac{\xi}{V}\right)} d\eta\, d\xi$$

(1-61) $$\left(U_z^R\right)_x = \frac{-iLC_3}{\mu\bar{\sigma}c} K_\beta \int_0^{\bar{\sigma}}\int_0^c \left\{e^{-K_n d_1 (h_1 + \xi\sin\delta)} - E_2 e^{-K_n d_2 (h_1+\xi\sin\delta)}\right\} \cos\theta\, H_1^{(2)}(K_n r)\, e^{i\omega\left(t-\frac{\xi}{V}\right)} d\eta\, d\xi$$

with

(1-62) $$r^2 = (x - \xi\cos\delta)^2 + (y-\eta)^2$$

where c is the y-extension of the fault. Using the method of equations 1-32 to 1-35, we use

$$(1\text{-}63)\quad \begin{cases} r = r_0\vartheta & \vartheta^2 = 1 - \frac{2}{r_0}(\xi\cos\theta_0\cos\delta + \eta\sin\theta_0) + \\ & \quad + \frac{\eta^2 + \xi^2\cos^2\delta}{r_0^2} \\ \therefore \frac{1}{2}r_0(1-\vartheta^2) \simeq \xi\cos\theta_0\cos\delta + \eta\sin\theta_0 & \end{cases}$$

The integration yields

$$(1\text{-}64)\quad (U_r^R)_x = \frac{c_1' L}{\mu}\frac{\cos\theta_0}{\sqrt{r_0}}\sqrt{\kappa_\beta}\left\{\frac{\sin Q_1^R}{Q_1^R}e^{-iQ_1^R - \kappa_n h_1 d_1} - E_1\frac{\sin Q_2^R}{Q_2^R}e^{-iQ_2^R - \kappa_n h_1 d_2}\right\}\frac{\sin Z_R}{Z_R}e^{i(\tau_R + \frac{3\pi}{4})}$$

$$(1\text{-}65)\quad (U_\theta^R)_x = \frac{c_2' L}{\mu}\frac{\sin\theta_0}{r_0^{3/2}}\frac{1}{\sqrt{\kappa_\beta}}\left\{\frac{\sin Q_1^R}{Q_1^R}e^{-iQ_1^R - \kappa_n h_1 d_1} - E_1\frac{\sin Q_2^R}{Q_2^R}e^{-iQ_2^R - \kappa_n h_1 d_2}\right\}\frac{\sin Z_R}{Z_R}e^{i(\tau_R - \frac{3\pi}{4})}$$

$$(1\text{-}66)\quad (U_z^R)_x = \frac{c_3' L}{\mu}\frac{\cos\theta_0}{\sqrt{r_0}}\sqrt{\kappa_\beta}\left\{\frac{\sin Q_1^R}{Q_1^R}e^{-iQ_1^R - \kappa_n h_1 d_1} - E_2\frac{\sin Q_2^R}{Q_2^R}e^{-iQ_2^R - \kappa_n h_1 d_2}\right\}\frac{\sin Z_R}{Z_R}e^{i(\tau_R + \frac{\pi}{4})}$$

$$(1\text{-}67)\quad \begin{cases} Q_1^R = \frac{\omega\bar{\sigma}}{2c_R}\left[\left(\frac{c_R}{V} - \cos\delta\cos\theta_0\right) + i\sin\delta\frac{\sqrt{\gamma^2 - 1}}{\gamma}\right] \\ Q_2^R = \frac{\omega\bar{\sigma}}{2c_R}\left[\left(\frac{c_R}{V} - \cos\delta\cos\theta_0\right) + i\sin\delta\frac{\sqrt{\gamma^2 - 1/3}}{\gamma}\right] \end{cases}$$

$$(1\text{-}68)\quad Z_R = \frac{\omega c\sin\theta_0}{2c_R} \quad ; \quad \tau_R = \omega\left(t - \frac{r_0}{c_R}\right) - Z_R$$

In a similar manner we may obtain the suitable expressions for the contribution due to L_Z. Combining them all, we have for the total Rayleigh-radiation of the dip-slip fault-plane:

$$(1\text{-}69)\quad \begin{cases} (U_r^R)_{total} = (U_r^R)_x\cos\delta + (U_r^R)_z\sin\delta \; ; \; (U_z^R)_{total} = (U_z^R)_x\cos\delta + (U_z^R)_z\sin\delta \\ (U_\theta^R)_{total} = (U_\theta^R)_x \end{cases}$$

1.7 Strike-slip fault with arbitrary dip angle

The situation is displayed in figure 7.

Applying the former method we get, with

$$(1\text{-}70)\quad \begin{cases} r = r_0\vartheta \qquad r^2 = (x-\xi)^2 + (y-\eta\cos\delta)^2 \\ \vartheta^2 = 1 - \frac{2}{r_0}\left(\eta\sin\theta_0\cos\delta + \xi\cos\theta_0\right) + \frac{\xi^2 + \eta^2\cos^2\delta}{r_0^2} \end{cases}$$

the approximation:

$$(1\text{-}71)\qquad \tfrac{1}{2}r_0(1-\vartheta^2) \cong \xi\cos\theta_0 + \eta\sin\theta_0\cos\delta$$

Using equations 1-32 and 1-22 - 1-24 and realizing the fault as described in figure 7, we obtain,

$$(1\text{-}72)\quad U_r^R = \frac{iC_1L}{\mu\sigma b} K_\beta \int_0^\sigma\int_0^b \cos\theta\left\{e^{-K_n d_1(h_1+\eta\sin\delta)} - E_1 e^{-K_n d_2(h_1+\eta\sin\delta)}\right\} H_0^{(2)}(K_n r)\, e^{i\omega\left(t-\frac{\xi}{v}\right)}\, d\eta\, d\xi$$

Evaluating this double integral along the lines stated above, we get, to terms of the order of $\frac{1}{\sqrt{r_0}}$:

$$(1\text{-}73)\quad U_r^R = \frac{LC_1'}{\mu}\frac{\cos\theta_0}{\sqrt{r_0}}\sqrt{K_\beta}\,\frac{\sin X_R}{X_R}\left\{\frac{\sin\Delta_1^R}{\Delta_1^R}e^{-i\Delta_1^R - h_1K_nd_1} - E_1\frac{\sin\Delta_2^R}{\Delta_2^R}e^{-i\Delta_2^R - h_1K_nd_2}\right\}e^{i\left(\varphi_R + \frac{3\pi}{4}\right)}$$

and similarly

$$(1\text{-}74)\quad U_\theta^R = \frac{LC_2'}{\mu}\frac{\sin\theta_0}{r_0^{3/2}}\frac{1}{\sqrt{K_\beta}}\frac{\sin X_R}{X_R}\left\{\frac{\sin\Delta_1^R}{\Delta_1^R}e^{-i\Delta_1^R - h_1K_nd_1} - E_1\frac{\sin\Delta_2^R}{\Delta_2^R}e^{-i\Delta_2^R - h_1K_nd_2}\right\}e^{i\left(\varphi_R - \frac{3\pi}{4}\right)}$$

$$(1\text{-}75)\quad U_z^R = \frac{LC_3'}{\mu}\frac{\cos\theta_0}{\sqrt{r_0}}\sqrt{K_\beta}\,\frac{\sin X_R}{X_R}\left\{\frac{\sin\Delta_1^R}{\Delta_1^R}e^{-i\Delta_1^R - h_1K_nd_1} - E_2\frac{\sin\Delta_2^R}{\Delta_2^R}e^{-i\Delta_2^R - h_1K_nd_2}\right\}e^{i\left(\varphi_R + \frac{\pi}{4}\right)}$$

with

$$(1\text{-}76)\quad \begin{cases} \Delta_1^R = \frac{\omega\sigma}{2C_R}\left(\cos\delta\sin\theta_0 + i\sin\delta\frac{\sqrt{\gamma^2-1}}{\gamma}\right) \\ \Delta_2^R = \frac{\omega\sigma}{2C_R}\left(\cos\delta\sin\theta_0 + i\sin\delta\frac{\sqrt{\gamma^2-1/3}}{\gamma}\right) \end{cases} \qquad \omega \neq 0$$

Here again Λ_1^R and Λ_2^R are complex. This is so because the depth does not have a phase effect while the extension along the y-axis, does. The former results are easily generalized for a radiating dipole: we differentiate each of equations 1-37 to 1-39 with respect to y with $\frac{\partial}{\partial y} = \sin\theta_o \frac{\partial}{\partial r_o} + \frac{\cos\theta_o}{r_o}\frac{\partial}{\partial\theta_o}$. Neglecting terms higher than $\frac{1}{\sqrt{r_o}}$ we find that the only terms which contribute to this order of magnitude are those which arise from differentiating the exponent $e^{i\varphi_R}$. It means that in order to obtain the dipole solutions we have to multiply equations 1-37 to 1-39 by the factor $K_n \sin\theta_o e^{-\frac{\pi i}{2}}$. This is given in equations 1-37^a to 1-39^a. In case that $\delta = \frac{\pi}{2}$ we get back equations 1-37 to 1-39.

$$(1\text{-}37^a)\quad (U_r^R)_{dipole} = \frac{\sin 2\theta_o}{\sqrt{r_o}}\, g_r(\omega)\sqrt{K\beta}\, \frac{\sin X_R}{X_R}\, e^{i(\varphi_R - \frac{3\pi}{4})} + O\left[(K_n r_o)^{-3/2}\right]$$

$$(1\text{-}38^a)\quad (U_\theta^R)_{dipole} = \frac{\sin^2\theta_o}{r_o^{3/2}}\, g_\theta(\omega)\, \frac{1}{\sqrt{K\beta}}\, \frac{\sin X_R}{X_R}\, e^{i(\varphi_R - \frac{\pi}{4})} + O\left[(K_n r_o)^{-5/2}\right]$$

$$(1\text{-}39^a)\quad (U_z^R)_{dipole} = \frac{\sin 2\theta}{\sqrt{r_o}}\, g_z(\omega)\sqrt{K\beta}\, \frac{\sin X_R}{X_R}\, e^{i(\varphi_R + \frac{3\pi}{4})} + O\left[(K_n r_o)^{-3/2}\right]$$

If one wishes, one may obtain also solutions for bidirectional fault by superposing on equations 1-37^a to 1-39^a the solution $-U_i(\pi - \theta)$. (Motion starts simultaneously from the source in two opposite directions.) The same applies to equations 1-53 - 1-54 and 1-73 to 1-75.

1.8 A worked example

Let us now investigate in detail the case of the strike-slip fault-plane, for a concrete example, in order to see the behaviour of the various parameters which take part in the mathematical formulation of the resulting displacements. The limitations on the choice of the parameters is given by equations 1-35 and 1-36. The condition $\frac{\omega r_o}{c_R} \gg 1$ has obviously the physical meaning:

$$r_o \gg \frac{\lambda}{2\pi} \tag{1-77}$$

Looking back on the previous equations we note that the ratio $\frac{b}{\lambda}$ appears in the parameters, X and Y and has a dominating influence on the function $\frac{\sin X}{X}$. Let us investigate the radial Rayleigh-displacement for the case $\delta = \frac{\pi}{2}$ with a dipole-type moving source. Multiplying equation 1-37 by $\frac{\omega}{c_R} \sin\theta_o e^{-\frac{\pi i}{2}}$ we have:

$$|U_r^R| = \left| \frac{\mu c_s'}{\mu(\Delta h)} \frac{\sin 2\theta_o}{\sqrt{r_o T}} \frac{\sin X_R}{X_R} \left\{ \left(e^{-\frac{a_1}{T}} - e^{-\frac{a_3}{T}}\right) - \gamma_1 \left(e^{-\frac{a_3}{T}} - e^{-\frac{a_4}{T}}\right) \right\} \right| \tag{1-78}$$

with

$$a_1 = \frac{2\pi h_1 d_1}{c_R} \qquad a_2 = \frac{2\pi h_2 d_1}{c_R} \qquad a_3 = \frac{2\pi h_1 d_2}{c_R} \qquad a_4 = \frac{2\pi h_2 d_2}{c_R} \tag{1-79}$$

From now on we omit the phase factor, taking only the absolute value of the displacements.

The amplitude factor of $|U_r^R|$ is built of three sub-factors. The factor sin $2\theta_o$ is characteristic for the dipole-field of a point-source. The factor containing the four exponentials plays the role of an attenuator and has a single zero for some T which depends on the constants a_i and γ_1. (U_z^R has also such a zero.) The third factor which is of the type $\frac{\sin X}{X}$ is a contribution of the finiteness of the source in the direction of the propagating disturbance. It is this factor which is responsible for the deviation from the pure dipole-field. This function has its zeros at

$$\frac{\omega b}{2c_R}\left(\frac{c_R}{V} - \cos\theta_o\right) = n\pi \qquad n = 1,2,\cdots$$

We rewrite this relation in the form

$$\frac{b}{V}c_R - b\cos\theta_o = n\lambda \tag{1-80}$$

from which the physical significance is clear: it is the condition for <u>destructive interference</u> at the point of observation. This case is analogous in many ways to the Frauenhoffer-diffraction through a rectangular slit and should not be mistaken for the condition of constructive interference in the case of two separated point-sources. The important thing to remember is that as long as

$$n\pi < \left|\frac{\omega b}{2c_R}\left(\frac{c_R}{V} - \cos\theta_o\right)\right| < (n+1)\pi$$

, no additional zeros are introduced into the normal dipole-pattern, and no more than a relative reduction in amplitude is expected. Thus, a bound for b can be set if the observed pattern for a certain frequency does not deviate from the point-dipole scheme.

Furthermore, the excessive number of zeros in any quadrant will be equal to the greatest integer in $[2\frac{b}{\lambda}]$ with an uncertainty of unity. The number of loops is therefore a clear measure for the dimensions of the source. Another interesting outcome of the dependence on $\frac{\sin X}{X}$ is exhibited by the ratio of amplitudes at equal distances in two opposite directions:

$$(1\text{-}81) \qquad \left|\frac{U_r^R(\theta_0)}{U_r^R(\pi+\theta_0)}\right| = \left|\frac{\dfrac{\sin\frac{\pi b}{\lambda}\left(\frac{c_R}{V}-\cos\theta_0\right)}{\frac{\pi b}{\lambda}\left(\frac{c_R}{V}-\cos\theta_0\right)}}{\dfrac{\sin\frac{\pi b}{\lambda}\left(\frac{c_R}{V}+\cos\theta_0\right)}{\frac{\pi b}{\lambda}\left(\frac{c_R}{V}+\cos\theta_0\right)}}\right|$$

It is important to note that this ratio, at least for the strike-slip fault, is independent of the source time-function as well as of the layering of the elastic half-space. We shall later make use of this fact. It is obvious from equation 1-81 that this ratio may acquire any value between unity to infinity. The phenomenon that surface-waves amplitudes show a very strong dependence on the azimuth of the station has already been established by H. Benioff and B. Gutenberg (10,11). This ratio approaches unity as $(\frac{b}{\lambda})$ decreases, and is another measure for the source extension, and the speed of rupture.

In our computation, the following magnitudes have been used:

$$b = 60 \text{ km}$$

$$h_1 = 15 \text{ km}$$

$$h_2 = 20 \text{ km} \quad (\Delta h = 5 \text{ km})$$

$$\pi b / C_R = 50$$

so that

$$a_1 = 9 \text{ sec}$$

$$a_2 = 12 \text{ sec}$$

$$a_3 = 18 \text{ sec}$$

$$a_4 = 24 \text{ sec}$$

with these numbers, we see that the function $\left(e^{-\frac{9}{T}} - e^{-\frac{12}{T}}\right) - 0{,}80\left(e^{-\frac{18}{T}} - e^{-\frac{24}{T}}\right)$ has a zero for $T \cong 20$ sec. It is positive for $T < 20$ sec and negative for $T > 20$ sec. Results are given in figures 9-20. The first set (fig. 9-14) gives the dependence of U_r on θ_o. θ_o is given at intervals of 5° and the parameter $\frac{C_R}{V}$ runs over the set: $\frac{C_R}{V} = 4$; $(V \sim 1 \frac{km}{sec})$, 0.9194, $(V \simeq \beta)$; 0.5308, $(V \simeq \alpha)$. Periods have been chosen as T = 15 sec, 25 sec, 50 sec. For periods higher than 50 the deviation from the dipole-field is small. The second set of figures (11-19) gives $|U_r^R|$ as a function of T where θ_o is the parameter, and in the third group (fig. 18-20) the amplitude is given as a function of the ratio $\frac{C_R}{V}$ with θ as a parameter.

To see what happens for dip angles other than $\delta = \frac{\pi}{2}$ we shall take the other extremity, $\delta = 0$. The amplitude factor of $|U_r^R|$ for this case is, from equation 1-73:

$$(1\text{-}82)\quad |U_r^R| = \frac{c_6' L}{\mu}\frac{\sin 2\theta}{\sqrt{r_0}}\frac{1}{T^{3/2}}\frac{\sin X_R}{X_R}\frac{\sin\left(\frac{\pi\sigma}{\lambda}\sin\theta_0\right)}{\left(\frac{\pi\sigma}{\lambda}\sin\theta_0\right)}\left\{e^{-\frac{a_1}{\pi}} - E_1 e^{-\frac{a_3}{\pi}}\right\}$$

where a_1, a_3 are the same as in equation 1-79, and $E_1 = \frac{2\gamma^2}{2\gamma^2-1}$. Examining equation 1-82 we notice that for the previous values of $\sigma = 5$ km and $T \geqslant 15$ sec, we always have $\frac{\sigma}{\lambda}\sin\theta_0 \leq \frac{1}{3}\sin\theta_0 < 1$ i.e., the deviation from the results for $\delta = \frac{\pi}{2}$ will be small unless σ acquires higher values. We conclude therefore, that the dip angle for the strike-slip case with $\sigma \ll b$ has no fundamental influence on the wave pattern. The computation for U_z^R may be carried along the same lines given hitherto, and there is essentially no remarkable qualitative difference of the wave-pattern for this case.

1.9 Generalization to a layered half-space

The former results may be generalized to an inhomogeneous elastic medium which in turn may be represented by a multi-layered half-space. Consider a horizontal simple-force placed in the j^{th} layer of an m-layered half-space, at depth h below the free surface. We shall follow the method of analysis given in section 1.2: After defining $3m+6$ scalar potential-functions there will be $6m+9$ "boundary-conditions" equations for the $6m+9$ indeterminate coefficients. The surface Rayleigh-displacements will have the form:

$$(1\text{-}83)\quad u_r = \frac{iL}{2\mu_1}\cos\theta\, e^{i\omega t}\sum_{n=0}\frac{K_n\, {}_mF_1^{j}(K_n)}{\frac{\partial\, {}_mF_0(K_n)}{\partial K_n}}\left\{H_0^{(2)}(K_n r)-\frac{1}{K_n r}H_1^{(2)}(K_n r)\right\}$$

$$(1\text{-}84)\quad u_\theta = \frac{iL}{2\mu_1 r}\sin\theta\, e^{i\omega t}\sum_{n=0}\frac{{}_mF_1^{j}(K_n)}{\frac{\partial\, {}_mF_0(K_n)}{\partial K_n}}H_1^{(2)}(K_n r)$$

$$(1\text{-}85)\quad u_z = \frac{iL}{2\mu_1}\cos\theta\, e^{i\omega t}\sum_{n=0}\frac{K_n\, {}_mF_2^{j}(K_n)}{\frac{\partial\, {}_mF_0(K_n)}{\partial K_n}}H_1^{(2)}(K_n r)\qquad m = 0,1,2,\cdots$$

Here ${}_mF_0(K_n)$ stands for the Rayleigh-determinant for the layered half-space and ${}_mF_1^{j}(K_n)$, ${}_mF_2^{j}(K_n)$ are some linear combinations of the cofactors of the ~~Rayleigh~~ system-determinant. These expressions are simple functions of the source depth, the width of the layers and the elastic parameters of these layers. The summation extends over all the possible modes.

The integrated Rayleigh-pattern for a vertical strike-slip fault with a dipole-type source is given in equations 3-3 and 3-4. To obtain the exact analytical forms of $g_r^m(\omega)$ and $g_z^m(\omega)$ (defined there) in case that the fault extends downward through m_o layers, one has to evaluate ${}_mF_1^{j}(K_n)$ and ${}_mF_2^{j}(K_n)$ for m_o different cases. Each case corresponding to the source being located at a different layer. The resulting $2m_o$ functions ${}_mF_1^{j}(h,\omega)$, ${}_mF_2^{j}(h,\omega)$ $\quad j = 1,2,\cdots\ m_o \leq m$ are

then integrated individually with respect to h between the proper limits. Finally we have: $(m = 1)$

$$(1\text{-}86) \qquad g_r^m = w_1 \frac{\sum_{j=1}^{m_0} \int_{H_{j-1}}^{H_j} {}_mF_1^j(\omega, h)\, dh}{\frac{\partial_m F_0(K_n)}{\partial K_n}}$$

$$(1\text{-}87) \qquad g_z^m = w_2 \frac{\sum_{j=1}^{m_0} \int_{H_{j-1}}^{H_j} {}_mF_2^j(\omega, h)\, dh}{\frac{\partial_m F_0(K_n)}{\partial K_n}}$$

$$m = 0, 1, 2, \cdots$$

H_j is the width of the j^{th} layer. $H_0 = 0$. w_1 and w_2 are some positive real constants. It has been assumed here that the fault extends from the free surface. Expressions for ${}_1F_1^1(K_n)$, ${}_1F_2^1(K_n)$ and ${}_1F_0(K_n)$ are given by Kanovskaya (4). It can be shown that the surface displacements are specified already by $6m + 3$ indeterminate coefficients. That is so because the corresponding differences between the 6 coefficients above the source and the 6 coefficients below the source lead to terms of zero residue in the integral representation of the surface displacements. It has also been proved by Keylis-Borok (references given in (4)) that $\sum_m$, the $(6m + 3)$ by $(6m + 3)$ determinant of the total system, is factorable into a Rayleigh-determinant ${}_mF_0$ of order $3m + 3$ and a Love-determinant Δ_L of order $3m$:

$$(1\text{-}88) \qquad \sum_m = \left\{ -K^{2m+1} (K\beta)_{\substack{half \\ space}} \prod_{j=1}^{m} K_{\beta m}^2 \right\} {}_mF_0 \cdot \Delta_L$$

where $K_{\beta m}$ is the shear wave-number of the mth layer.

CHAPTER II

LOVE-WAVES FROM FINITE MOVING SOURCES

2.1 Introduction

The effect of the finiteness of the seismic focus on the Love-wave radiation pattern is investigated. We start from the exact solution for the surface displacements due to a harmonic horizontal point-source, situated in a homogeneous layer overlaying a homogeneous half-space. A fault plane is then realized by moving this source along a line with finite speed and integrating the Love-poles contribution across a finite rectangle in the layer. Displacements are evaluated for long ranges and expressions are obtained for strike-slip and dip-slip fault types. Attention is mainly focused on a dipole-type motion of a vertical strike-slip model. The theory is then applied to the G-wave pattern for which the results are also transformed into the time domain. It is also demonstrated how this theory may lead to an estimate of source parameters such as fault-length and rupture-velocity from phases and amplitudes ratio of G or R waves recorded at a single station.

All present computations and results will be limited to the first mode only, as higher modes are not observed under common circumstances. Consequently, $C_L(\omega)$ will stand for the first branch of the dispersion curve. It will soon become clear that the SH fault-plane displacements will

differ from the corresponding Rayleigh-displacements, mainly due to the fact that Love-wave amplitudes in the layer do not depend strongly upon depth (6).

2.2 The horizontal-source solution

The surface displacements for a simple horizontal force, acting at depth h below the free surface in a layer of depth H was given by Yanovskaya (4). Using the method outlined in Chapter I for a horizontal force in the sense of section 1.2, located at z = h < H (fig. 21), we have:

$$(2\text{-}1) \qquad u_r = \frac{-iL}{2\mu_1} \frac{\cos\theta}{r} e^{i\omega t} H_1^{(2)}(\kappa_n r) \frac{D_L(\kappa_n; H; h)}{\frac{\partial \Delta_L(\kappa_n; H)}{\partial \kappa_n}}$$

$$(2\text{-}2) \qquad u_\theta = \frac{-iL}{2\mu_1} \sin\theta\, e^{i\omega t} \frac{\kappa_n D_L(\kappa_n; H; h)}{\frac{\partial \Delta_L(\kappa_n; H)}{\partial \kappa_n}} \left\{ H_0^{(2)}(\kappa_n r) - \frac{1}{\kappa_n r} H_1^{(2)}(\kappa_n r) \right\}$$

$$(2\text{-}3) \qquad u_z = 0 \quad , \quad n = 1$$

The suitable expressions for the cartesian components are accordingly

$$(2\text{-}4)\qquad u_x = \frac{iL}{2\mu_1}\sin^2\theta\, e^{i\omega t} H_0^{(2)}(nKr)\,\frac{nK\,D_L(nK,H,h)}{\dfrac{\partial \Delta_L(nK,H)}{\partial nK}} + O\left[(nKr)^{-3/2}\right]$$

$$(2\text{-}5)\qquad u_y = \frac{-iL}{4\mu_1}\sin 2\theta\, e^{i\omega t} H_0^{(2)}(nKr)\,\frac{nK\,D_L(nK,H,h)}{\dfrac{\partial \Delta_L(nK,H)}{\partial nK}} + O\left[(nKr)^{-3/2}\right]$$

$$(2\text{-}6)\qquad u_z = 0 \quad , \quad n=1$$

The notation incorporated in equations 2-1 to 2-6, is

$$(2\text{-}7)\qquad D_L = \left[\zeta\frac{\nu_2}{\nu_1}\,sh(\nu_1 H) + ch(\nu_1 H)\right] ch(\nu_1 h)$$

$$(2\text{-}8)\qquad \Delta_L = \zeta\nu_2\, ch(\nu_1 H) + \nu_1\, sh(\nu_1 H)$$

$$(2\text{-}9)\qquad \begin{cases} \zeta = \dfrac{\mu_2}{\mu_1} \\ h = H - q \\ K_1 = \dfrac{\omega}{\beta_1} \\ K_2 = \dfrac{\omega}{\beta_2} \\ nK = \dfrac{\omega}{C_L} \end{cases} \qquad \begin{aligned} \nu_1 &= \left(nK^2 - K_1^2\right)^{\frac{1}{2}} = i\omega\alpha_1 \\ \nu_2 &= \left(nK^2 - K_2^2\right)^{\frac{1}{2}} = \omega\alpha_2 \\ \alpha_1 &= \left(\beta_1^{-2} - C_L^{-2}\right)^{\frac{1}{2}} \\ \alpha_2 &= \left(C_L^{-2} - \beta_2^{-2}\right)^{\frac{1}{2}} \\ \beta_2 &\geq C_L \geq \beta_1 \end{aligned}$$

and $C_L = C_L(\omega)$ is given implicitly by the "period-equation"

(2-10) $$\Delta_L = 0$$

Performing the operations indicated in equations 2-1 - 2-2 we get, with the aid of equations 2-7 to 2-10, for the leading term of u_θ: (we shall give henceforth the results for u_θ only, as u_r varies like $r_o^{-3/2}$):

(2-11) $$u_\theta = \frac{-iL}{2\mu_1} \sin\theta \, H_o^{(2)}(\eta kr) e^{i\omega t} N_o(\omega) \cos(h\omega\alpha_1) + O[(\eta kr)^{-3/2}]$$

with

(2-12) $$N_o(\omega) = \frac{\alpha_2 \omega}{\alpha_2 \omega H + \zeta \left\{ \frac{1 + (\alpha_2/\alpha_1)^2}{1 + \zeta^2 (\alpha_2/\alpha_1)^2} \right\}}$$

2.3 A model for a dip-slip fault in the layer

Imagine a fault-plane striking in the direction of the axis and dipping at an angle δ with respect to the free surface (fig. 22). Assume further that the impulse starts at some depth h_1, in the layer, along a line $y = 0$ to $y = c$, directed downwards, at the angle δ. We may split the force $\vec{L}$ into a vertical component and a horizontal com-

ponent, thus: $L_x = |L| \cos\delta$ $L_z = |L| \sin\delta$. The only contribution to Love-waves arises from the L_x component. Using the same method as given in section 1.6 we get for the integrated radiation:

$$(2\text{-}13)\quad U_\theta^L = \frac{L}{2\mu_1\sqrt{2\pi}} \frac{\sin\theta_0 \cos\delta}{\sqrt{\kappa r_0}} N_0(\omega) \frac{\sin Z_L}{Z_L} \left\{ \frac{\sin Q_1^L}{Q_1^L} e^{i(\omega h_1 \alpha_1 + Q_1^L)} + \frac{\sin Q_2^L}{Q_2^L} e^{-i(\omega h_1 \alpha_1 - Q_2^L)} \right\} e^{i(\tau_L + \frac{3\pi}{4})}$$

with

$$(2\text{-}14)\quad Z_L = \frac{\omega c \sin\theta_0}{2c_L} \qquad \tau_L = \omega\left(t - \frac{r_0}{c_L}\right) - Z_L$$

$$(2\text{-}15)\quad Q_1^L = \frac{\omega\bar{\sigma}}{2c_L}\left\{\left(\frac{c_R}{V} - \cos\delta\cos\theta_0\right) + \alpha_1 c_L \sin\delta\right\}$$

$$(2\text{-}16)\quad Q_2^L = \frac{\omega\bar{\sigma}}{2c_L}\left\{\frac{c_R}{V} - \cos\delta\cos\theta_0\right) - \alpha_1 c_L \sin\delta\right\}$$

under the conditions

$$(2\text{-}17)\quad \left|\frac{\omega r_0}{c_L}\right| \gg 1 \qquad \left(\frac{\bar{\sigma}}{r_0}\right) \ll 1 \qquad \left(\frac{c}{r_0}\right) \ll 1$$

2.4 A model for a strike-slip fault in the layer

The geometrical configuration of the fault in this case is clear from figure 23. The integrated effect of the fault is given by the double integral:

$$(2\text{-}18)\quad U_\theta^L = \frac{-iL}{2\mu_1} \sin\theta_0 e^{i\omega t} N_0(\omega) \int_0^b \int_0^\sigma \cos\left[\omega\alpha_1(h_1 + \eta\sin\delta)\right] H_0^{(2)}(\kappa r) e^{-i\omega\frac{\xi}{V}} d\eta\, d\xi$$

which yields

$$(2\text{-}19)\quad U_\theta^L = \frac{L}{2\mu_1\sqrt{2\pi}} \frac{\sin\theta_0}{\sqrt{\kappa r_0}} N_0(\omega) \frac{\sin X_L}{X_L} \left\{ \frac{\sin\Delta_1^L}{\Delta_1^L} e^{i(\omega h_1 \alpha_1 + \Delta_1^L)} + \frac{\sin\Delta_2^L}{\Delta_2} e^{-i(\omega h_1 \alpha_1 - \Delta_2^L)} \right\} e^{i(\varphi_L + \frac{3\pi}{4})}$$

with

$$\varphi_L = \omega\left(t - \frac{r_o}{c_L}\right) - X_L \qquad X_L = \frac{\omega b}{2c_L}\left(\frac{c_L}{v} - \cos\theta_o\right)$$

(2-20)
$$\Delta_1^L = \frac{\omega\sigma}{2c_L}\left(\sin\theta_o \cos\delta + \alpha_1 c_L \sin\delta\right)$$

$$\Delta_2^L = \frac{\omega\sigma}{2c_L}\left(\sin\theta_o \cos\delta - \alpha_1 c_L \sin\delta\right)$$

For a vertical strike-slip fault we substitute $\delta = \frac{\pi}{2}$ in (2-19) to get with $\Delta^L = \frac{\omega\alpha_1(h_2 - h_1)}{2}$

(2-21)
$$U_\theta^L = \frac{L}{\mu_1\sqrt{2\pi}} \frac{\sin\theta_o}{\sqrt{r_o\, {}_nk}} N_o(\omega) \frac{\sin X_L}{X_L} \frac{\sin\Delta^L}{\Delta^L} \cos\left(\omega\alpha_1 \frac{h_1 + h_2}{2}\right) e^{i\left(\varphi_L + \frac{3\pi}{4}\right)}$$

In order to generalize for a radiating dipole we differentiate equation 2-21 with respect to the coordinate y, using the operator $\frac{\partial}{\partial y} = \sin\theta_o \frac{\partial}{\partial r_o} + \frac{\cos\theta_o}{r_o} \frac{\partial}{\partial \theta_o}$ and neglecting terms higher than $r_o^{-\frac{1}{2}}$. We find that the relevent contribution to this order of magnitude comes from differentiating the exponent $e^{i\varphi_L}$. This means that in order to obtain the dipole-displacement from equation 2-21 we have to multiply it by $\frac{\omega}{c_L}\sin\theta_o e^{-\frac{\pi i}{2}}$. Thus we have

(2-22)
$$\left(U_\theta^L\right)_{dipole} = \frac{L}{\mu_1} \frac{\sin^2\theta_o}{\sqrt{r_o}} \sqrt{{}_nk}\, N_1(\omega) \frac{\sin X_L}{X_L} e^{i\left(\varphi_L + \frac{\pi}{4}\right)}$$

$$c_L(-\omega) = c_L(\omega) \qquad {}_nk^{\frac{1}{2}}(-\omega) = {}_nk^{\frac{1}{2}}(\omega)$$

The layering-dependence of U_θ is given by:

(2-23) $$N_1(\omega) = \frac{\sin \Delta^L}{\Delta^L} \frac{N_0(\omega)}{\sqrt{2\pi}} \cos\left(\omega \alpha, \frac{h_1+h_2}{2}\right)$$

Where the "dipole factor" is $\sin^2\theta_0$ whereas we had the factor $\sin 2\theta$ for the leading components of the Rayleigh dipole pattern. The "finiteness-factor" $\frac{\sin X}{X} e^{i\varphi}$ is the same for both waves.

2.5 Transformation into the time domain

We shall now proceed to obtain a theoretical seismogram from equation 2-22. The same method will apply, mutatis mutandis, to any of the expressions in equations 2-13, 2-19 and 2-21.

First we note that the amplitude of $(U_\theta)_{dipole}$ in equation 2-22 is even in ω. Taking the source time-dependence to be that of $\delta(t)$ we get

(2-24) $$\left(U_\theta^L\right)_{dipole}(t) = \frac{L}{\pi \mu_1} \frac{\sin^2\theta_0}{\sqrt{r_0}} \int_0^\infty G(\omega) \cos \omega\tau \, d\omega$$

with $$\tau = t - \frac{r_0}{C_L} - \frac{b}{2C_L}\left(\frac{C_L}{V} - \cos\theta_0\right)$$

(2-25) $$G(\omega) = \sqrt{nK}\ N_1(\omega) \frac{\sin X_L}{X_L} \quad , G(0) = G(\infty) = 0$$

and equation 2-24 can be integrated numerically for any observed dispersion curve $C_L = C_L(\omega)$. This is only an approximation since our solution to the wave-equation

is exact only for a homogeneous mantle but is not an exact solution for the real Earth. There is an apparent difficulty at the lower limit of the integral because we derived our previous theory on the assumption that $\frac{\omega r}{C_L} \gg 1$, thus restricting ω to non-vanishing values. However, the contribution to the integral from values of the integrand at the neighborhood of $\omega = 0$ can be made small enough as compared with the rest of the integral without violating the above restriction.

Kelvin's stationary-phase method may be used to approximate equation 2-24. Using the results given by Pekeris (12) and Newlands (13) we have,

$$K_0 = K(\omega_0) \qquad C_L = C_L(\omega_0)$$

for $\frac{d^2K}{d\omega_0^2} > 0$ and ω_0 - root of $\frac{d}{d\omega}(\omega t - Kr_0) = 0$

$$(2\text{-}26)\quad U_\theta^L(t) \simeq \frac{2L}{\mu_1}\frac{\sin^2\theta_0}{r_0}\frac{G(\omega_0)}{\sqrt{2\pi\left|\frac{d^2K}{d\omega_0^2}\right|}}\cos\left[\omega_0 t - K_0 r_0 - \frac{b\omega_0}{2C_L}\left(\frac{C_L}{V} - \cos\theta_0\right) - \frac{\pi}{4}\right]$$

---

for $\frac{d^2K}{d\omega_0^2} < 0$

$$(2\text{-}27)\quad U_\theta^L(t) \simeq \frac{2L}{\mu_1}\frac{\sin^2\theta}{r_0}\frac{G(\omega_0)}{\sqrt{2\pi\left|\frac{d^2K}{d\omega_0^2}\right|}}\cos\left[\omega_0 t - r_0 K_0 - \frac{\omega b}{2c_L}\left(\frac{c_L}{V}-\cos\theta_0\right)+\frac{\pi}{4}\right]$$

and for $\frac{d^2K}{d^2\omega_m}=0$ with $\begin{cases} U_m \text{ - stationary value of group-velocity} \\ \omega_m \text{ - angular frequency corresponding to } U_m \end{cases}$

$$(2\text{-}28)\quad U_\theta^L(t) \simeq \frac{4L}{\mu_1\sqrt{2\pi}}\frac{\sin^2\theta_0}{r_0^{5/6}}\frac{G(\omega_m)}{\left[\frac{1}{2}\frac{d^3K}{d\omega_m^3}\right]^{\frac{1}{3}}}Ai(u)\cos\left[\omega_m t - r_0 K_m - \frac{b\omega_m}{2c_L}\left(\frac{c_L}{V}-\cos\theta_0\right)\right]$$

$$u = \frac{t-\frac{r_0}{U_m}}{\left[-\frac{r_0}{2}\frac{d^3k}{d\omega_m^3}\right]^{\frac{1}{3}}}$$

Where Ai(u) is the Airy-function defined by $Ai(u)=\int_0^\infty \cos(ut+\frac{1}{3}t^3)\,dt$. The validity-condition for equation 2-28 is given by Pekeris (12). The reader is reminded that our results apply only to the first SH mode and for a single stationary point. In case of n modes and m roots of $\frac{d}{d\omega}(\omega t - K_n r_0) = 0$, a double sum is understood.

2.6 Application to the G-wave

Our findings will be applied to the G-phase which is being repeatedly observed on records of major Earthquakes. This phase appears on seismograms as a long-period SH pulse. It propagates with a rather constant group-velocity of 4.38-4.44 $\frac{Km}{sec}$ (Gutenberg and Richter (14,14a), Benioff (15), Sato (16) and Press (17), and its power is concentrated mainly in the period range 40 T 400. Gutenberg's (18) low-velocity

channel in the upper Mantle provides a possible explanation to the low group-velocity of this phase.

Starting with an assumed constant group-velocity in the above mentioned period-range we integrate the basic relation $U_g = C - \lambda \frac{dC}{d\lambda} = U_o$ to yield $C = \frac{U_o}{1-\alpha_o T}$ (16) with the observed values of $U_o = 4.38\text{-}4.44 \frac{Km}{sec}$ and $\alpha_o = 6 \times 10^{-4} sec^{-1}$ (16,20). The wave number thus becomes a linear function in the angular frequency: $K(\omega) = \frac{1}{U_o}(\omega - 2\pi\alpha_o)$. Being unable to use the stationary-phase approximation, we take the following alternative: (19,20). We put the value of $K(\omega)$ directly into equation 2-24 and integrate between the limits of the spectral window from ω_1 to ω_2. It is observed that $G(\omega)$ in equation 2-24 is a slowly-varying function over the integration range; therefore, after expanding ω about $\bar{\omega}$ and integrating, we have for a first approximation,

$$(2\text{-}29) \qquad U_\theta^L(t) \simeq \frac{2L(\Delta\omega)}{\pi\mu_1} \frac{\sin^2\theta_o}{\sqrt{r_o}} G(\bar{\omega}) \frac{\sin\left\{\frac{\Delta\omega}{2}\Theta\right\}}{\left\{\frac{\Delta\omega}{2}\Theta\right\}} \cos\left(\bar{\omega}\tau_o + \frac{\pi}{4}\right)$$

with

$$(2\text{-}30) \qquad \begin{cases} \Delta\omega = \omega_2 - \omega_1 \qquad \bar{\omega} = \frac{1}{2}(\omega_1 + \omega_2) \qquad \Theta = t - \frac{r_o}{U_o} - \frac{b}{2V} \\ \tau_o = t - \frac{r_o}{C_L(\bar{\omega})} - \frac{b}{2C_L(\bar{\omega})}\left(\frac{C_L(\bar{\omega})}{V} - \cos\theta_o\right) \end{cases}$$

Inspecting equation 2-29 in more detail we find here again the "finiteness-factor" $\frac{\sin X_L}{X_L}$ which has already been encountered in the case of the Rayleigh-waves. $\frac{\sin^2 \Theta_o}{\sqrt{r_o}}$ is the pure "dipole-factor," both factors being fixed on a certain seismogram. The time factor has the form of a cosine wave propagating with a phase velocity corresponding to $\bar{\omega}$. Its amplitude is modulated by the $\frac{\text{"}\sin(\bar{\alpha}t-\bar{\beta})\text{"}}{(\bar{\alpha}t-\bar{\beta})}$ pattern which progresses with the group-velocity U_o. In the former generalization into the time domain we did not take into account the selective absorption which plays a dominant role in shaping the waveform of the G-waves as they circle and recircle the Globe (16). We saw earlier that the G-wave surface-displacement can be generalized into a pulse by integrating the steady-state solution over a finite spectral window from $\omega = \omega_1$, to $\omega = \omega_2$, in which the group-velocity is rather constant. If we introduce into the integrand an exponential decay factor which governs the absorption in the real Earth we have

$$(2\text{-}31) \quad \left\{ U_\theta^L(t) \right\}_n = E_o \frac{\sin^2\theta_o}{\sqrt{\Gamma_o \sin \Delta_n}} G(\bar{\omega}) \int_{\omega_1}^{\omega_2} \omega^{P-1} e^{-\Omega\omega} \cos(\omega\tau_o - K\Delta_n + \delta_o)\, d\omega$$

with $\qquad G(o) = 0 \qquad G(\infty) = 0 \qquad n = 1,2,3,\cdots$

E_o is some real constant, Γ_o is the radius of the Earth and the factor $\frac{1}{\sqrt{\Gamma_o \sin \Delta_n}}$ arises from the asymptotic ex-

pansion of the Legendre-function of a large order, which replaces the Hankel-function in problems of wave propagation over a sphere (21,22,23). This asymptotic expansion is conditioned by $K\Gamma_o \gg 1$. δ_o is a phase angle which includes the constant initial phase (21) and the polar phase shift (22). $\Omega = \frac{n}{2\bar{Q}\ U_o}$ where U_o is the constant value of the group-velocity and $\bar{Q}$ is the average value of Q (16) over the spectral window. n is the order of the surface-wave and Δ_n is the distance along a great circle travelled by a surface-wave of order n. p is a characteristic of the source time-dependence. Since we are dealing with a horizontal dipole we shall have $p = \frac{5}{2}$ for a delta-source and $p = \frac{3}{2}$ for a step-source. Equation 2-31 can be integrated numerically for every desired epicentral distance, and thus the corresponding wave-form can be obtained. The exact evaluation of equation 2-31 is possible in terms of Incomplete Gamma-functions. Under the conditions $n > 2$, $\tau_o > \frac{T_1}{2\pi}$, and $e^{-\Omega\omega_1} \gg e^{-\Omega\omega_2}$ equation 2-31 is approximated by

$$(2\text{-}32) \quad \left\{U_\theta^L(t)\right\}_n = \text{constant} \times \frac{\sin^2\theta_o}{\sqrt{\Gamma_o \sin\Delta_n}} G(\bar{\omega}) \frac{\cos\left(\omega_1\tau_o + tg^{-1}\frac{\tau_o}{\Omega} + \delta_o\right)}{\sqrt{\tau_o^2 + \Omega^2}}$$

Equation 2-32 originally includes an additional term which is similar to equation 2-32 in which ω_1 is replaced by ω_2.

If this term is added, then equation 2-32 will reduce to equation 2-29 as Ω approaches zero. The term $tg^{-1}\frac{\tau_o}{\Omega}$ in equation 2-32 is responsible for the broadening of the G-pulse due to absorption.

CHAPTER III

DERIVATION OF THE SOURCE PARAMETERS FROM THE SPECTRUM OF SURFACE-WAVES

3.1 Introduction

Up to the present time, Mantle Rayleigh-waves and Love-waves have been examined mainly by two methods. By the first method dispersion-curves are utilized to obtain information on the velocity distribution in the Crust and the upper Mantle of the Earth (6). The second method seeks information on the Earthquake-source by the method of phase-equalization (19). This method is based on the notion of seismic point-source and thus *a priori* cannot provide us with any further knowledge which concerns itself with departures from this oversimplified model.

The theoretical results obtained in the former chapters can be used to obtain valuable data on real Earthquake-sources. This is done by introducing two new theoretical entities which are measurable on seismic records, whenever there exists a considerable departure from the point-source model. These are the Directivity function and the differential-phase function.

3.2 Derivation of source parameters from the amplitudes

It was shown in section 1-8 that in the case of a horizontally-moving fault, the amplitude-ratio of two

opposite-going components does depend neither on the source spectrum nor on the layering, since these are cancelled out, while it does depend on the horizontal extension of the source, the velocity of rupture, and the strike of the fault with respect to the line joining the station with the initial epicenter. This function is called henceforth Directivity and is generally given by

$$(3\text{-}1) \quad D = \left| \frac{\frac{c}{v} + \cos\theta_o}{\frac{c}{v} - \cos\theta_o} \; \frac{\sin \frac{\pi b}{\lambda}\left(\frac{c}{v} - \cos\theta_o\right)}{\sin \frac{\pi b}{\lambda}\left(\frac{c}{v} + \cos\theta_o\right)} \right|$$

where C stands for either Rayleigh or Love phase-velocity, whichever is the case. In case that the opposite-going components did not travel the same distance, they should be equalized in order to normalize the Directivity which is defined for equal seismic paths. The Directivity is defined for two different situations: one case in which the waves are studied at two different stations on opposite sides of the fault. The second case is that of surface-waves of different order recorded at a single station. Such are for example Mantle Rayleigh-waves or G-waves which start from the fault both in the direction of faulting and in the opposite direction and thus reach the recording station from two opposite directions. The Directivity does not depend practically on the direction of reception of the Instrument (e.g., orientation of the strain seismograph). This happens because in the case of

Love-waves U_r^L is of the order $\frac{1}{(Kr_o)^{3/2}}$, and for long ranges is negligible in comparison with U_θ^L. The same is true of the azimutal component U_θ^R of the Rayleigh-waves which for long ranges is negligible in comparison with the radial component U_r^R (see equations 1-37 to 1-39 and 2-1 to 2-3). Thus the orientation of the instrument may affect the recorded amplitudes but will not affect the Directivity. This argument does not hold for low or moderate values of Kr_o which is the case for very low frequencies.

The Directivity is equal to unity for the case of a vertical dip-slip fault. It does not depend on the dip angle in case of a strike-slip fault with arbitrary dip angle and is not defined in the case of a dip-slip fault with arbitrary dip angle.

The source parameters v and b are derived from the seismic records in the following way:

After digitizing the proper phases on the records and taking their numerical Fourier-transforms, the amplitude-ratios for a set of selected frequencies are computed and then compared with the theoretical ratio given by equation 3-1, which has been corrected for absorption on different paths. The corrected amplitude-ratios are then drawn vs. the period and compared to theoretical trial-curves. These curves may easily be drawn by computing the theoretical zeros and infinities of equation 3-1. A wide enough spectrum (100-400 sec.) is needed to obtain good

results for the three unknown parameters. A knowledge of the dependence of the phase-velocity and the attenuation coefficient (or Q) on period are needed. Q can be obtained independently using G or Mantle-waves of the same parity. This method will be explained in more detail in Chapter IV.

3.3 Derivation of fault-length from the differential phase

Consider a vertical strike-slip fault of length b which extends vertically from depth h_1 to depth h_2 in a multi-layered half-space. The total surface-wave radiation for the spectral frequency ω is given, according to equations 2-22 and 1-37^a, 1-38^a and 1-39^a:

$$U_\theta^L = \frac{L}{\mu_1} \frac{\sin^2\theta_0}{\sqrt{r_0}} \sqrt{n_K}\, N_m(\omega) \frac{\sin X_L}{X_L} e^{i(\varphi_L + \frac{\pi}{4})} \tag{3-2}$$

$$U_r^R = \frac{L}{\mu_1} \frac{\sin 2\theta_0}{\sqrt{r_0}} \sqrt{K_n}\, g_r^m(\omega) \frac{\sin X_R}{X_R} e^{i(\varphi_R - \frac{3\pi}{4})} \tag{3-3}$$

$$U_z^R = \frac{L}{\mu_1} \frac{\sin 2\theta_0}{\sqrt{r_0}} \sqrt{K_n}\, g_z^m(\omega) \frac{\sin X_R}{X_R} e^{i(\varphi_R + \frac{3\pi}{4})} \tag{3-4}$$

with

$$X_j = \frac{\omega b}{2 c_j} \left(\frac{c_j}{V} - \cos\theta_0\right) \tag{3-5}$$

$$\varphi_j = \omega\left(t - \frac{r_0}{c_j}\right) - X_j \qquad j = L, R \tag{3-6}$$

Equation 3-2 gives the Love-wave pattern while equations 3-3 and 3-4 represent the Rayleigh pattern. The subscript j in equations 3-5 and 3-6 refers to Love or Rayleigh-waves which-

ever is the case. The function N_m has been derived for the simple case of a layer over a half-space in case of Love-waves, and g_r^m and g_z^m has been given for a homogeneous half-space. The source is a horizontal dipole with an harmonic time-dependence. For an arbitrary time-dependence the layering-functions N_m, g_r^m and g_z^m will be multiplied by a suitable factor. The situation for a single-layered half-space is displayed in figure 21. We shall now apply these results to the propagation of Mantle Rayleigh-waves and G-waves around the Globe. Since, at the moment we are concerned only with the phases of these waves, we need only add to equations 3-5 and 3-6 the polar shift P_n (22) and replace r_o by Δ_n. Thus

$$\varphi_n = \omega\left(t_o - \frac{\Delta_n}{C}\right) - \frac{\omega b}{2c}\left(\frac{c}{v} + (-)^n \cos\theta_o\right) \pm 2\pi m_n + P_n \qquad n = 1,2,\cdots \quad 0 \le \theta_o \le 2\pi \tag{3-7}$$

with $m = 0,1,2,\cdots$

$$\begin{cases} \Delta_n = \Delta_1 + \pi\Gamma_o(n-1) & n = 1,3,5,\cdots \\ \quad = \pi n\Gamma_o - \Delta_1 & n = 2,4,6,\cdots \\ P_n = \frac{\pi}{2}(n-1) & n = 1,2,3,\cdots \end{cases} \tag{3-8}$$

Δ_1 is the shortest distance from the source to the station. Equation 3-6 is the phase of a spectral component of a surface-wave of order n (time taken with respect to the origin-time to of the Earthquake). C is the phase-velocity of either G or R-waves, and v is the velocity of rupture. The differential-phase $\partial_1\varphi$ of two opposite-going surface waves is therefore given by

$$(3\text{-}9)\qquad \partial_1\varphi = \frac{\varphi_{n+1}-\varphi_n}{2\pi} = \frac{f}{C}\left(40000 - 2\Delta_1 + b\cos\theta_o\right) + \left(M + \tfrac{1}{4}\right)$$

$M = 0, 1, 2, \cdots$

The slope of $\partial_1\varphi$ vs. f/c will yield the faulting length b provided that θ_o and c(f) are known. An alternative formula may be obtained by taking the differential phase of the second order $\partial_2\varphi$: manipulating with <u>three</u> phases of three waves of consecutive orders, one finds:

$$(3\text{-}10)\qquad \partial_2\varphi = \frac{(\varphi_{n+1}-\varphi_n) + (1 - \frac{\Delta^\circ}{180^\circ})(\varphi_{n+2}-\varphi_n)}{2\pi} = f\frac{b}{C}\cos\theta_o + \text{constant}$$

A special case of equations 3-9 and 3-10 is of interest for practical purposes of deriving the fault-length without having recourse to the phase-velocity function. It is a well-established fact that the G-waves propagate on the flat portion of their group-velocity curve, at least in the period range $150 \leq T \leq 250$ sec. Thus, solving the differential equation $U_g = \text{const.} = U_o$ we obtain $f/C_L = f/U_o - \alpha_o$ where α_o is some constant. Therefore, equation 3-10 reduces to

$$(3\text{-}11)\qquad \partial_2\varphi = f\frac{b}{U_o}\cos\theta_o \qquad + \text{constant}$$

Furthermore, if each G-event is taken with respect to its own arrival-time, we also have

$$(3\text{-}12)\qquad \partial_1\varphi = f\frac{b}{U_o}\cos\theta_o \qquad + \text{constant}$$

which is more convenient to use when only two G-events are available, although less accurate since the time of origin is known to a higher degree of accuracy than the arrival-times of the individual events.

CHAPTER IV

EXPERIMENTAL VERIFICATION OF THE THEORY

4.1 Introduction

In the preceding chapters we presented a theory for the propagation of seismic surface-waves from finite moving sources. It was demonstrated how the fault-length and the velocity of rupture may be derived from the amplitude and the phase-spectra of seismic surface-waves, recorded at a single station. This theory has been examined experimentally with ultrasonic scale models and also applied to the great Chilean Earthquake of May 22, 1960. The model-experiment indicated good agreement with the theory and the results for the Chilean Earthquake agree with field measurements (24) and independent measurements made with other methods (25).

4.2 Experiments with a two-dimensional ultrasonic model

The model-experiments were designed by M. Nafi Toksoz and Frank Press. The model was a circular aluminum plate (6061 T-6) with radius of 12 inches and thickness of 1/16". The equipment and the set up was essentially the same as that described in an earlier paper (26).

The source was a 1/8" solid barium-titanate cylinder, and the receiver was a barium-titanate bimorph transducer. For the sake of convenience the receiver was moved instead

of the source and the records taken at two degree intervals. These records were time-shifted and superposed to obtain the condition for a moving source. This interchange of source and receiver is allowed by the principle of seismic reciprocity. The effective rupture-velocity is obtained by dividing the distance of 2° by the shifting-time. The choice of the shifting-time is arbitrary and hence a convenient way to vary the rupture-velocity. A transient pulse input was used. The output waveforms from the oscilloscope were photographed with a polaroid camera. To get the effect of a source moving toward the receiver the individual records were time-shifted to the right by multiples of $(\Delta t)_1 = \frac{2^{\circ}}{v_f}$, while to get the effect of a source receding from the receiver they were time-shifted to the left by the same amount. C_R is the average Rayleigh velocity in the plate and v_f is the desired faulting velocity. Figure 24 shows the superposed waveform resulting from a source moving toward the receiver with a velocity close to the average Rayleigh-velocity in the plate. The resulting total wave-pattern was almost a replica of the static-source output except for a considerable increase in amplitude. The explanation is simple: successive wavelets are in phase and the signal builds up by constructive interference. On the same figure we displayed for comparison the integrated radiation from the source when receding from the receiver. Since the individual wavelets are no longer in

phase, the totality of the individual pulses resulted in a waveform which was spread over a longer time interval with reduced amplitude. By reducing the 2^{o} recording-interval, even a better contrast between the two waveforms may be achieved. The experiment was carried out for two cases: In the first case the receiver, placed at 120^{o} from the source, was moved over a total distance of 12^{o} (an effective fault of 2.5 inches) with an effective rupture-velocity of $1.4 \times 10^{5} \frac{\text{inch}}{\text{sec}}$. In the second case the receiver was moved only 6^{o} with the same rupture-velocity. In both cases the recording was made at 2^{o} intervals. The superposed waveforms were digitized and Fourier-analysed. Then the amplitude-ratio of the two waveforms was taken for frequencies between $f_1 = 0.08 \times 10^{5}$ cps to $f_2 = 3 \times 10^{5}$ cps at intervals of 0.08×10^{5} cps. This experimental Directivity is plotted against frequency in figures 25 and 27. On the same figures we see the theoretical Directivity. The Directivity is the amplitude-ratio of a spectral component of the approaching-source waveform to a spectral component (of the same frequency) of the receding-source waveform. In our case $\cos\theta = 1$ for the approaching source and $\cos\theta = -1$ for the receding source, therefore the theoretical Directivity is given by:

$$D = \left| \frac{1 + \frac{C_R}{V_f}}{1 - \frac{C_R}{V_f}} \; \frac{\sin \frac{\pi f b}{C_R}\left(1 - \frac{C_R}{V_f}\right)}{\sin \frac{\pi f b}{C_R}\left(1 + \frac{C_R}{V_f}\right)} \right| \qquad (4\text{-}1)$$

where b is the fault-length, f is the frequency and v_f is the rupture-velocity. The zeros of this expression are given by $b\left(\frac{C_R}{v_f} - \cos\theta\right) = n\lambda_n \quad n = 1,2,\cdots$ where n is the order of the interference and λ_n is the corresponding wave-length. Likewise, the infinities of D are given by $b\left(\frac{C_R}{v_f} + \cos\theta\right) = m\lambda_m \quad m = 1,2,\cdots$. By using two or more adjacent infinities, the value of m may be obtained. Thus by locating the positions of the zeros and the infinities of the experimental curves, a first estimate of the rupture velocity v_f and fault-length b was made. Then the theoretical Directivity, as given in equation 4-1, was programmed for various values of b and v_f centered on the primary values just obtained. Those values were finally chosen, which reproduce the experimental curve most faithfully. The results are shown in figures 25 and 27. The absorption-correction and the curvature-dispersion were neglected for the present frequency-range. The average Rayleigh-velocity was measured and found to be $C_R = 1.26 \times 10^5 \frac{\text{inch}}{\text{sec}}$. The final results were b = 1.25 inch and $v_f = 1.9 \times 10^5 \frac{\text{inch}}{\text{sec}}$ for the second case. In addition to the amplitude-ratio method we also used the phases of the opposite-going spectral components to obtain the fault-length.

The complete theory was given in Chapter III. It is shown there that the phase of the approaching source is given by $\varphi_+ = \frac{\pi f b}{C_R}\left(\frac{C_R}{v_f} - 1\right) + 2\pi f\frac{\Delta}{C_R} \pm 2\pi n$ (where Δ is

the distance from the source to the receiver (Δ = 25 inch in the experiment). The phase of the receding source is found to be $\varphi_- = \frac{\pi f b}{C_R}\left(\frac{C_R}{v_f} + 1\right) + 2\pi f \frac{\Delta}{C_R} \pm 2\pi m$. Subtracting these phases from each other, we get the differential phase

(4-2) $$\partial_1 \varphi = \frac{\varphi_- - \varphi_+}{2\pi} = \frac{b}{C_R} f + \text{constant}$$

Thus, the slope of $\partial_1 \varphi$ against the frequency will yield the fault-length b, provided C_R is known. This method was applied to our data and yielded b = 2.1 inch in the first case and b = 1.25 inch in the second case. The situation is represented in figures 26 and 28.

In view of the fact that instrumental determination of fault-length and rupture-velocity were never previously obtainable we consider these results to be a distinct contribution despite differences as large as 25% between the actual and the experimental values of the rupture-velocity. The discrepancy between actual value of $v_f = 1.4 \times 10^5 \frac{\text{inch}}{\text{sec}}$ and the experimental result of $1.9 \times 10^5 \frac{\text{inch}}{\text{sec}}$ may be due to the following experimental and theoretical errors:

(1) The simulation of a continuous rupture by a sequence of moving impulses at finite (2°) intervals.

(2) An error of the order $(\frac{b}{\Delta})^2$ in the theory. In our case this amounts to 10% for b = 12°.

(3) An error of the order $\frac{C_R}{(2\pi f \Delta)}$ in the asymptotic expansion of the Hankel-function (see theory in part I). Substituting our values of Δ = 25 inch $C_R = 1.26 \times 10^5 \frac{\text{inch}}{\text{sec}}$ we get an error of the order of $(\frac{800}{f})$ where f ranges from 0.08×10^5 cps to 3×10^5 cps.

(4) The finite spectral window.

(5) Uncertainties in reading the infinities and zeros from the experimental amplitude-ratio curves.

(6) Errors introduced in digitizing the records, especially where amplitudes were extreme or low.

(7) Neglecting the dispersion due to the curvature of the model.

It should be mentioned that the particular waveform of the source-transient has no bearing on the results, since the spectrum of the source does not enter the Directivity function nor the expression for the differential phase.

Computations were executed on the Bendix G-15D electronic computer at our laboratory.

4.3 The great Chilean Earthquake of May 22, 1960

(Magnitude M = $8\frac{1}{4}$ - $8\frac{1}{2}$. Time of origin 0 = 19-11-20)

The Directivity and the differential-phase methods may be applied to Mantle Rayleigh-waves and G-waves from major Earthquakes. These waves circle the Earth many times, both in the direction of the moving fault and in the opposite

direction, and thus provide us with the necessary data for our theory. Extensive field measurements were carried out by P. St Amand. He describes the situation there (24) at the time and after the occurrence of the shocks: "The fault runs parallel to the coast about 20 to 50 kilometers off-shore for a distance of 1000-1200 Km. The rupture began to slip at the south end of the Arauco Peninsula and the rupture propagated southward to a point just north of the Taitao Peninsula. The movement was probably right-lateral, but the vertical component was such that the seaward side went up maybe 5 meters with respect to the landward side."

These observations have been confirmed by other investigators: From measurements of the phase-angle between the horizontal and the vertical components of the free vibration of the Earth, Benioff, et al (25) were able to recover a fault-length of about 1000 Km and a rupture-velocity of 3-4 $\frac{\text{Km}}{\text{sec}}$. The fault lengths are in agreement with Benioff's measurements from the after-shock sequences and the Eaton measurement from the T-phase duration. All these findings together suggest that we have here an obvious case of a horizontally moving source with a predominating strike-slip character for which we have previously built a complete theory.

4.3.1 Data processing

In table I we have summarized the data used for our computations. This includes the geographical data of the stations, the chosen phases and the character of the instruments. The geometry of the station-net with respect to the fault is given in figure 29. First p-arrivals yielded an epicenter at $38^{\circ}00'$S $73^{\circ}30'$W and Benioff's aftershock theory together with field measurements indicated a fault striking at $9^{\circ} \pm 2^{\circ}$ West of South. Identification of the various phases on the seismogram were made in the following manner: Rayleigh-waves were identified by their dispersion curve. G-waves were identified by travel-times and character. Dubious phases were rejected. To fit the data for the Fourier analysis, the chosen phases on the seismograms were digitized manually. All Rayleigh phases were windowed between fixed group-velocities of $U_g = 3.90 \frac{Km}{sec}$ and $U_g = 3.47 \frac{Km}{sec}$. Most of the G-arrivals fitted a group-velocity of $4.38\text{-}4.44 \frac{Km}{sec}$. The broadening of the G-pulse per revolution around the Globe was found to be about 60 sec, measured from the first to the second peak of the G-pulse (see equation 2-32).

In table I, G_2 stands for a G-wave which travelled from the source to the station along the major arc, G_4 is the same wave circling the Earth once more. R_3 for example, is a Mantle Rayleigh-wave travelling along the shortest arc from the source to the station plus one revolution around

TABLE I. STATIONS, PHASES AND INSTRUMENTS

	Latitude	Longitude	Δ°	Km	Azimuth	θ_o	Phases	Instruments
Nana (Peru)	$11^\circ 50' 00''$	$76^\circ 33' 00''$	26.19°	= 2914.7	353.22°	$16^\circ \pm 2^\circ$	G_2, G_4, G_5, G_6	Strain-seismograph N $39^\circ 02'$ E (same as Isabella)
Pasadena (Calif.)	$34^\circ 08' 54''$	$118^\circ 10' 18''$	82.91°	= 9228.9	324.01°	$45^\circ \pm 2^\circ$	R_1, R_2, R_3, R_4 G_2, G_4	Low-magnification strain seismograph, EW with galvanometer-period of T_o = 180 sec
Isabella (Calif.)	$35^\circ 39' 48''$	$118^\circ 28' 24''$	84.30°	= 9383.8	324.66°	$45^\circ \pm 2^\circ$	G_2, G_3, G_4	Strain-seismograph N 32° W with displacement transducer and one stage integrating-network

the Globe. Since in the Chilean Earthquake the fault-rupture with respect to our three stations was in the direction of surface-waves with even orders, we should have expected to see on the seismogram the same effect as mentioned before in connection with our model experiments (fig. 24). This effect, which in fact demonstrates beyond doubt the motion of the seismic source, is shown in figure 46 where R_1 is compared with R_2. In spite of the fact that the Earth (unlike our two-dimensional model) is a strong dispersive and absorptive medium, the resemblance between the situation in figure 24 to that in figure 46 is striking. Figure 47 shows the events recorded at Isabella on Benioff's strain seismograph. Figure 48 displays the G-waves recorded at Nana.

Table II summarizes the data used for the Fourier-analysis. The analysis was performed between the frequency $f_1 = 10^{-3}$ cps to $f_2 = \frac{1}{3}x10^{-1}$ cps with $\Delta f = \frac{1}{2}x10^{-3}$ cps. It was not useful to digitize longer portions of the seismic events because of the risk of overlapping G and R phases. Consequently, our spectra for periods which surpass the mean record-length (about 500 sec) are not reliable. The resulting amplitude-spectra of our phases are shown in figures 32 to 38. The shift of the dominant period to higher periods with the increase of order of the surface-wave is clearly seen. Computations were executed on the IBM 709 computer at the Western Data Processing Center, UCLA.

TABLE II. DATA FOR FOURIER-ANALYSIS

Station	Phase	Digitizing time-interval in sec	Record-length (in sec)
Nana	G_2	12	312
Nana	G_4	15	465
Nana	G_5	15	435
Nana	G_6	15	525
Isabella	G_2	12	350
Isabella	G_3	12	288
Isabella	G_4	12	495
Pasadena	G_2	16	320
Pasadena	G_4	16	435
Pasadena	R_1	16	195
Pasadena	R_2	16	608
Pasadena	R_3	16	672
Pasadena	R_4	16	1200

4.3.2 Recovering the absorption-coefficient from the amplitude-spectrum

We shall see later that for the derivation of the fault parameters, one has to correct the spectral amplitudes of the G and R phases for absorption on different paths. Hence a knowledge of the absorption-coefficient as a function of frequency is needed. The amplitude of a spectral component of a seismic phase may be described

by $A_1 = A_o e^{-\bar{\gamma}\Delta_1}$ where A_1 is the amplitude as read from the Fourier-analysis and A_o is the actual amplitude at the source. By comparing this amplitude with another amplitude of the same spectral component $A_2 = A_o e^{-\bar{\gamma}\Delta_2}$, belonging to the same wave-train which has reached the distance Δ_2, we get, by eliminating A_o:

(4-3) $$\bar{\gamma}(f) = \frac{\log_e 10}{\Delta_2 - \Delta_1} \log_{10} \left| \frac{A_1}{A_2} \right|$$

We have used this formula to compute $\bar{\gamma}_L$ for the G-events from the amplitude-spectra of G_2, G_4, G_6 of the Nana Station, G_2, G_4 of the Isabella Station and G_2, G_4 of Pasadena. All the results are in fair agreement as seen in figure 30. In the same way we have evaluated $\bar{\gamma}_R$ for Mantle Rayleigh-waves using (R_1, R_3) and (R_2, R_4) recorded at Pasadena. Results are given in figure 31. The results for the G-wave are slightly lower, at the high-frequency end of our spectrum than those obtained by Sato (16) for the Kamchatka Earthquake. This might be partly explained by the fact that in the Kamchatka Earthquake the wave-path was mostly oceanic while in the Chilean Earthquake it was an evenly-mixed path of continents and oceans.

4.3.3 Recovering the Rayleigh and Love phase-velocities from the phase-spectrum

Phase-velocities, we well as absorption-coefficients are essential for deriving the fault parameters from the

spectra of our seismic events. The phases of our surface-waves are:

$$\frac{1}{2\pi}\varphi_{n+2} = f\left(t_0 - \frac{\Delta_{n+2}}{c}\right) - \frac{fb}{2c}\left(\frac{c}{v} + (-)^{n+1}\cos\theta_0\right) \pm M_{n+2} + P_{n+2}$$

(4-4)

$$\frac{1}{2\pi}\varphi_n = f\left(t_0 - \frac{\Delta_n}{c}\right) - \frac{fb}{2c}\left(\frac{c}{v} + (-)^{n}\cos\theta_0\right) \pm M_n + P_n$$

$$n = 1,2,3,\cdots$$

Here φ_n is the phase of a surface-wave of order n, M_n is an integer, P_n is the polar phase shift (22). Δ_n is the distance traversed by the particular phase in question and t_n is the time of arrival of the phase to Δ_n with respect to the time of origin.

Subtracting these phases from each other and denoting $\partial\varphi = \frac{1}{2\pi}(\varphi_{n+2} - \varphi_n)$ and $t_{n+2} - t_n = \partial t$ we have, upon solving for C:

$$C = \frac{40,000}{\partial t - T(\partial\varphi + M - \frac{1}{2})} \quad \frac{\text{Km}}{\text{sec}} \qquad (4\text{-}5)$$

In case of the Mantle Rayleigh-waves we have used the phases R_4 and R_2 recorded at Pasadena. We had $\partial t = 10804$ sec. With this value, equation 4-5 has been programmed for various integral values of M. The results are shown in table III. We have finally chosen the value M = 10 as it gave results for the low frequencies which agreed with the high modes of the spheroidal free vibrations of the Earth (25). Our results also agree with those obtained by J. Brune (21). The dependence of the phase-velocity upon the period T is shown in figure 40. The same procedure was used for the phase-velocities of Love-waves with $\partial t = 9090$ sec. Results for some values of M are given in table IV.

TABLE III. PHASE-VELOCITIES OF RAYLEIGH-WAVES

FROM PASADENA $R_4 - R_2$

Frequency $\times 10^{-3}$ cps	Period in sec	Phase difference 2	Phase-velocity Km/sec M=9	M=10	M=11
2	500	0.050	6.42	6.98	7.23
2.5	400	0.110	5.65	5.98	6.09
3	333.3	0.990	5.23	5.47	5.73
3.5	285.7	0.982	4.94	5.12	5.31
4	250	1.136	4.76	4.91	5.00
4.5	222.2	1.495	4.66	4.78	4.91
5	200	1.700	4.56	4.67	4.78
5.5	181.8	1.808	4.48	4.57	4.67
6	166.6	1.833	4.40	4.88	4.57
6.5	153.8	1.963	4.35	4.42	4.50
7	142.8	2.103	4.30	4.37	4.44
7.5	133.3	2.215	4.26	4.32	4.39
8	125	2.420	4.23	4.29	4.35
8.5	117.6	2.694	4.21	4.27	4.32
9	111.1	2.835	4.19	4.24	4.29
9.5	105.2	2.950	4.16	4.21	4.26
10	100	2.953	4.14	4.18	4.23
10.5	95.2	2.974	4.12	4.16	4.20
11	90.9	2.940	4.09	4.13	4.17
11.5	86.9	2.950	4.07	4.11	4.15
12	83.3	3.319	4.07	4.11	4.14
12.5	80.0	3.402	4.06	4.09	4.12
13	76.9	3.364	4.04	4.07	4.10
13.5	74.1	3.366	4.03	4.06	4.09
14	74.4	3.552	4.02	4.05	4.08
14.5	68.9	3.740	4.01	4.04	4.07
15	66.6	3.798	4.00	4.03	4.06
15.5	64.5	3.753	3.99	4.02	4.04
16	62.5	3.750	3.99	4.02	4.04
16.5	60.6	4.122	3.98	4.01	4.03
17	58.8	4.276	3.98	4.01	4.03
17.5	57.1	4.923	3.98	4.00	4.03
18	55.5	4.984	3.97	4.00	4.02
18.5	54.0	5.020	3.97	4.00	4.02
19	52.6	5.670	3.97	3.99	4.02
20	50	5.612	3.96	3.98	4.00

TABLE IV. PHASE-VELOCITIES OF LOVE-WAVES

FROM ISABELLA $G_4 - G_2$

Frequency $\times 10^{-3}$ cps	Period in sec	Phase difference 2	Phase-velocity Km/sec M=3	M=4	M=5	M=6
2	500	0.112	5.10	5.45	5.85	6.31
2.5	400	0.158	4.95	5.20	5.49	5.81
3	333.3	0.207	4.85	5.05	5.28	5.52
3.5	285.7	0.259	4.78	4.95	5.14	5.33
4	250	0.320	4.74	4.88	5.04	5.20
4.5	222.2	0.392	4.70	4.83	4.96	5.10
5	200	0.484	4.68	4.79	4.91	5.03
5.5	181.8	0.600	4.66	4.76	4.86	4.97
6	166.6	0.717	4.64	4.73	4.83	4.93
6.5	153.8	0.816	4.63	4.71	4.80	4.89
7	142.8	0.908	4.62	4.69	4.77	4.86
7.5	133.3	1.000	4.61	4.68	4.75	4.83
8	125.0	1.116	4.60	4.67	4.73	4.81
8.5	117.6	1.290	4.59	4.66	4.72	4.79
9	111.1	1.787	4.61	4.66	4.72	4.80
9.5	105.2	1.891	4.60	4.66	4.72	4.78
10	100	1.976	4.60	4.65	4.70	4.76
10.5	95.24	2.060	4.59	4.64	4.69	4.74
11	90.09	2.147	4.58	4.63	4.68	4.73
11.5	86.96	2.221	4.58	4.62	4.67	4.72
12	83.33	2.264	4.57	4.61	4.66	4.70
12.5	80.0	2.295	4.56	4.60	4.65	4.69
13	76.92	2.350	4.56	4.60	4.64	4.68
13.5	74.07	2.440	4.55	4.59	4.63	4.67
14	71.43	2.563	4.55	4.59	4.63	4.66
14.5	68.92	2.695	4.55	4.58	4.62	4.66
15	66.67	2.816	4.55	4.58	4.62	4.65
15.5	64.52	2.932	4.54	4.58	4.61	4.65
16	62.50	3.066	4.54	4.58	4.61	4.64
16.5	60.61	3.218	4.54	4.57	4.61	4.64
17	58.82	3.381	4.54	4.57	4.60	4.64
17.5	57.14	3.521	4.54	4.57	4.60	4.63
18	55.56	3.633	4.54	4.57	4.60	4.63
18.5	54.05	3.718	4.54	4.57	4.59	4.62
19	52.63	3.785	4.53	4.56	4.59	4.62
20	50	3.851	4.53	4.55	4.58	4.61

The value M=5 was chosen because of the agreement of the results with the high modes of the torsional free vibrations of the Earth. Comparison of the resulting phase-velocities with those obtained by the formula $C = \frac{U_o}{1-\alpha_o T}$ (which holds only for a region of constant group-velocity U_o) shows that with $\alpha_o = 6 \times 10^{-4}$ sec^{-1} (see sec. 2.6) there is good agreement in the period interval $250 > T > 100$ sec. This may serve as indirect evidence that the group-velocity is indeed practically constant in this region, and thus justifies an assumption made later in connection with the derivation of the fault-length from the differential phase. Figure 39 displays the variation of the phase-velocity of Love-waves against the period .

4.3.4 Deriving the source parameters from the Directivity of long-period surface-waves

Having computed the phase-velocities and the absorption coefficients from the spectra we are now ready to approach the final step. It has been shown in section 3.2 that the Directivity for a particular frequency of two opposite-going surface-waves, resulting from a strike-slip fault is given by:

$$(4\text{-}6)' \qquad D = \left| \frac{\left(\frac{c}{V} + \cos\theta_o\right)}{\left(\frac{c}{V} - \cos\theta_o\right)} \frac{\sin \frac{\pi b f}{c}\left(\frac{c}{V} - \cos\theta_o\right)}{\sin \frac{\pi b f}{c}\left(\frac{c}{V} + \cos\theta_o\right)} \right|$$

In order to be able to use this expression, we first obtained amplitude-ratios from the spectra. Then these ratios were

multiplied by a correction factor to equalize for absorption on different paths as shown in table V: $\bar{\gamma}_L$ is given in figure 30 and $\bar{\gamma}_R$ is given in figure 31.

TABLE V. THE ABSORPTION CORRECTION

Station	Ratio used	Path difference $360^\circ - 2\Delta,^\circ$	Absorption-correction factor
Nana	G_6/G_5	34170.6 Km	$+(10^4\,\bar{\gamma}_L)3.4171$
Pasadena	R_2/R_1	21542.0 Km	$+(10^4\,\bar{\gamma}_R)^{2.1542}$
Isabella	G_4/G_3	21233.1 Km	$+(10^4\,\bar{\gamma}_L)2.1233$

The corrected amplitude-ratios are plotted against the frequency f in figures 41 to 43. From the position of the zeros and infinities of these curves a first estimate of the fault-length b and the rupture-velocity can be made. This is rather easy since the zeros of the Directivity function are given by $b\,(\frac{c}{v} - \cos\theta_o) = n\lambda_n \quad n = 1,2,\cdots$ where n is the order of interference. Likewise, the infinities are given by $b\,(\frac{c}{v} + \cos\theta_o) = m\lambda_m \quad m=1,2,\cdots$. By using two or more adjacent infinities, the value of m may be obtained. As a next step the theoretical Directivity has been programmed for various values of b and v centered on the primary values obtained earlier. We have chosen finally those values which reproduced the experimental curve most faithfully. The results are shown in figures 41 to 43. The fit of the experimental to the theoretical

curves is satisfactory. To demonstrate the fidelity of our results we have programmed the theoretical Directivity in one case (broken line in fig. 43) for a fault-length of b = 500 Km and a rupture-velocity of $v = 4.5 \frac{Km}{sec}$ and in another case (dotted line in fig. 43) for b = 750 Km and $v = 2 \frac{Km}{sec}$. The resulting curves do not match the experimental curves. Final results are given in table VI. The amplitude-spectra measurements indicate an average fault-length of 800 Km and a velocity of rupture of $4.5 \frac{Km}{sec}$.

4.3.5 Deriving fault-length from differential-phase

The theory of the differential phase is given in section 3.3 and was reviewed in connection with the model experiments in section 4.2. Since the spectral region $250 > T > 100$ is a region of constant group-velocity for Love-waves, equation 3-12 can be used to recover the fault length b with no further computations. In figure 44 we have plotted the phase (exactly as it came out from the Fourier-analysis) of G_4 and G_3 of Isabella against frequency. The fault-length b is directly obtainable from the slope of the line which is the difference of the two lines shown in figure 44. Figure 45 shows the same situation for the phases of G_6 and G_5 recorded at Nana, Peru. The results are assembled in table VI.

TABLE VI. FINAL RESULTS FOR THE SOURCE PARAMETERS

Station	Type of wave	Fault length (Km) From Directivity	Fault length (Km) From differential-phase	Rupture velocity $\frac{Km}{sec}$
Nana	G	800	850	4.5
Isabella	G	750	1300	4.5
Pasadena	R	750	-	4.5

4.4 Discussion of the results

Comparing the results of our computations as given in table VI we see that except for one value they are rather consistent, indicating a fault of about 800 Km and a rupture velocity of 4.5 $\frac{Km}{sec}$. Our results are susceptible to three types of errors:

(1) Deviations of the actual Earthquake-mechanism, which took place in the Chilean Earthquake from our theoretical model such as: zig-zag faulting with variable rupture velocity, bidirectional faulting and other possible deviations from the pure strike-slip model.

(2) Errors introduced in preparing the data for the Fourier-analysis such as imperfect separation of the individual events, the use of a finite spectral window, overlapping of G and R events on the seismogram, digitizing low-amplitude regions or regions of extreme amplitudes on the record.

(3) Errors in the fault azimuth. This angle was given by Benioff, et al. (25) and derived by them from the location of after-shocks sequence of the main Earthquake.

This study was hampered by the large variations in the amplitudes of the recorded waves, and the wave interferences which took place in this great Earthquake. If greater dynamic ranges were available together with higher recording speeds, then more accurate results could have been obtained.

4.5 Conclusion

Our model experiments and analysis of records of the Chile Earthquake of May 22, 1960 have shown that the theory proposed in chapters I-III is applicable to seismic wave-propagation from finite moving sources. Our theory was able to explain the asymmetrical radiation pattern from Earthquake-faults and derive from it some important and previously elusive parameters of the source. The main features of our method are its simplicity, straightforwardness and efficiency. It may serve to associate many Earthquakes with at least two important parameters and thus be of great use in exploring the mechanism at the focus and the nature of the Earth's interior. Moreover, the dependence of the surface-wave amplitudes on the vertical extent of the source were already indicated in

most of the results of chapter I and chapter II. In future work we intend to generalize our theory to fit the real Earth and thus be able to derive the vertical extent of the faulting as well as its length. Because of the possible errors indicated earlier, one should treat the derived quantities as rough values since their physical meaning is probably not sharply defined. We hope that future comparisons between measurements and the theory may point up ways to improve the theory, so as to cope with more realistic Earthquake-mechanisms.

Our present work has, however, another aspect which extends beyond its immediate applicability to the derivation of fault-lengths and rupture-velocities, and that is the notion that the classical point-source picture is no longer adequate as a model for most Earthquakes. The finiteness and the motion of the source have their bearing on many measurements from Earthquake records and ignoring them can lead to serious errors (e.g., calculations of phase and group-velocities from readings of a single station, the concept of an "epicenter," etc.). Earthquake seismologists must from now on let this new dimension enter their way of thinking.

LEGEND OF FIGURES

Fig. 1 Horizontal force in an elastic half-space.

Fig. 2 The Rayleigh pole in the complex K-plane.

Fig. 3 The geometry of the horizontal strike-slip fault in the half-space.

Fig. 4 The motion of the source relative to the station.

Fig. 5 The geometry of the vertical strike-slip fault in the half-space.

Fig. 6 The geometry of the dip-slip fault.

Fig. 7 The geometry of the strike-slip fault.

Fig. 8 The function $\frac{\sin X}{X}$.

Fig. 9-14 Azimuthal dependence of the radial Rayleigh displacements for various values of the parameters T, b and $\frac{C_R}{v}$. Arrow indicates the direction of dipole motion.

Fig. 15-17 The dependence of the radial Rayleigh displacements on the period for various values of the velocity ratio $\frac{C_R}{v}$, and four different values of the azimuth angle.

Fig. 18-20 The dependence of the radial Rayleigh displacement of the velocity ratio $\frac{C_R}{v}$ for various values of the period, and four different values of the azimuth angle.

Fig. 21 Horizontal force in a layer on top of an elastic half-space.

Fig. 22 The geometry of the dip-slip fault inside the layer.

Fig. 23 The geometry of the strike-slip fault inside the layer.

Fig. 24 Model experiment: plate Rayleigh-waves from moving source. Upper waveform: source moving toward receiver. Lower waveform: source receding from receiver.

Fig. 25 Model experiment: theoretical vs. experimental Directivity for the case b = 2.5 inch $v_f = 1.4 \times 10^5 \frac{\text{inch}}{\text{sec}}$.

Fig. 26 Model experiment: differential phase for the case b = 2.5 inch $v_f = 1.4 \times 10^5 \frac{\text{inch}}{\text{sec}}$.

Fig. 27 Model experiment: theoretical vs. experimental Directivity for the case b = 1.25 inch $v_f = 1.4 \times 10^5 \frac{\text{inch}}{\text{sec}}$.

Fig. 28 Model experiment: differential phase for the case b = 1.25 inch $v_f = 1.4 \times 10^5 \frac{\text{inch}}{\text{sec}}$.

Fig. 29 The geometry of the station-net and the fault of the great Chilean Earthquake of May 22, 1960.

Fig. 30 Chile Earthquake: Love-wave absorption coefficient vs. frequency.

Fig. 31 Chile Earthquake: Mantle Rayleigh-waves absorption-coefficient vs. frequency.

Fig. 32-38 Chile Earthquake: amplitude-spectra of the digitized events. Amplitude units are arbitrary and differ from one station to another.

Fig. 39 Chile Earthquake: phase-velocity of Love-waves vs. period.

Fig. 40 Chile Earthquake: phase-velocity of Rayleigh-waves vs. period.

Fig. 41 Chile Earthquake: theoretical vs. observed Directivity. Isabella G_4/G_3.

Fig. 42 Chile Earthquake: theoretical vs. observed Directivity. Nana G_6/G_5.

Fig. 43 Chile Earthquake: theoretical vs. observed Directivity. Pasadena R_2/R_1.

Fig. 44 Chile Earthquake: differential phase for Isabella G_4-G_3.

Fig. 45 Chile Earthquake: differential phase for Nana G_6-G_5.

Fig. 46 Chile Earthquake: Mantle Rayleigh-waves R_1 and R_2 recorded on the Pasadena Low-Magnification strain seismograph.

Fig. 47 Chile Earthquake: Mantle Rayleigh-waves and G-waves recorded on the Isabella strain seismograph.

Fig. 48 Chile Earthquake: G-waves from Nana.

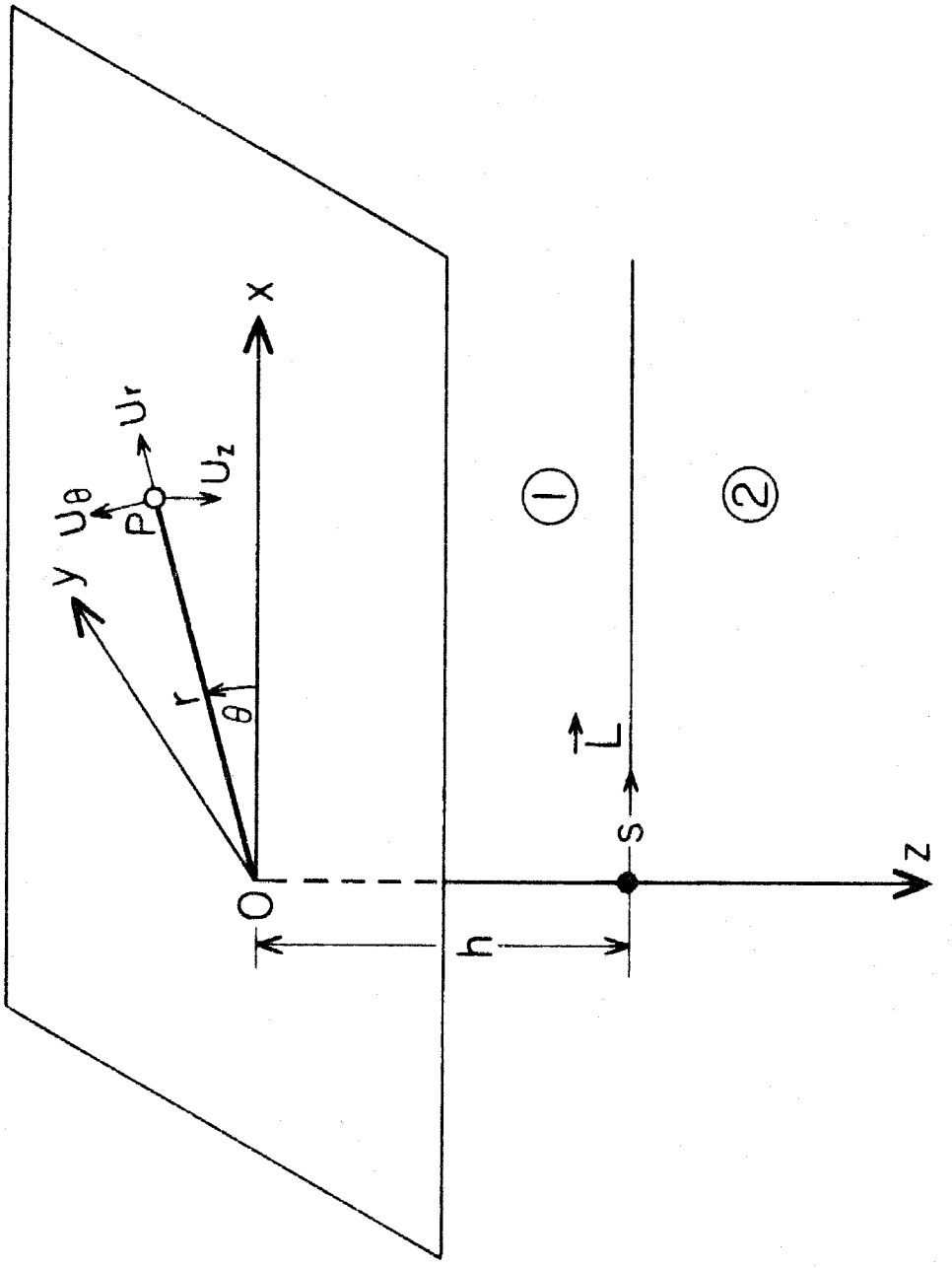

Fig. 1

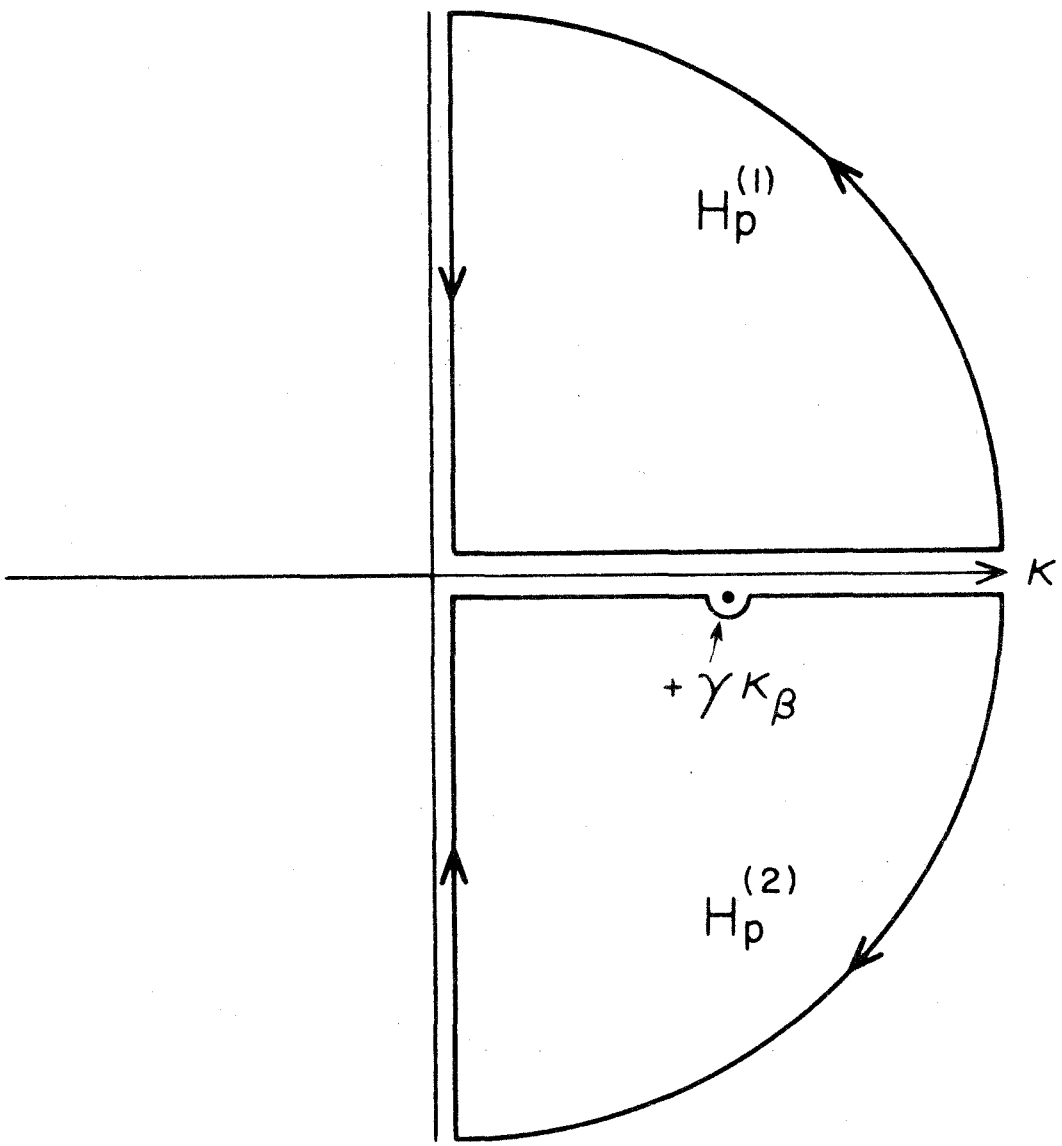

Fig. 2

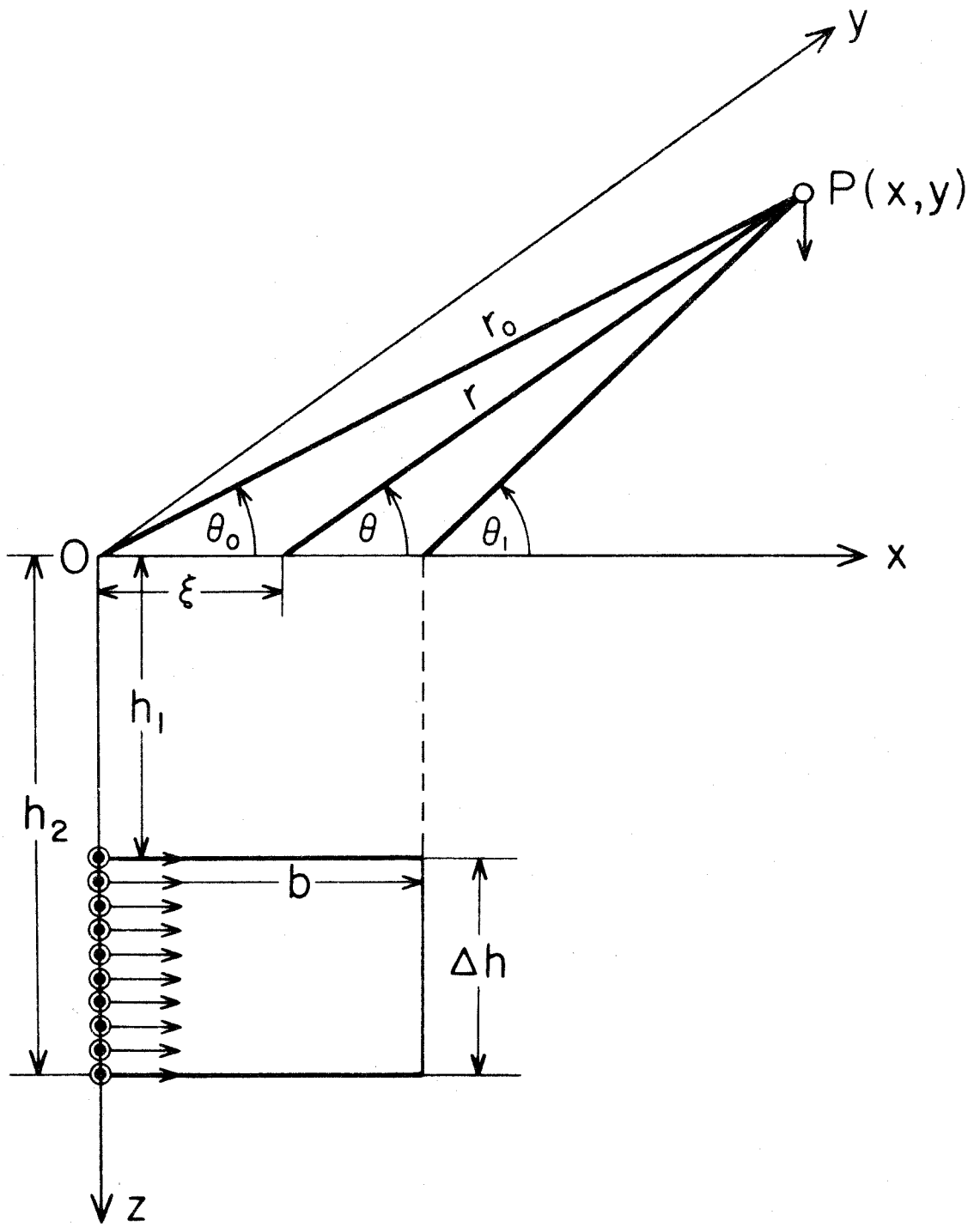

Fig. 3

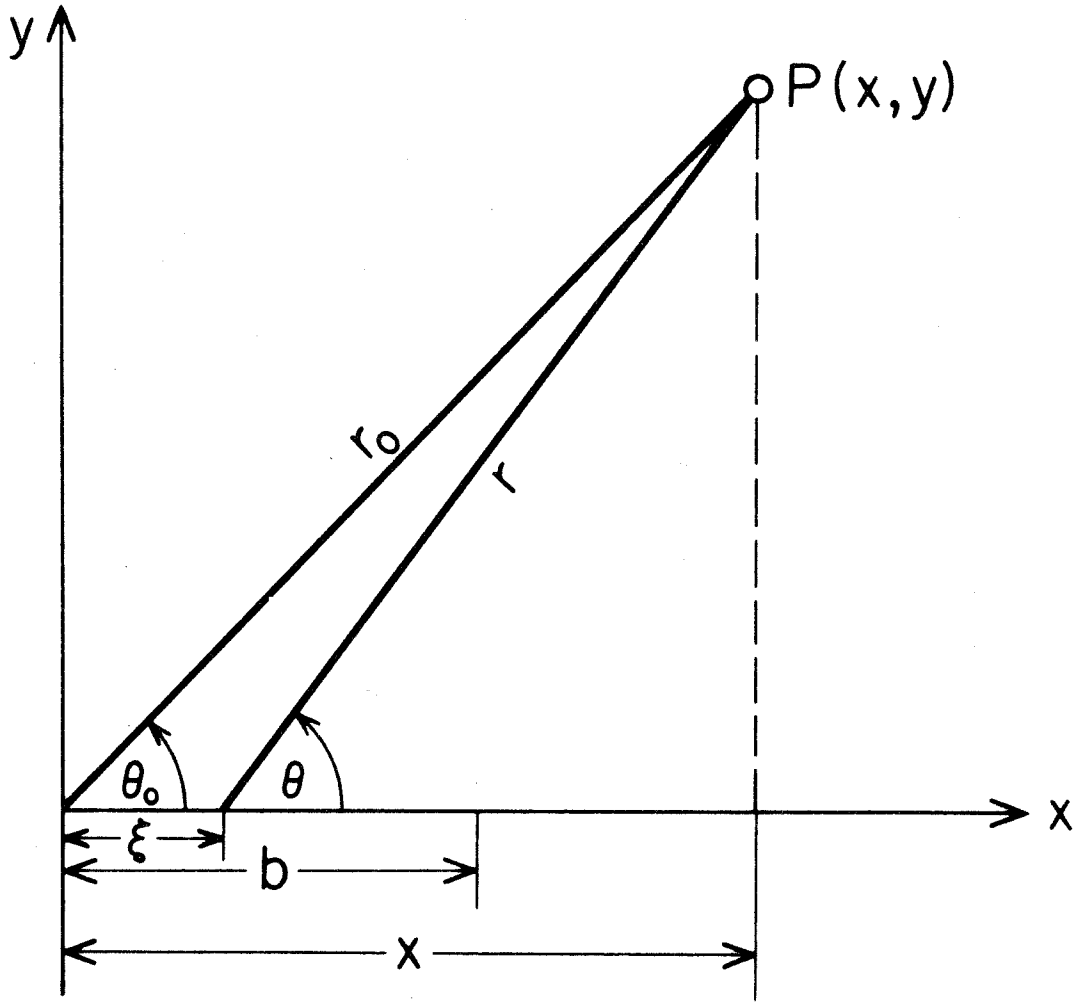

Fig. 4

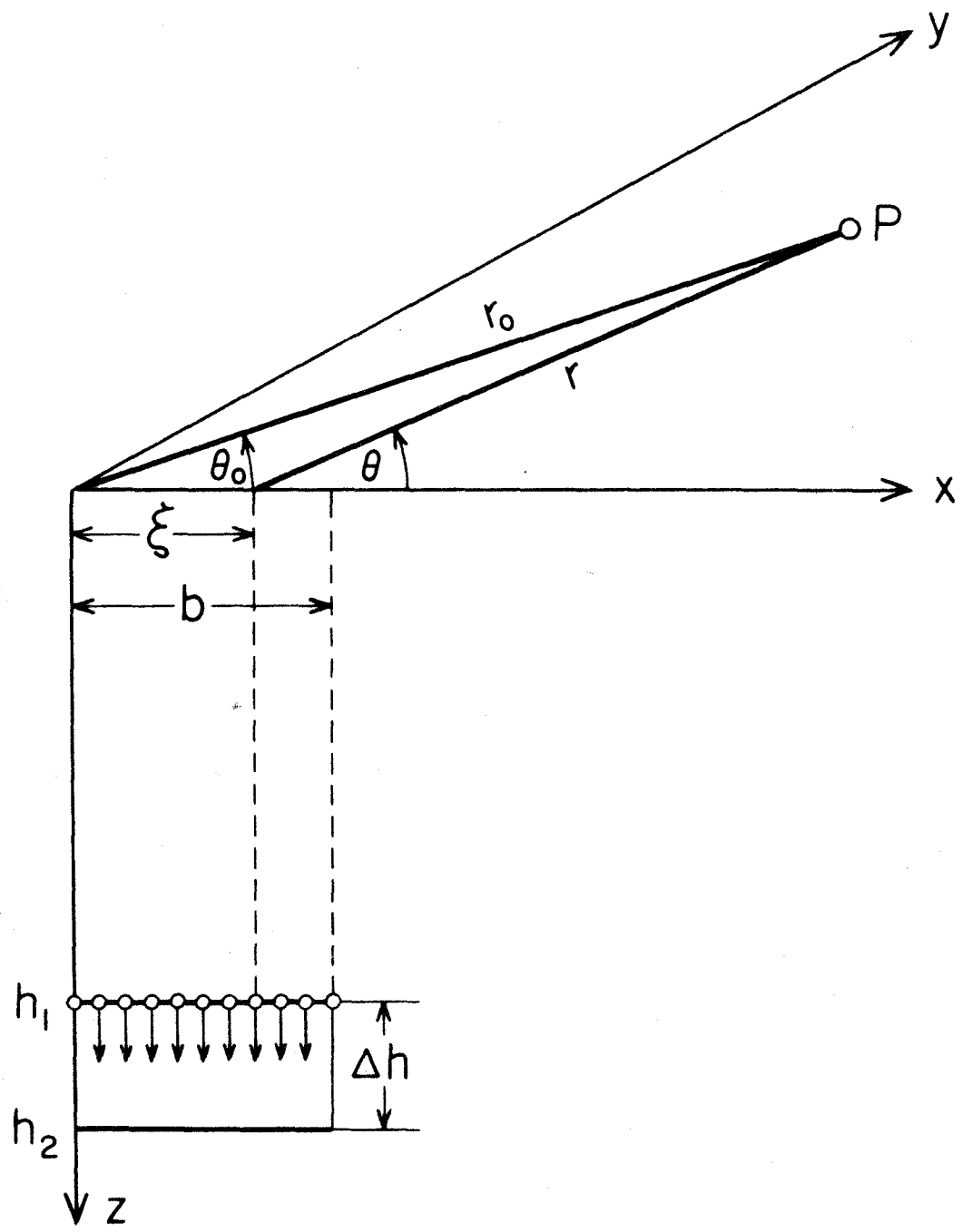

Fig. 5

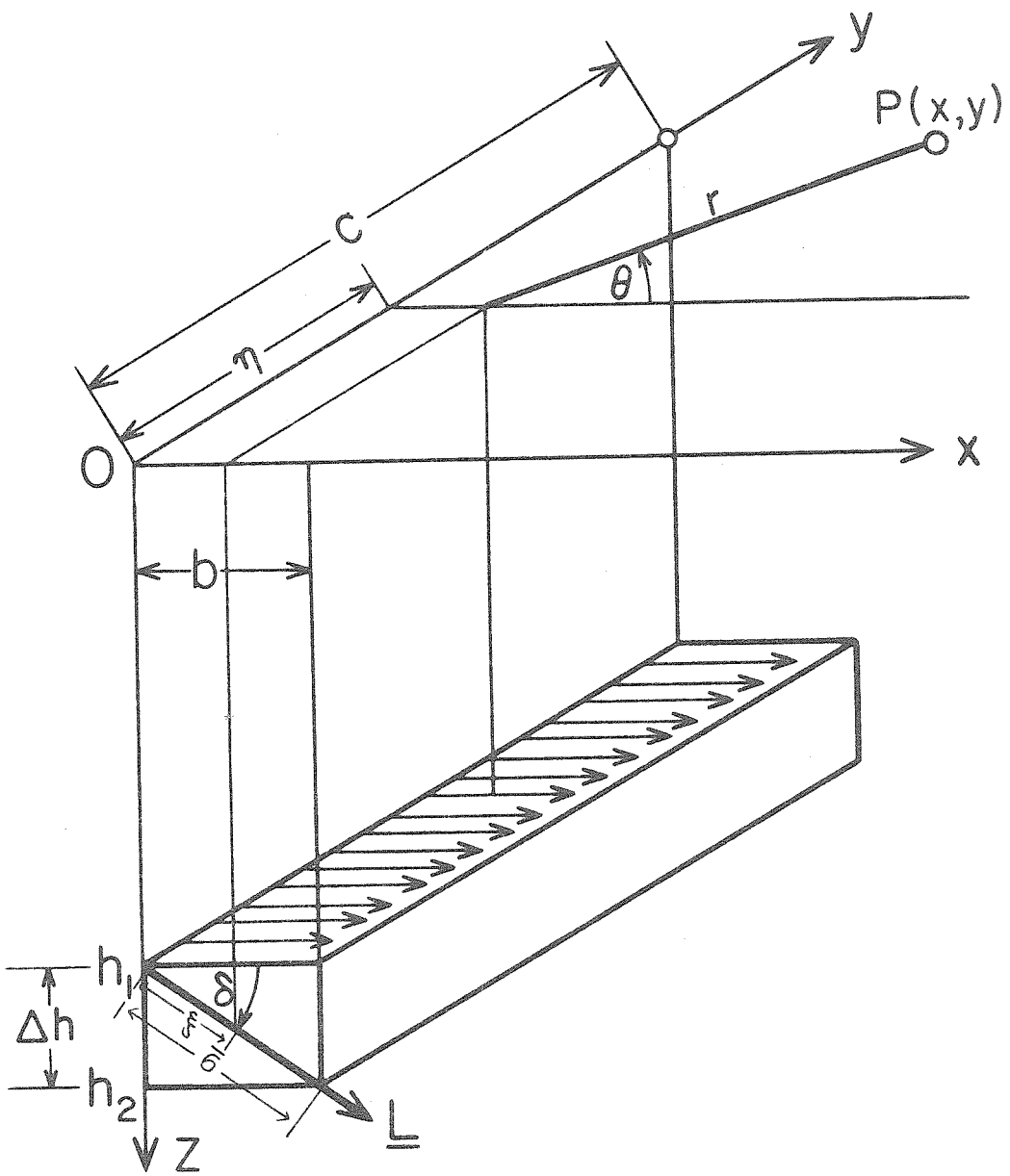

Fig. 6

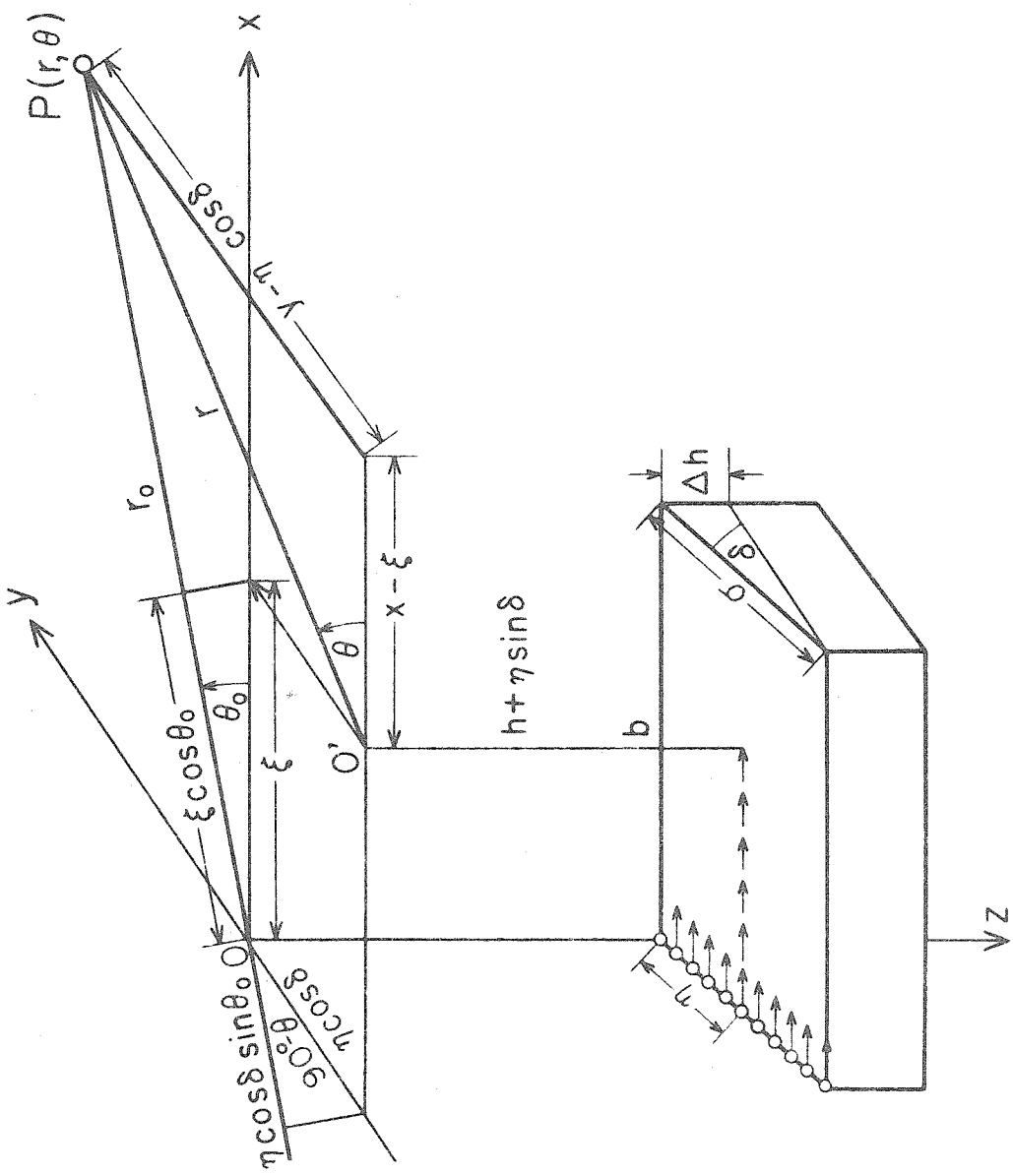
P(r,θ)
x
y
z
r
r₀
θ
θ₀
ξ
x - ξ
y - η cosδ
ξ cosθ₀
η cosδ sinθ₀
η cosδ
90°-θ₀
h + η sinδ
b
O
O'
Δh
δ
ρ
L

Fig. 7

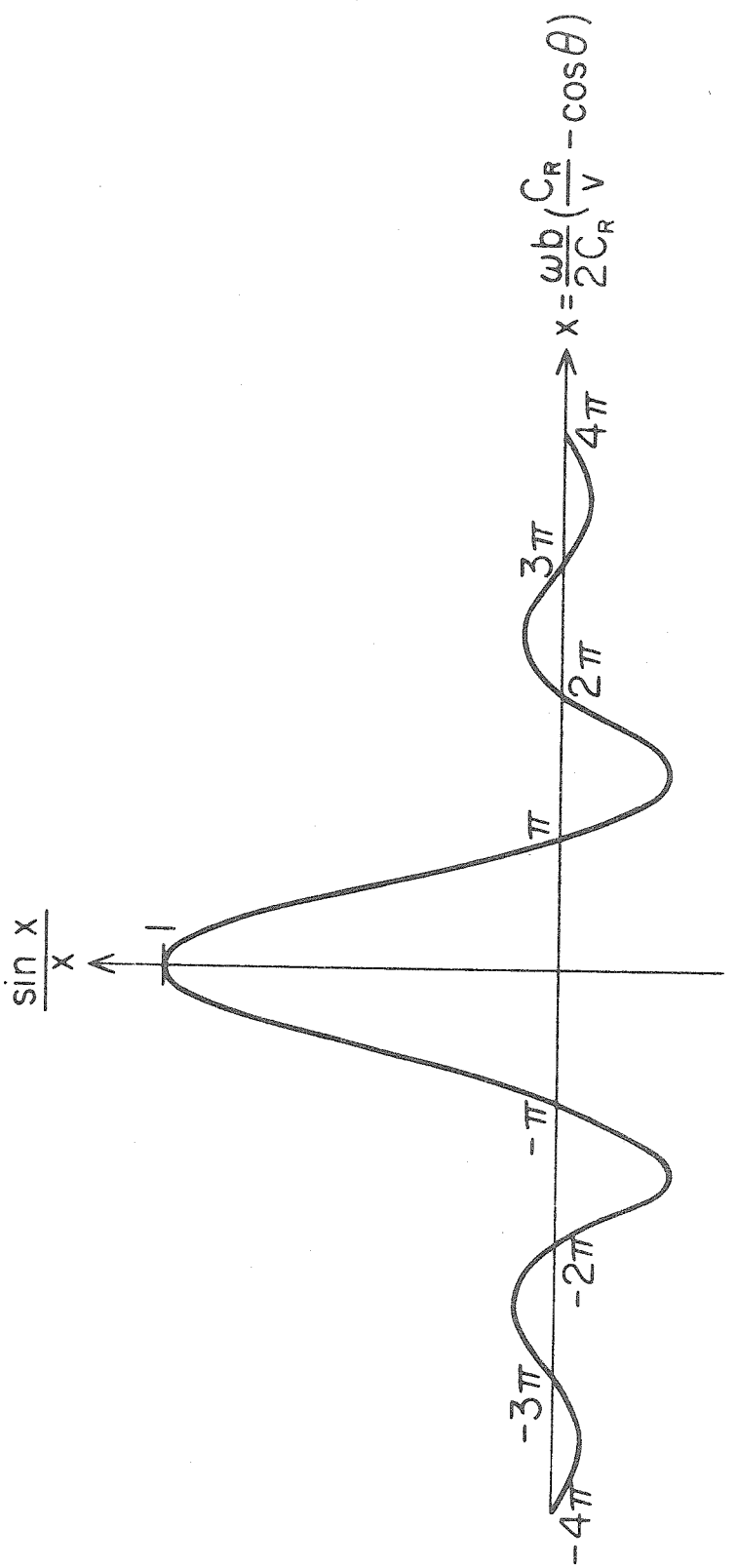
$\frac{\sin x}{x}$
1
$x = \frac{\omega b}{2C_R}\left(\frac{C_R}{V} - \cos\theta\right)$
π
2π
3π
4π
$-\pi$
-2π
-3π
-4π

Fig. 8

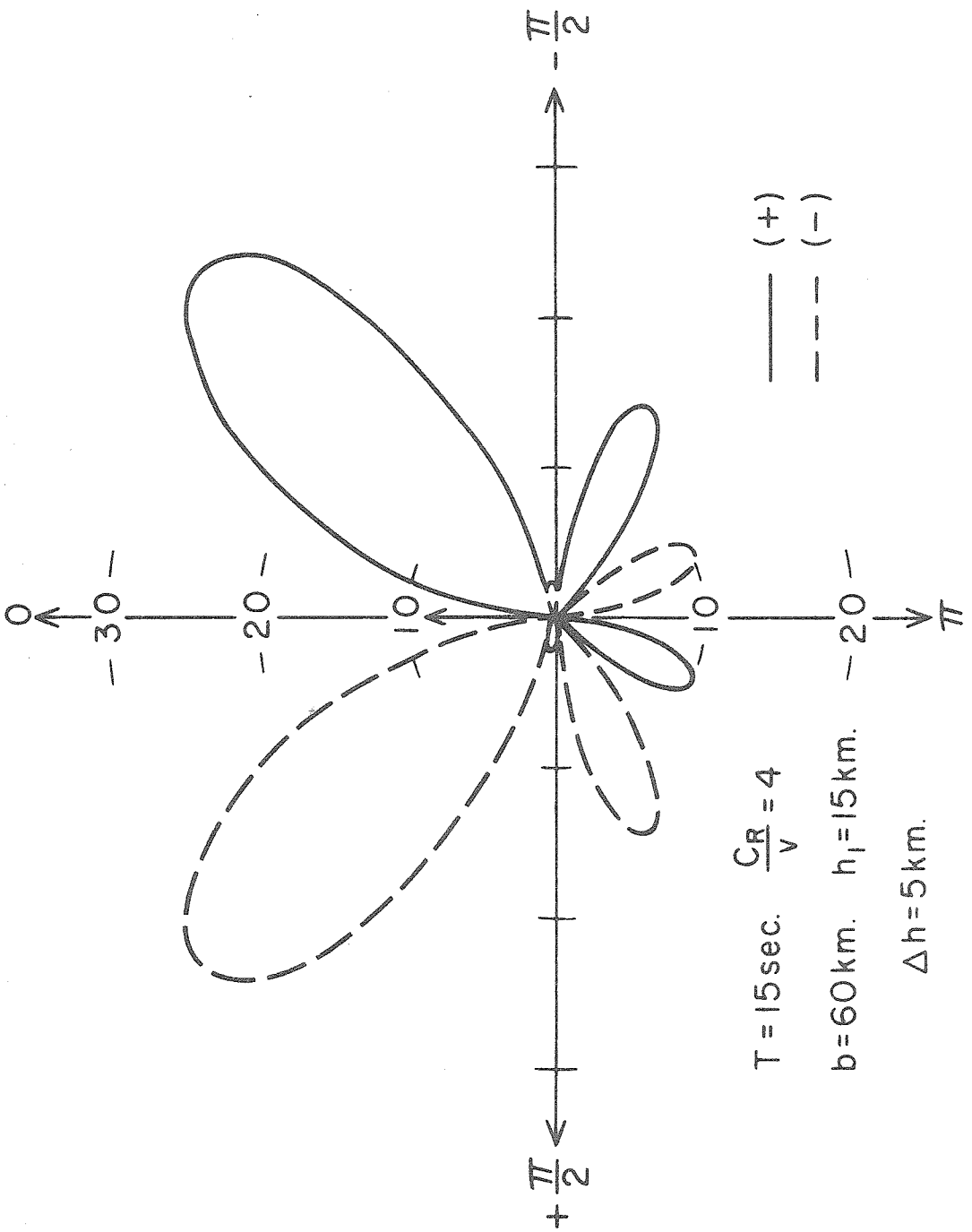

Fig. 9

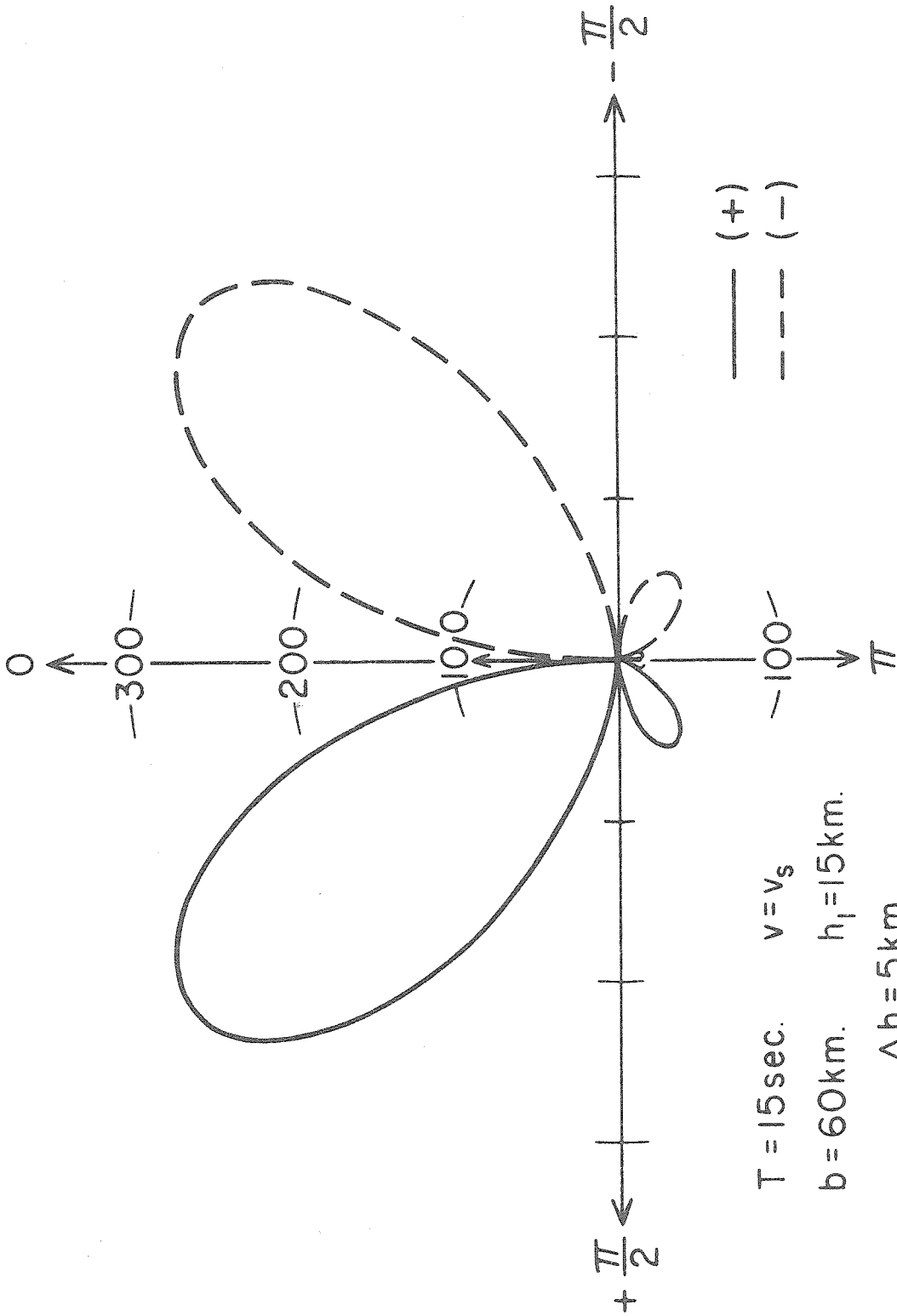

Fig. 10

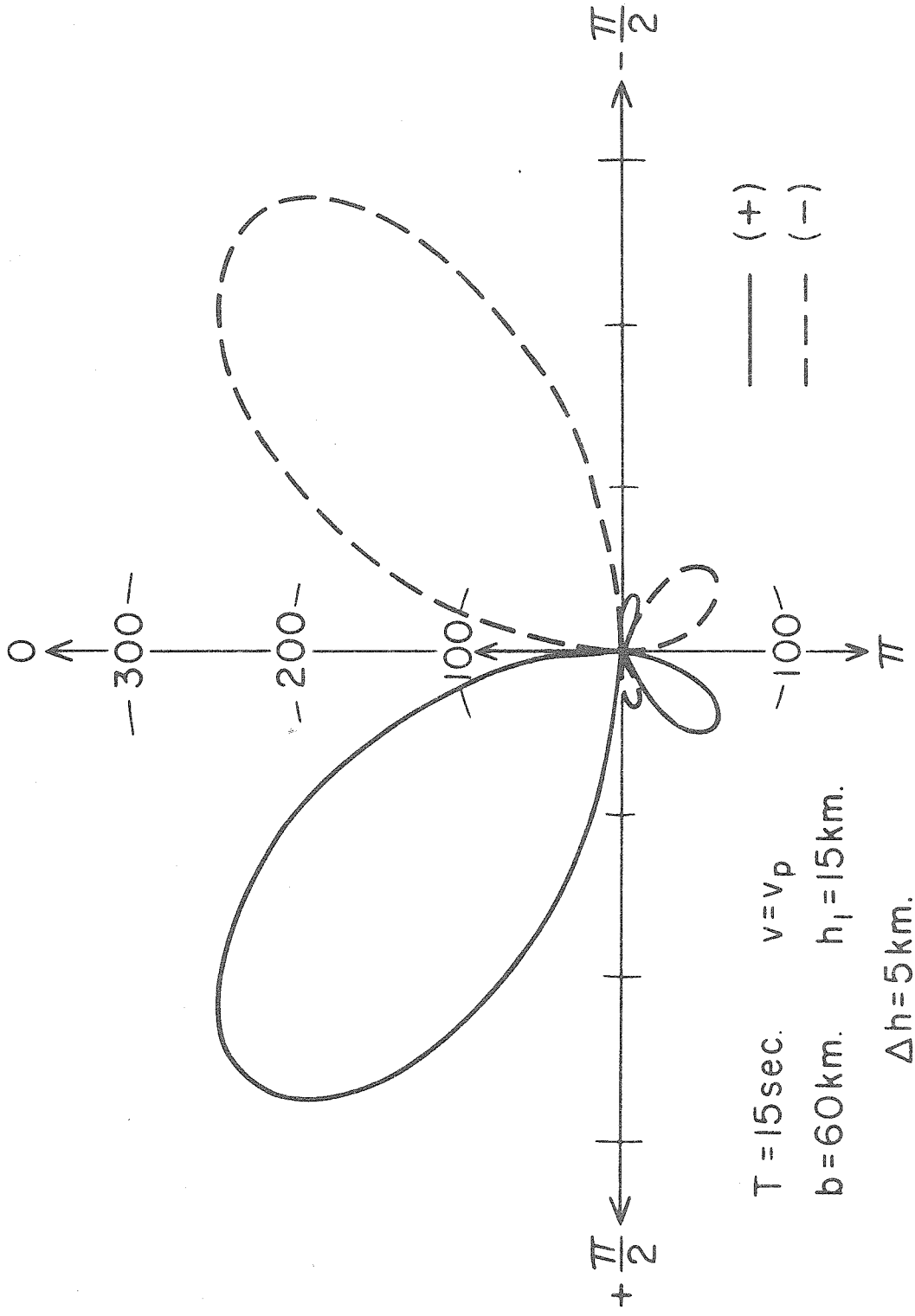

Fig. 11

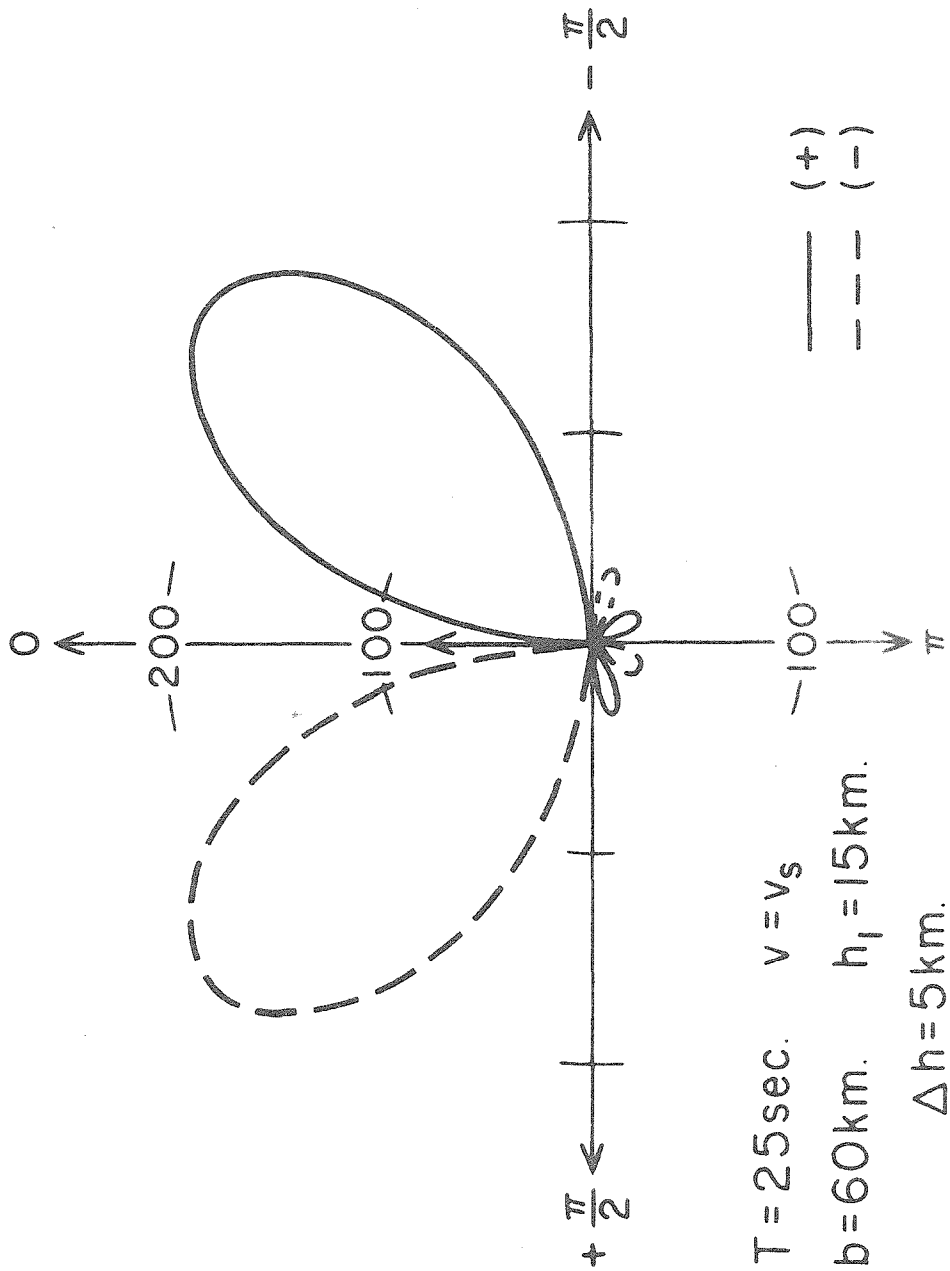

Fig. 12

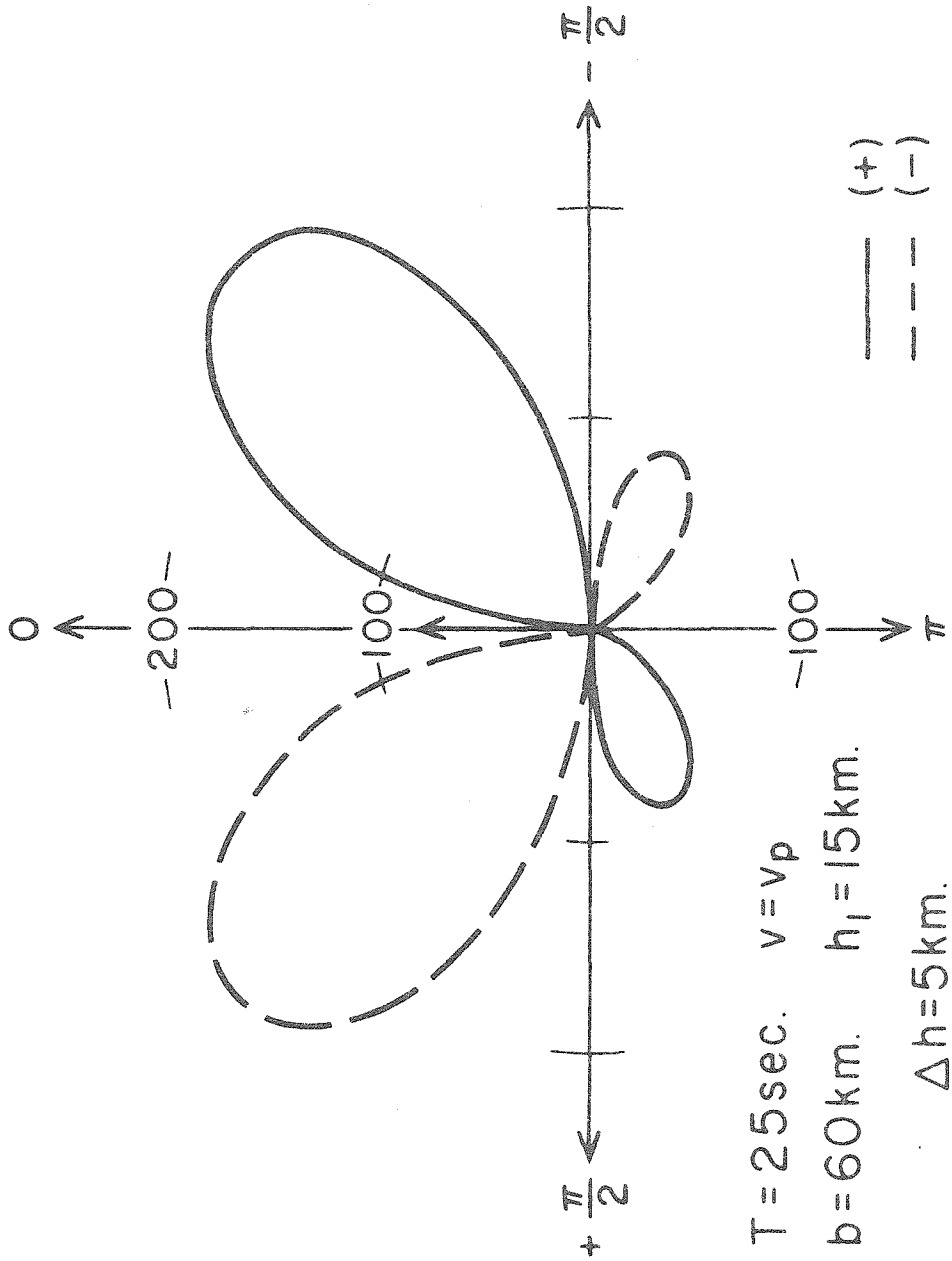

Fig. 13

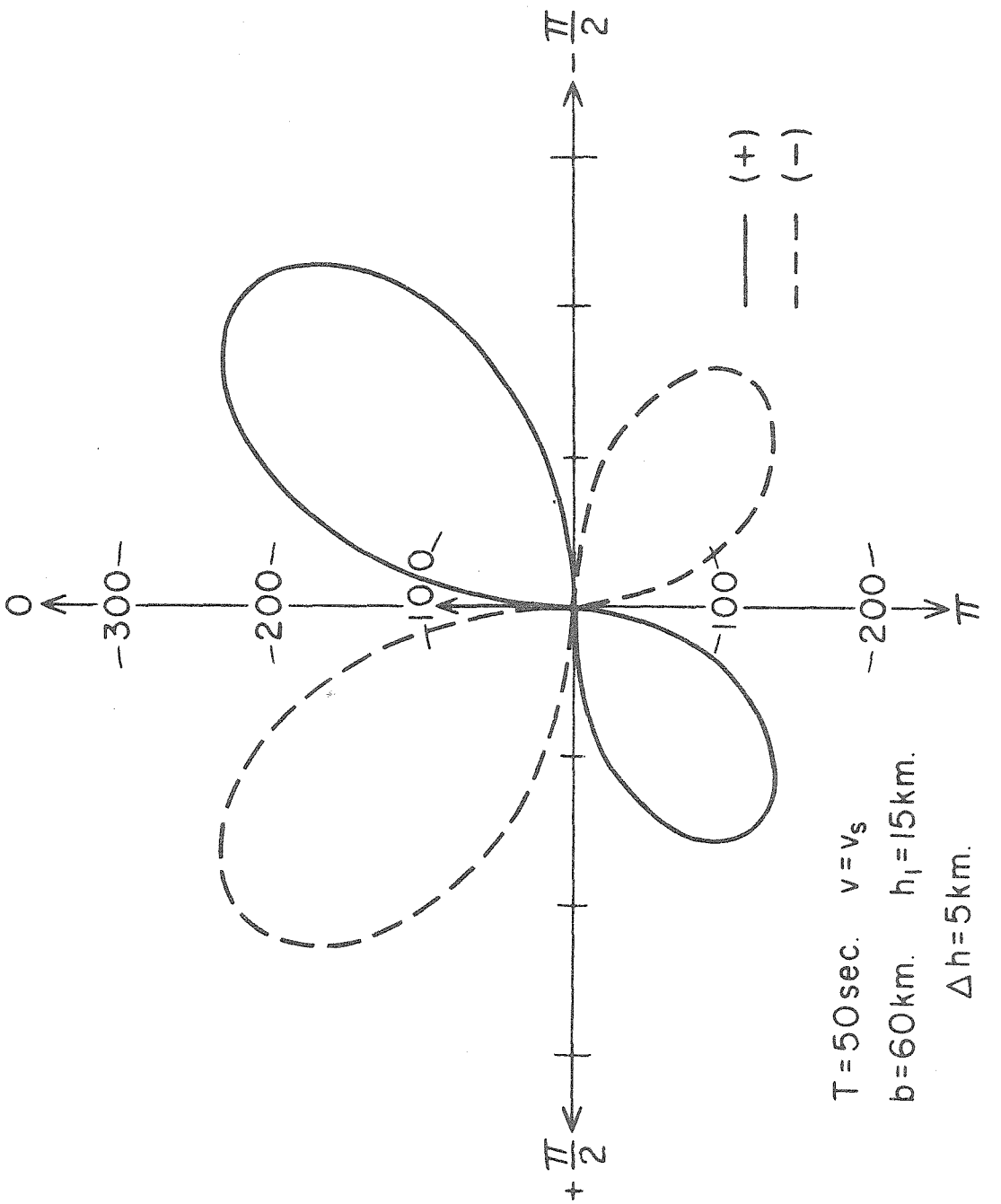

Fig. 14

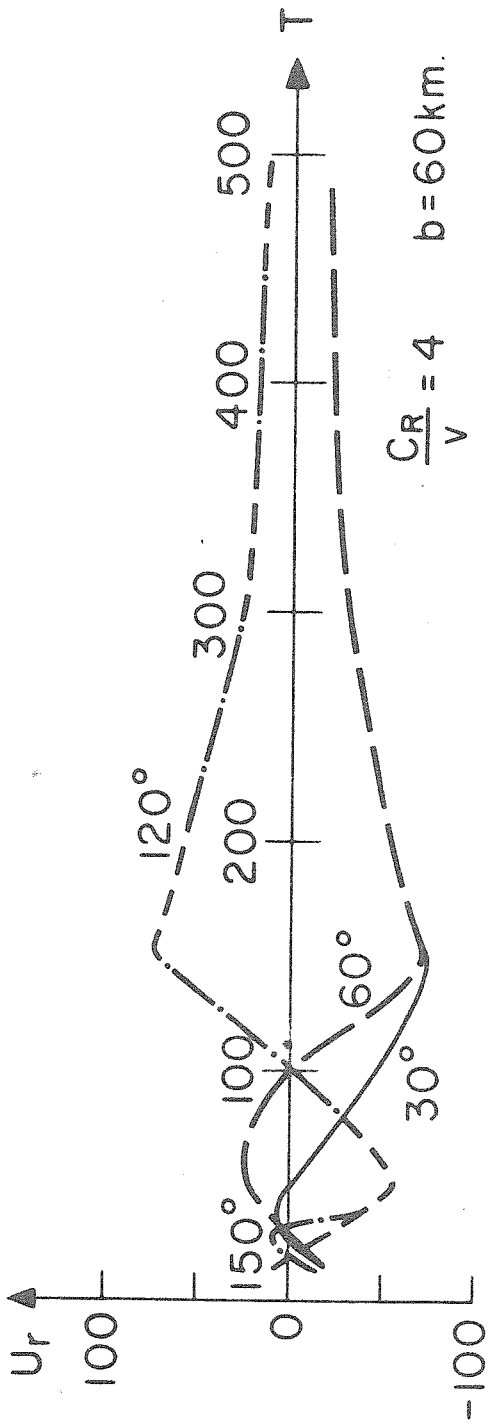
T
500
400
300
200
100
120°
60°
30°
150°
U_r
100
0
-100
$\frac{C_R}{V} = 4$ b=60km.
h_1=15km. Δh=5km.

Fig. 15

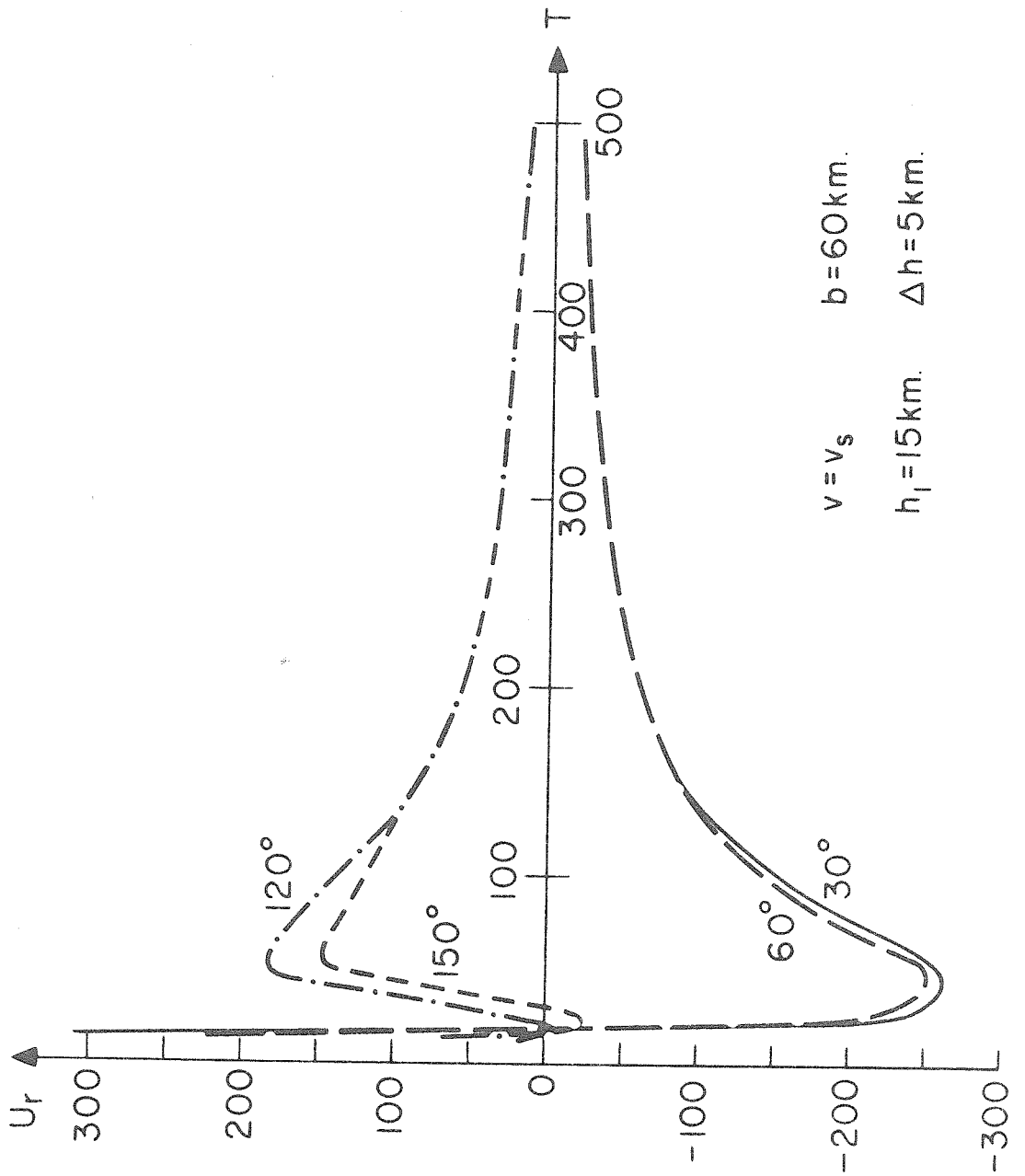
T
U_r
300
200
100
0
-100
-200
-300
100
200
300
400
500
120°
150°
60°
30°
$v = v_s$
b=60km.
h_1=15km.
Δh=5km.

Fig. 16

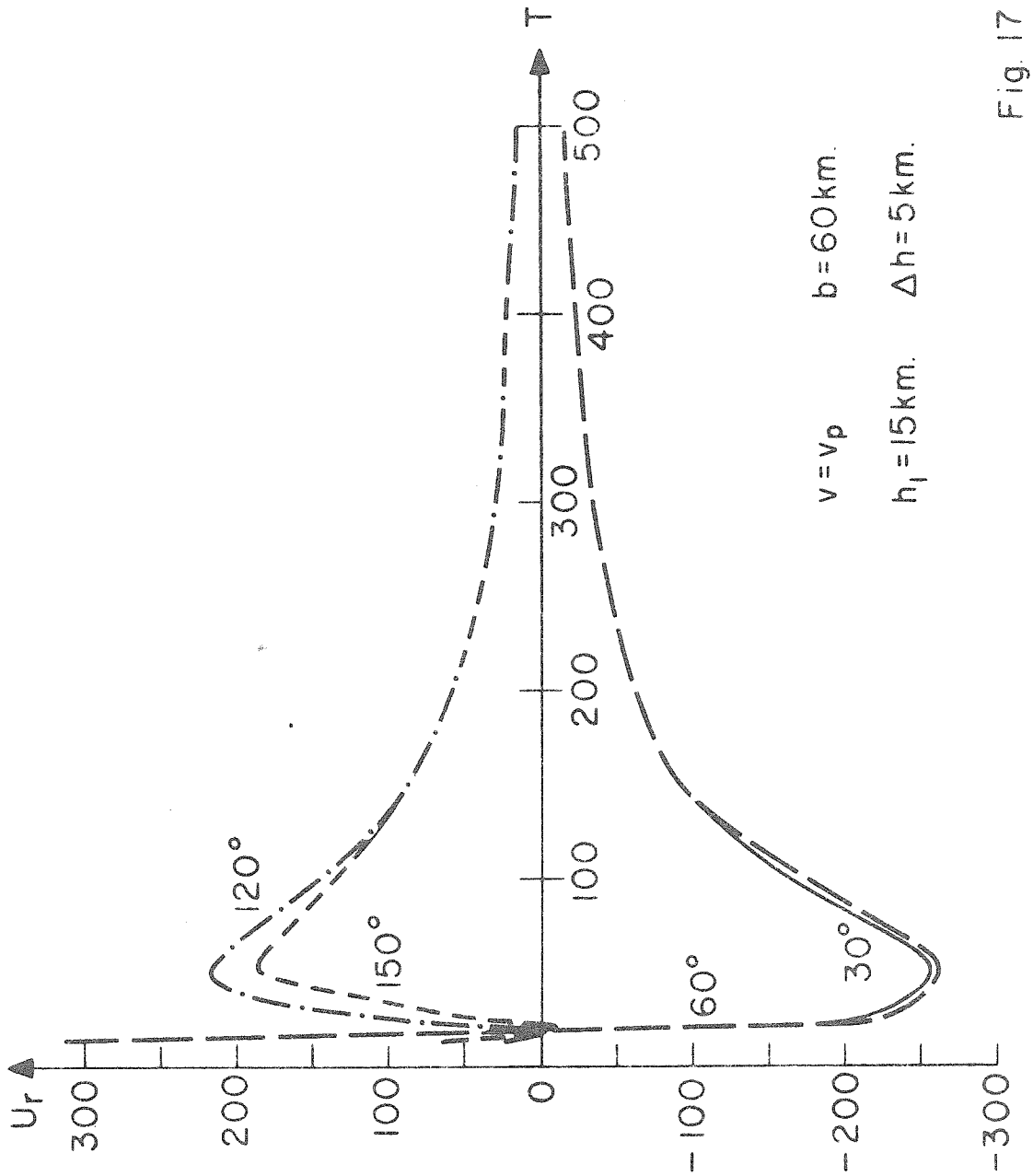
T
U_r
300
200
100
0
-100
-200
-300
100
200
300
400
500
120°
150°
60°
30°
$v = v_p$
b = 60 km.
h_1 = 15 km.
Δh = 5 km.

Fig. 17

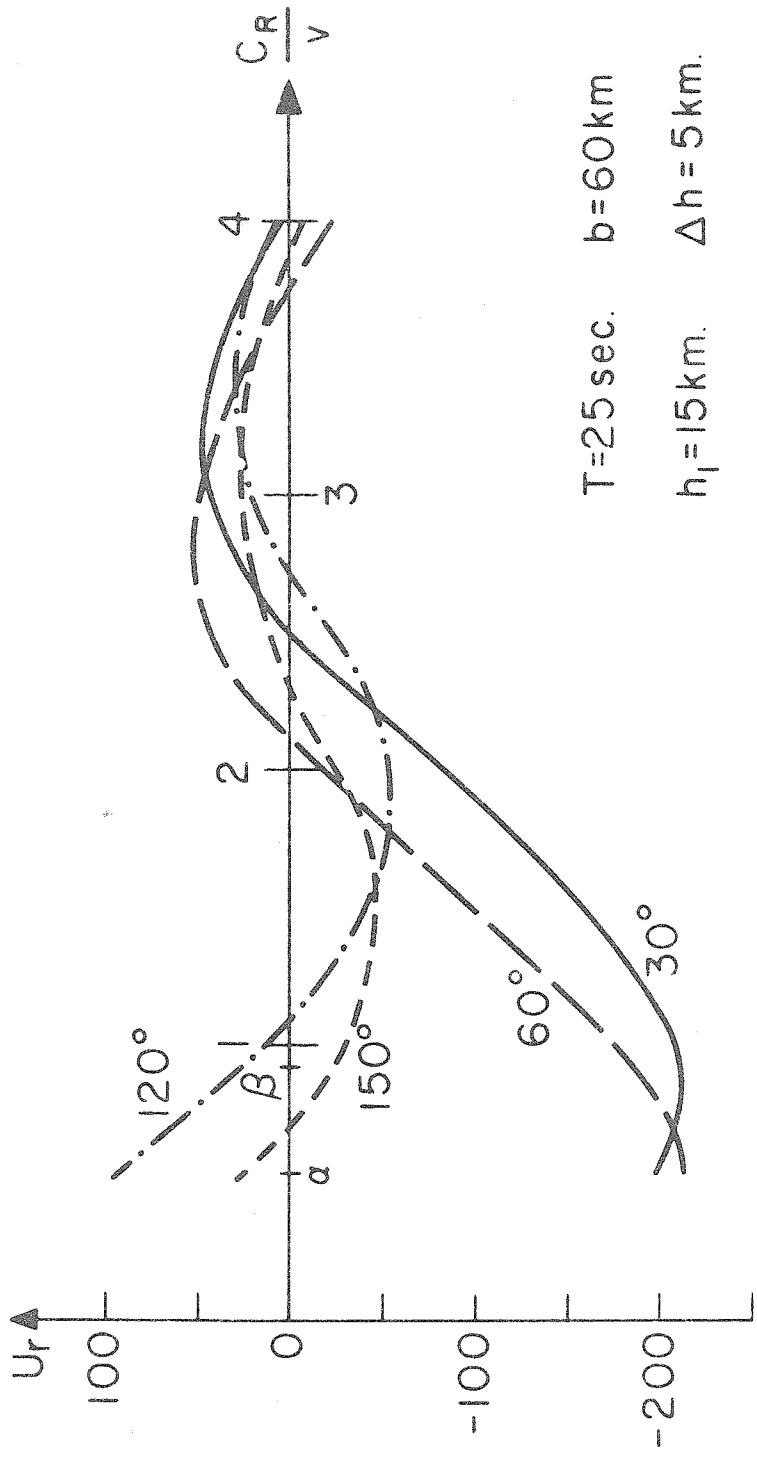
C_R/v
4
3
2
1
β
α
120°
150°
60°
30°
U_r
100
0
-100
-200
T=25 sec. b=60km
h_1=15km. Δh=5km.

Fig. 18

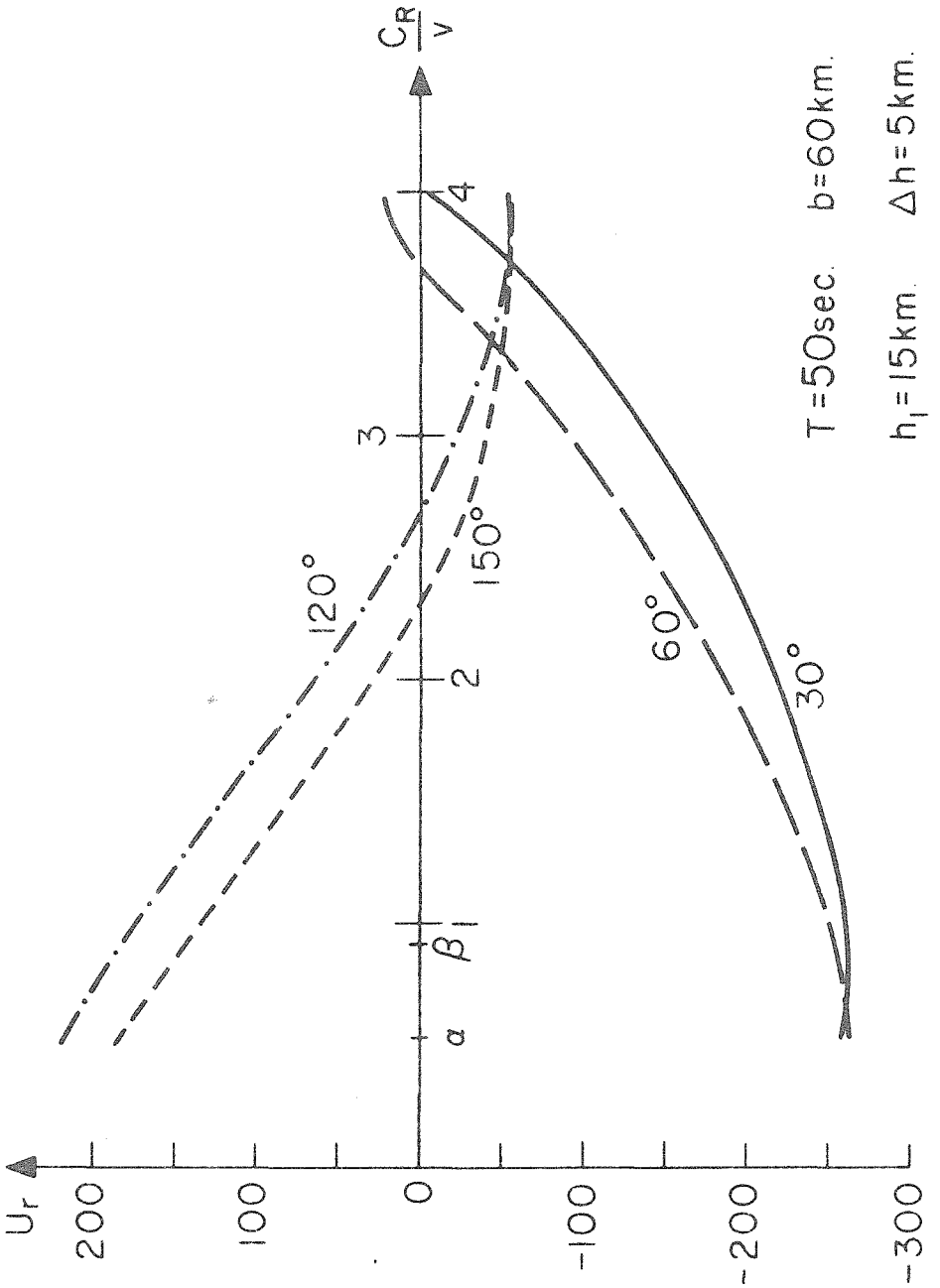
C_R/v
4
3
2
β_1
α
120°
150°
60°
30°
U_r
200
100
0
-100
-200
-300
T=50sec. b=60km.
h_1=15km. Δh=5km.

Fig. 19

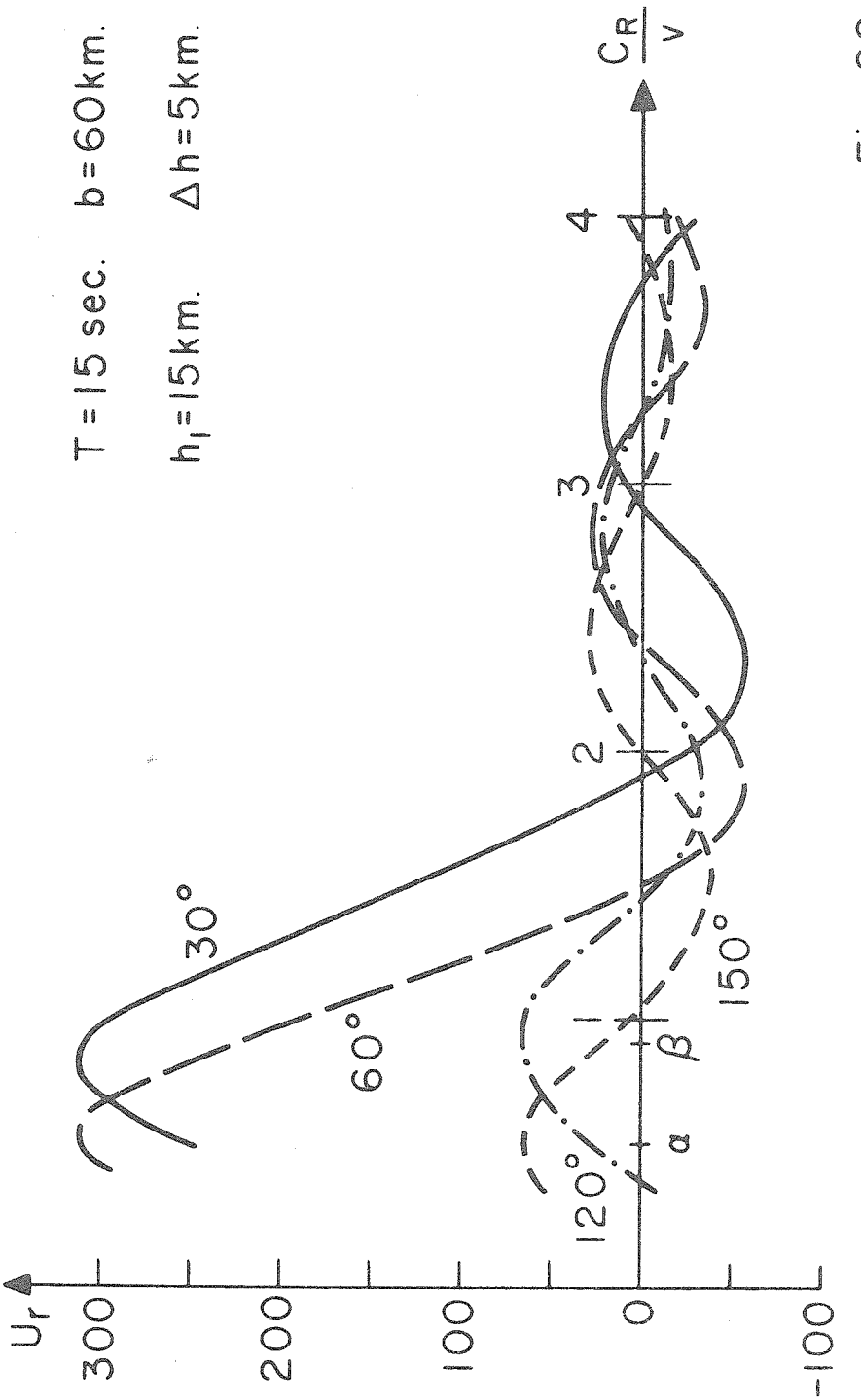
T=15 sec. b=60km.
h1=15km. Δh=5km.
Ur
300
200
100
0
-100
CR/v
4
3
2
1
α
β
30°
60°
120°
150°

Fig. 20

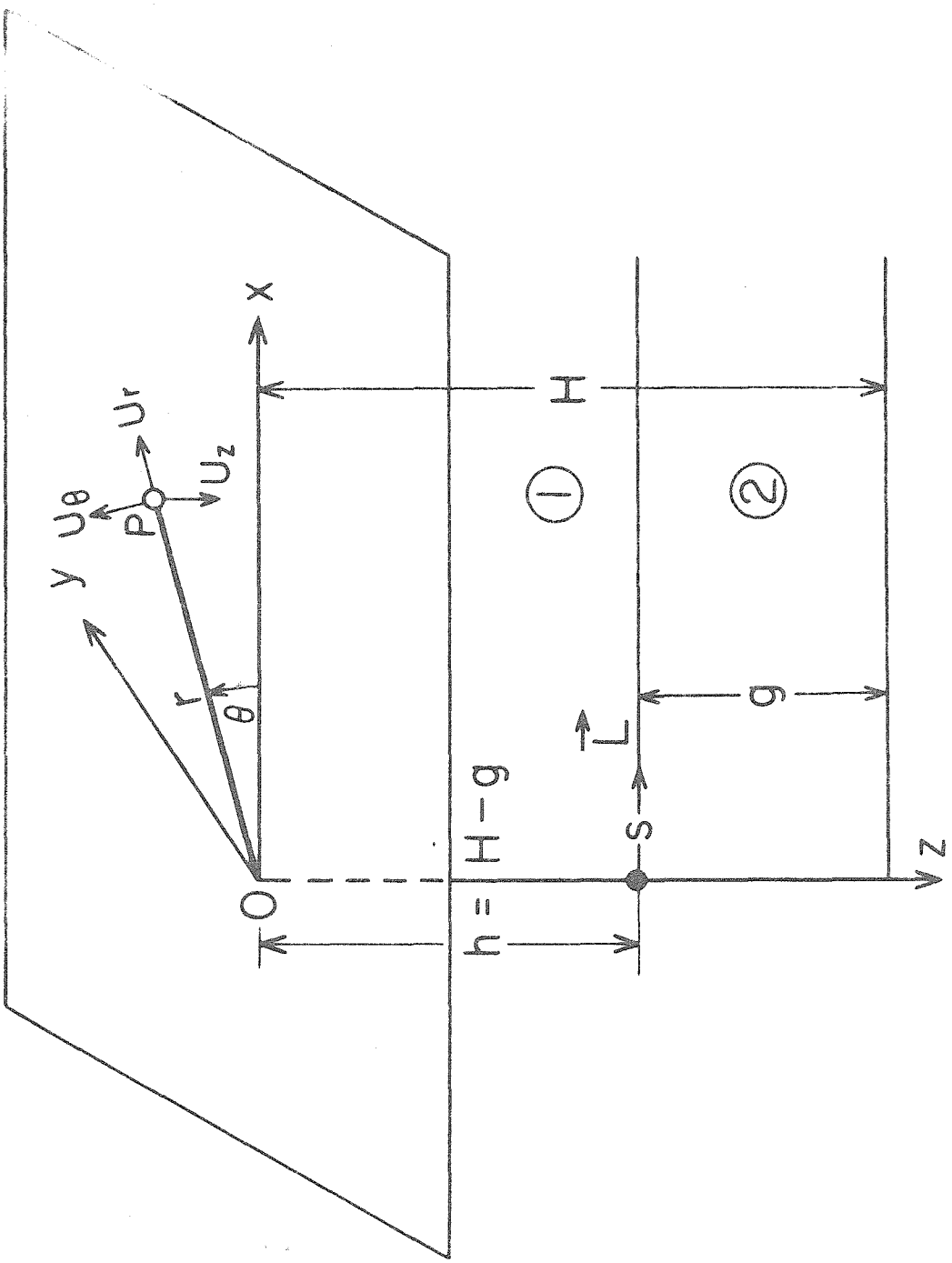

Fig. 21

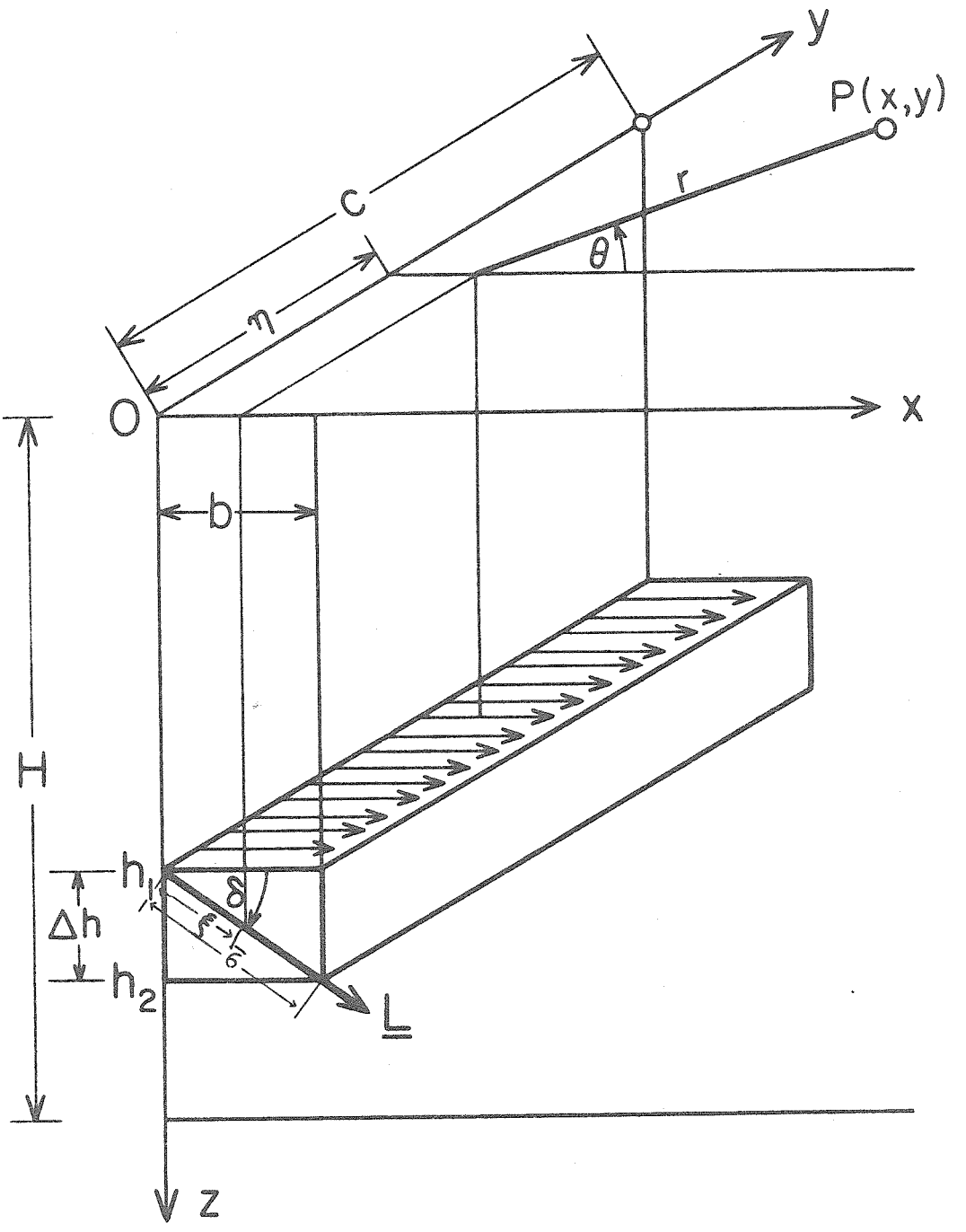

Fig. 22

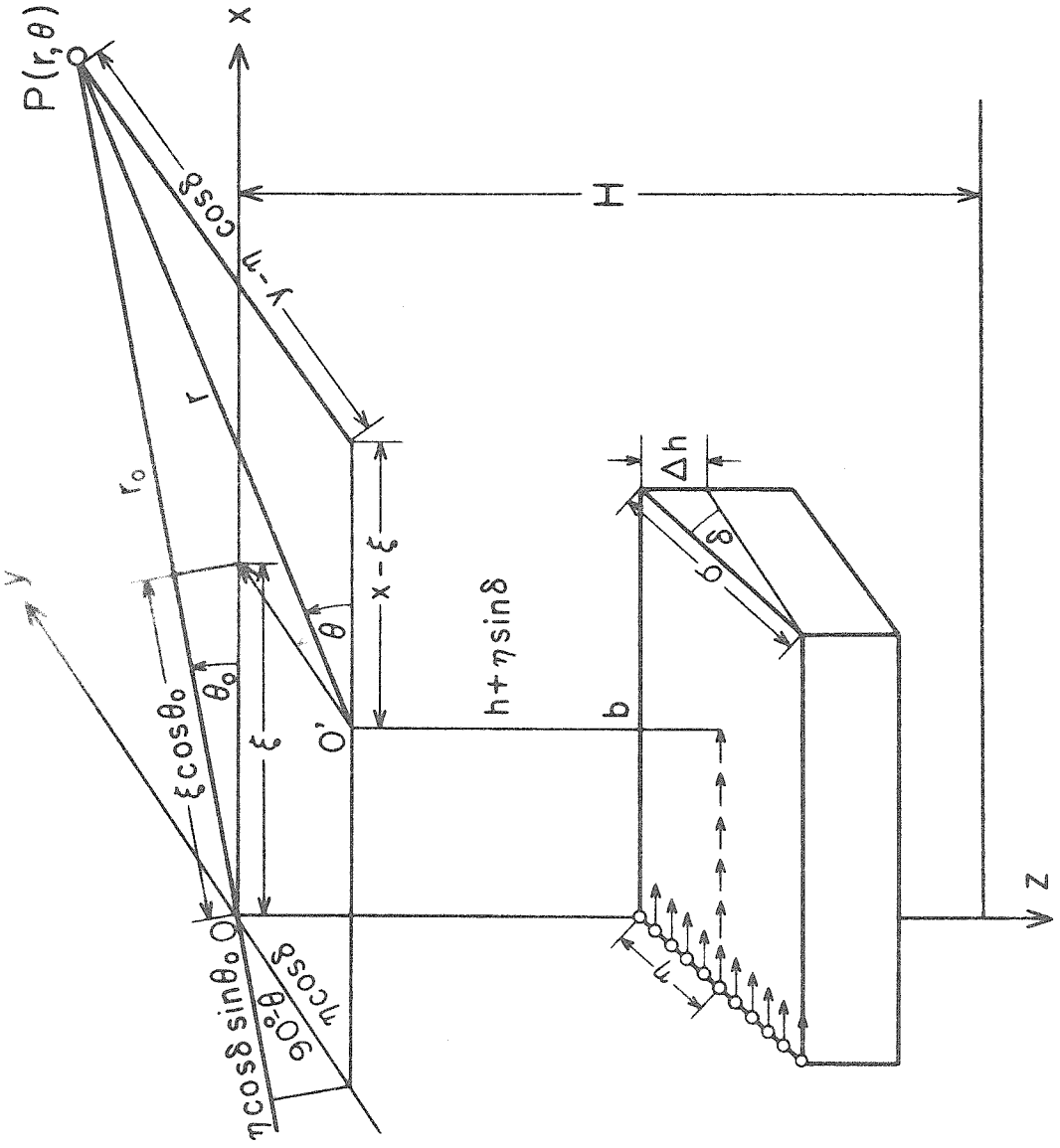
P(r, θ)
x
H
y-η cosδ
r
r₀
ξ-x
θ
θ₀
ξ cosθ₀
ξ
O'
h+η sinδ
b
Δh
δ
δ
η
y
O
η cosδ
90°-θ₀
η cosδ sinθ₀
z

Fig. 23

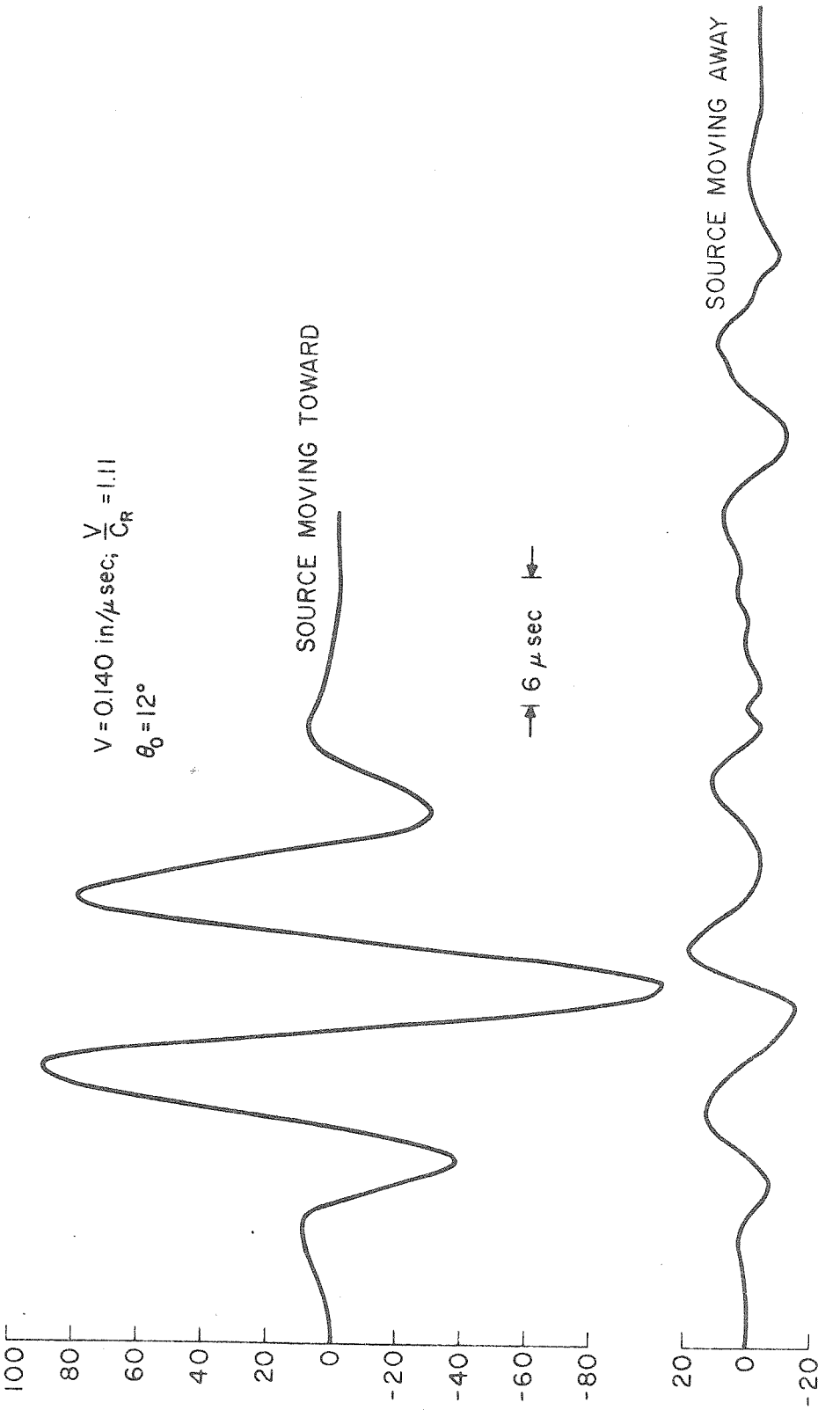
V = 0.140 in/μ sec; V/C_R = 1.11
θ_0 = 12°
SOURCE MOVING TOWARD
6 μ sec
SOURCE MOVING AWAY
100
80
60
40
20
0
-20
-40
-60
-80
20
0
-20

Fig. 24

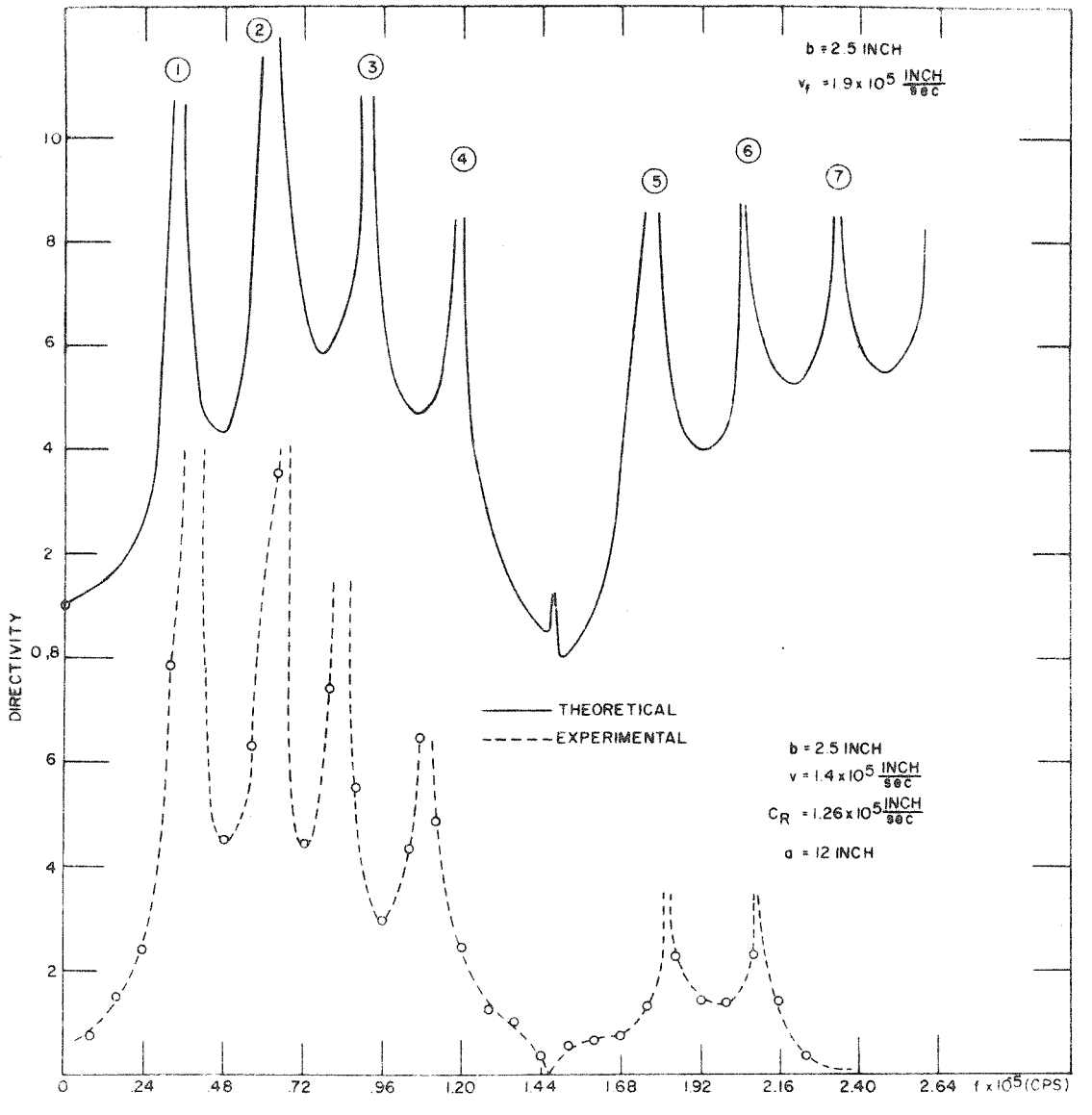
b = 2.5 INCH
v_f = 1.9 x 10^5 INCH/sec
DIRECTIVITY
10
8
6
4
2
0.8
6
4
2
THEORETICAL
EXPERIMENTAL
b = 2.5 INCH
v = 1.4 x 10^5 INCH/sec
C_R = 1.26 x 10^5 INCH/sec
a = 12 INCH
1
2
3
4
5
6
7
0
.24
.48
.72
.96
1.20
1.44
1.68
1.92
2.16
2.40
2.64
f x 10^5 (CPS)

Fig. 25

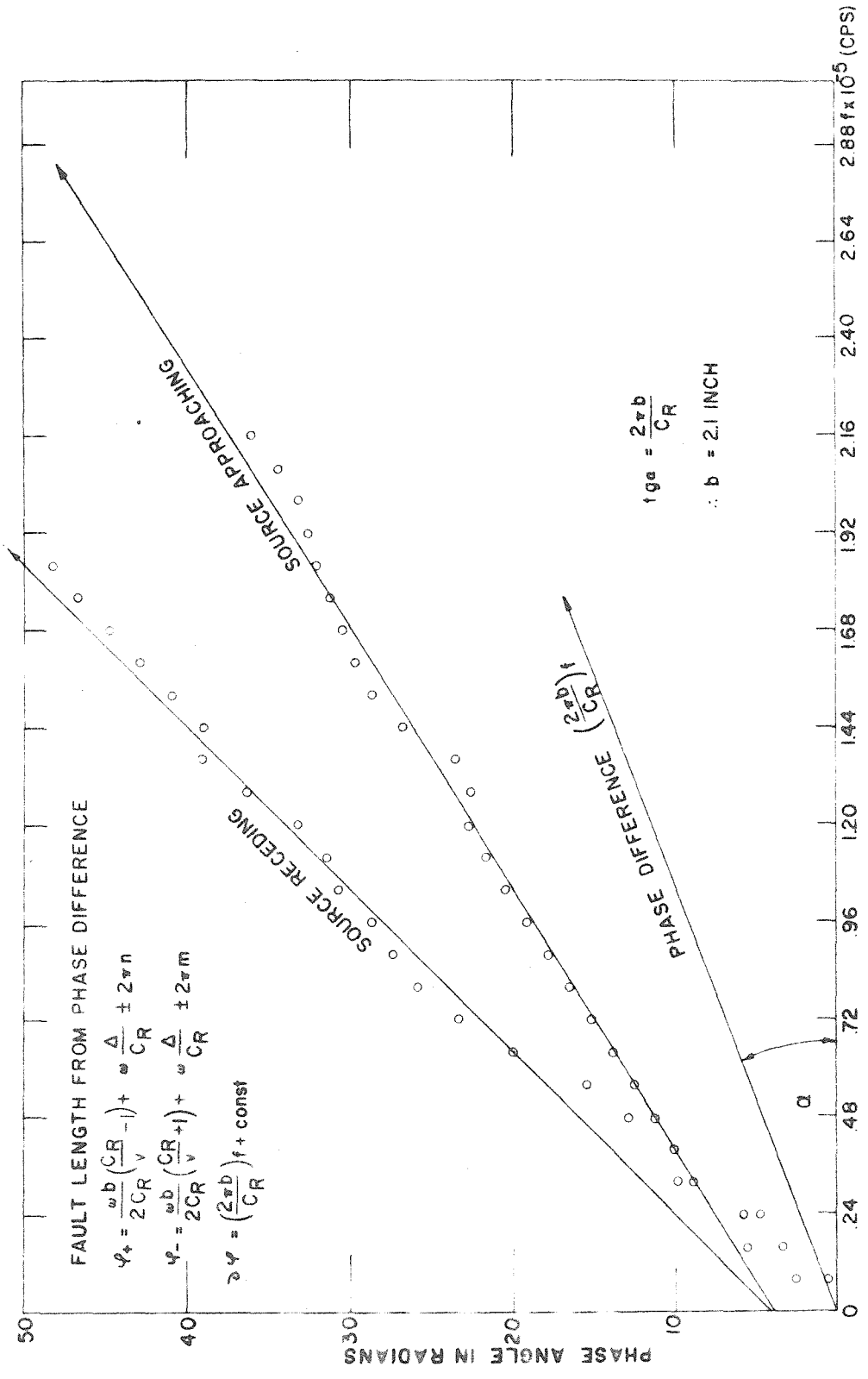
FAULT LENGTH FROM PHASE DIFFERENCE
$\varphi_+ = \frac{\omega b}{2C_R}\left(\frac{C_R}{v}-1\right) + \omega\frac{\Delta}{C_R} \pm 2\pi n$
$\varphi_- = \frac{\omega b}{2C_R}\left(\frac{C_R}{v}+1\right) + \omega\frac{\Delta}{C_R} \pm 2\pi m$
$\Delta\varphi = \left(\frac{2\pi b}{C_R}\right)f + \text{const}$
SOURCE APPROACHING
SOURCE RECEDING
PHASE DIFFERENCE $\left(\frac{2\pi b}{C_R}\right)f$
$\tan\alpha = \frac{2\pi b}{C_R}$
$\therefore b = 2.1$ INCH
PHASE ANGLE IN RADIANS
0
10
20
30
40
50
.24
.48
.72
.96
1.20
1.44
1.68
1.92
2.16
2.40
2.64
2.88 f x 10^5 (CPS)

Fig 26

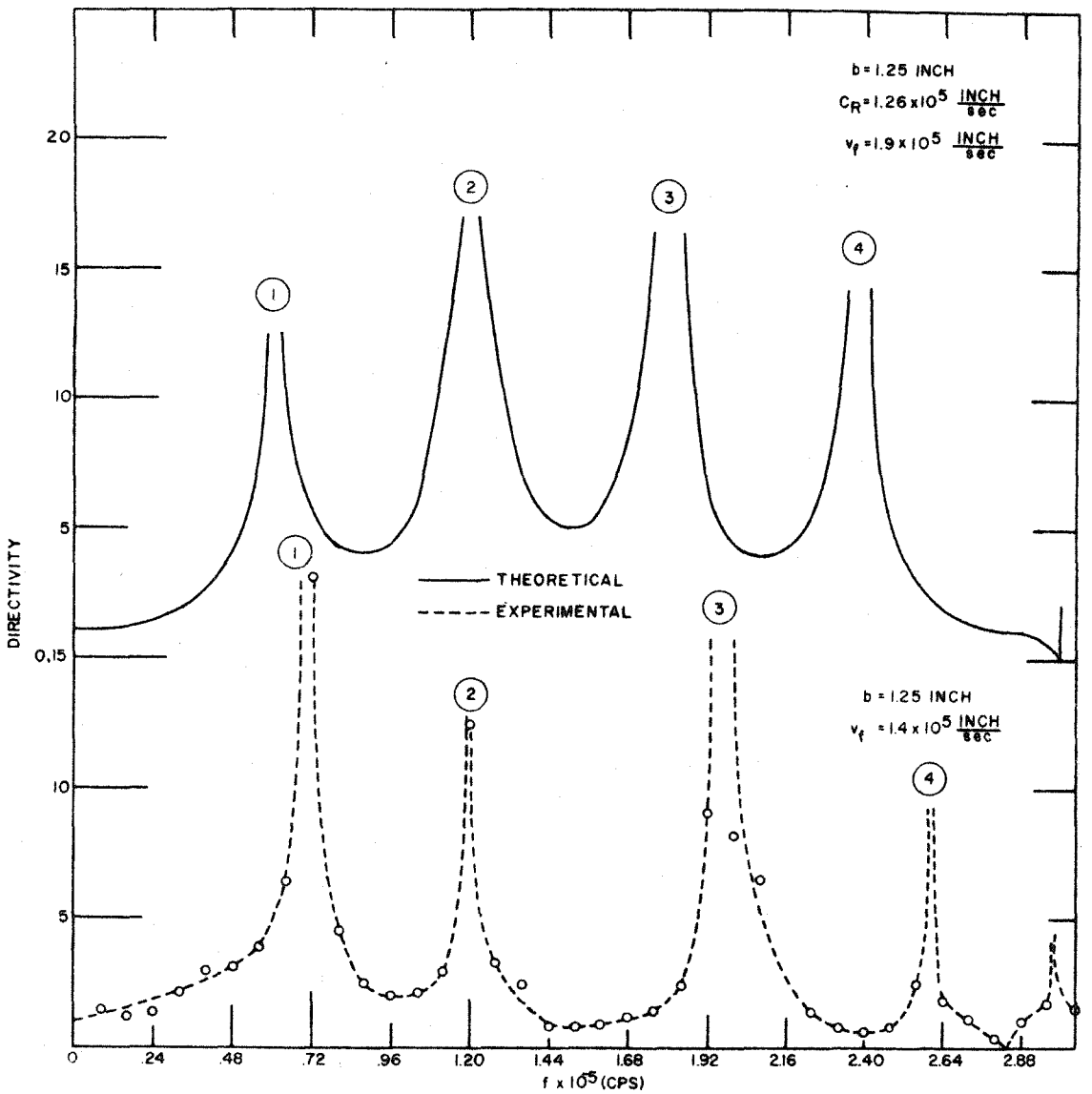
b = 1.25 INCH
$C_R = 1.26 \times 10^5 \frac{INCH}{sec}$
$v_f = 1.9 \times 10^5 \frac{INCH}{sec}$
THEORETICAL
EXPERIMENTAL
b = 1.25 INCH
$v_f = 1.4 \times 10^5 \frac{INCH}{sec}$
DIRECTIVITY
20
15
10
5
0.15
10
5
0
.24
.48
.72
.96
1.20
1.44
1.68
1.92
2.16
2.40
2.64
2.88
f x 10^5 (CPS)

Fig. 27

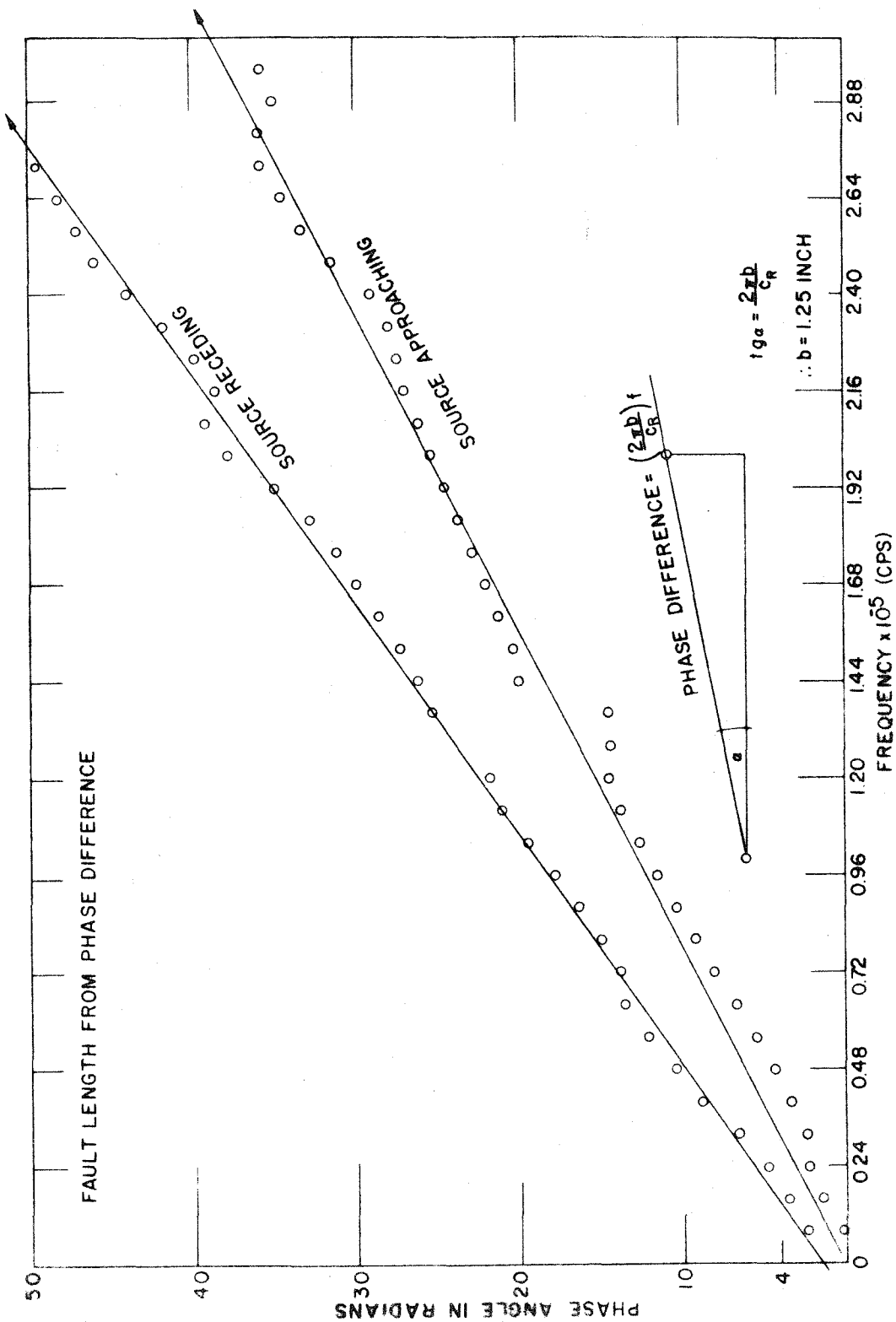
FAULT LENGTH FROM PHASE DIFFERENCE
SOURCE RECEDING
SOURCE APPROACHING
PHASE DIFFERENCE = $\left(\frac{2\pi b}{c_R}\right) f$
$tg\alpha = \frac{2\pi b}{c_R}$
$\therefore b = 1.25$ INCH
PHASE ANGLE IN RADIANS
FREQUENCY $\times 10^5$ (CPS)
50
40
30
20
10
4
0
0.24
0.48
0.72
0.96
1.20
1.44
1.68
1.92
2.16
2.40
2.64
2.88

Fig. 28

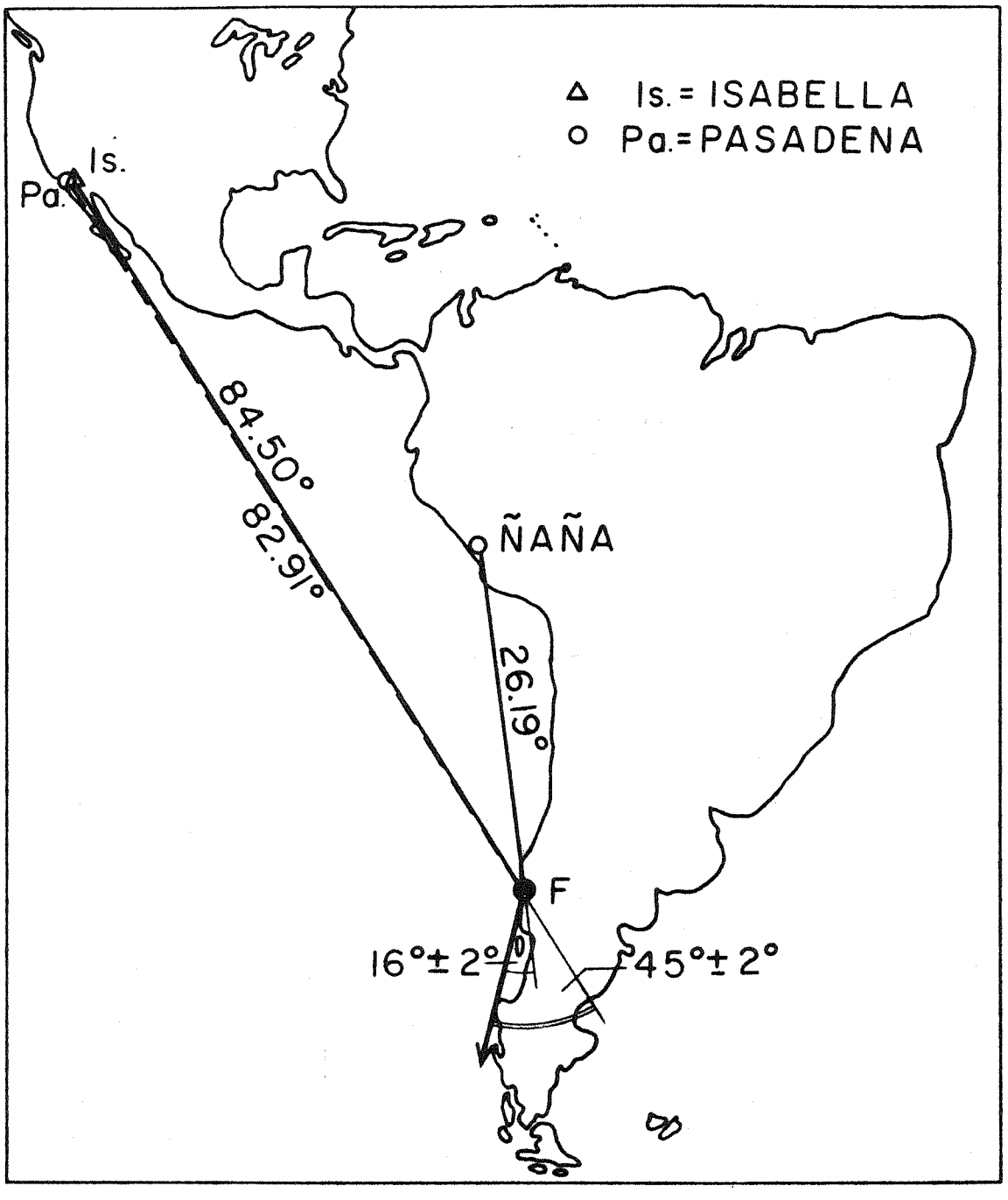

Fig. 29

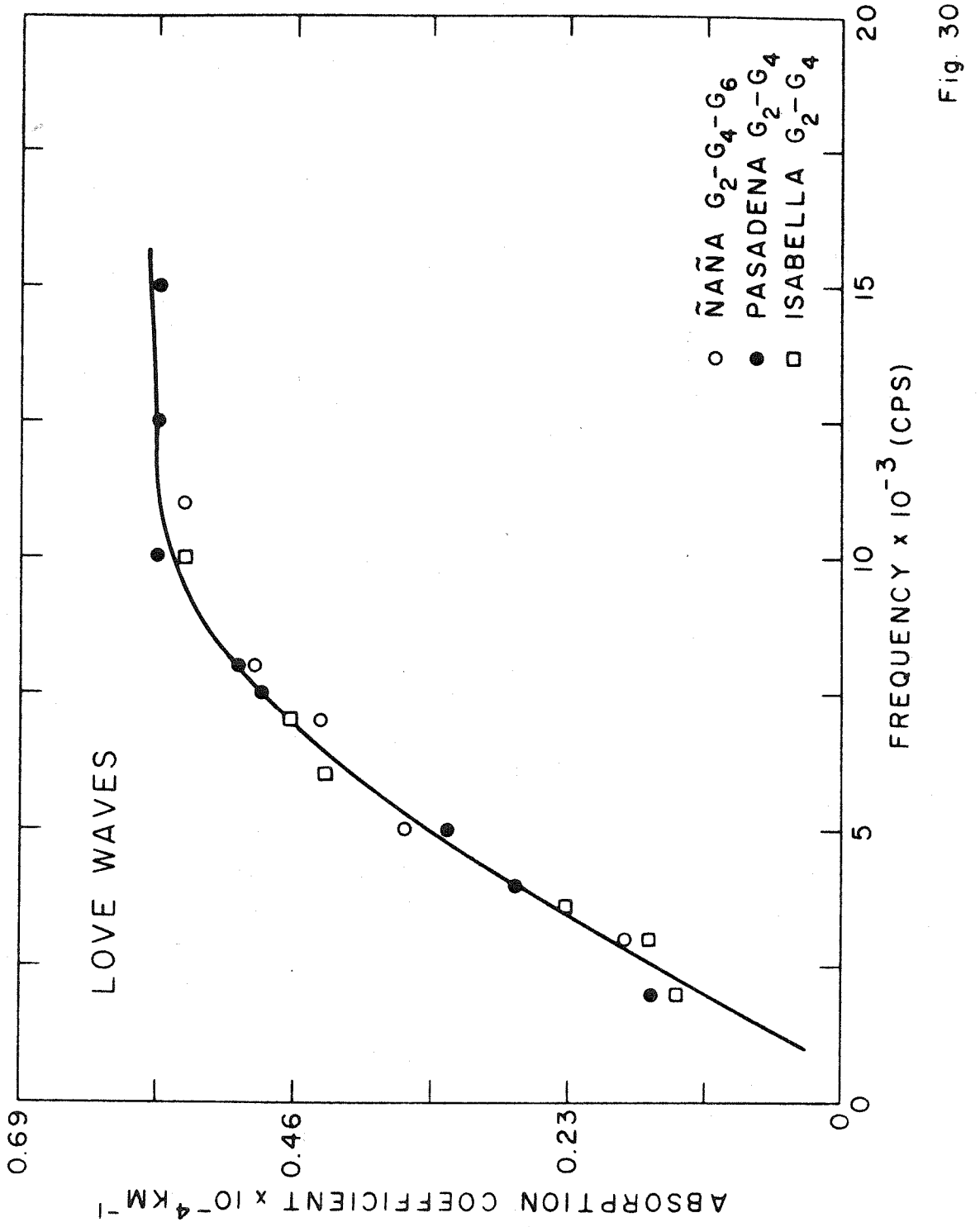
LOVE WAVES
ÑAÑA $G_2-G_4-G_6$
PASADENA G_2-G_4
ISABELLA G_2-G_4
ABSORPTION COEFFICIENT x 10^{-4} KM^{-1}
0.69
0.46
0.23
0
0
5
10
15
20
FREQUENCY x 10^{-3} (CPS)

Fig. 30

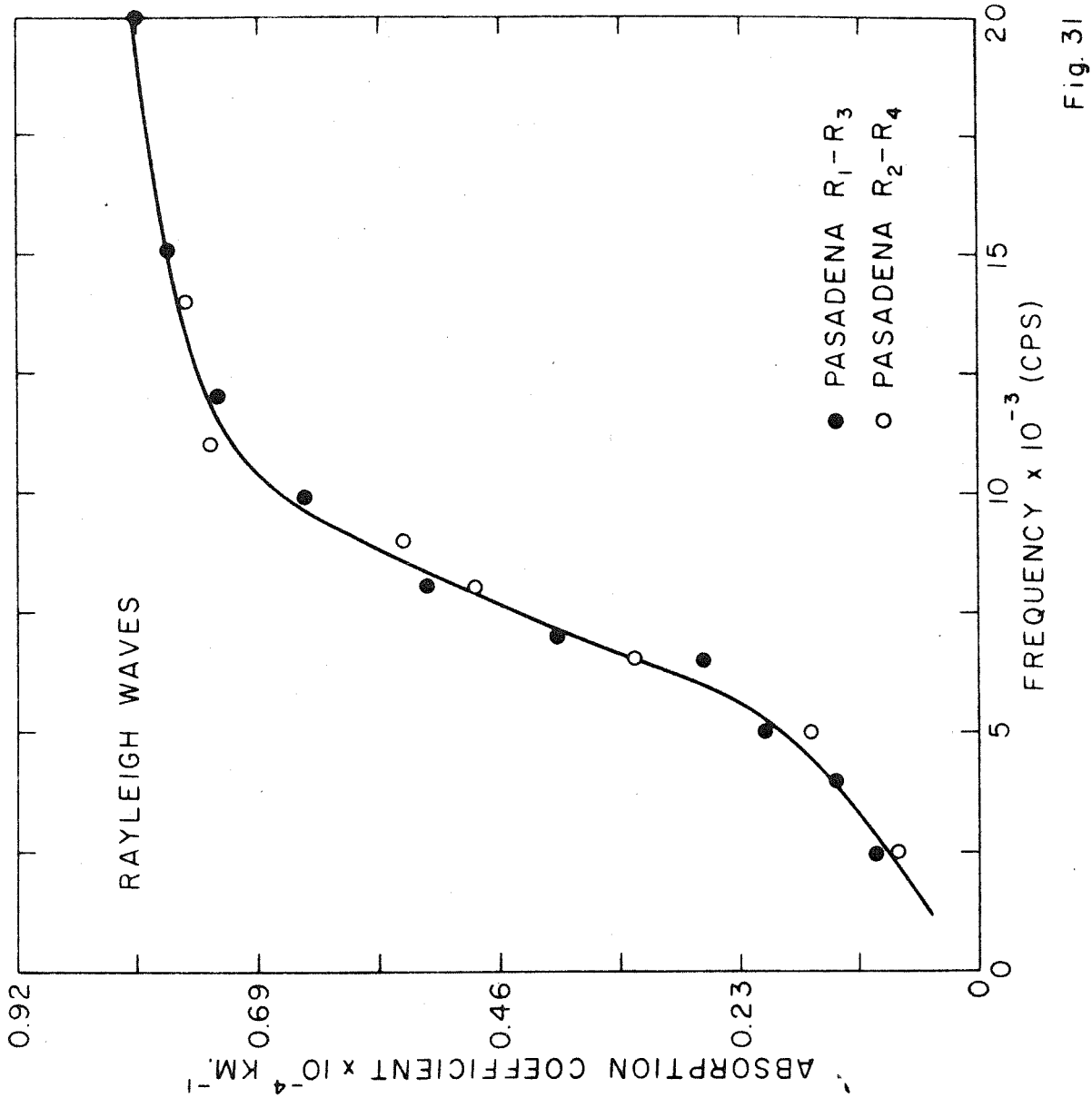
RAYLEIGH WAVES
PASADENA R_1-R_3
PASADENA R_2-R_4
ABSORPTION COEFFICIENT x 10^{-4} KM.$^{-1}$
0.92
0.69
0.46
0.23
0
0
5
10
15
20
FREQUENCY x 10^{-3} (CPS)

Fig. 31

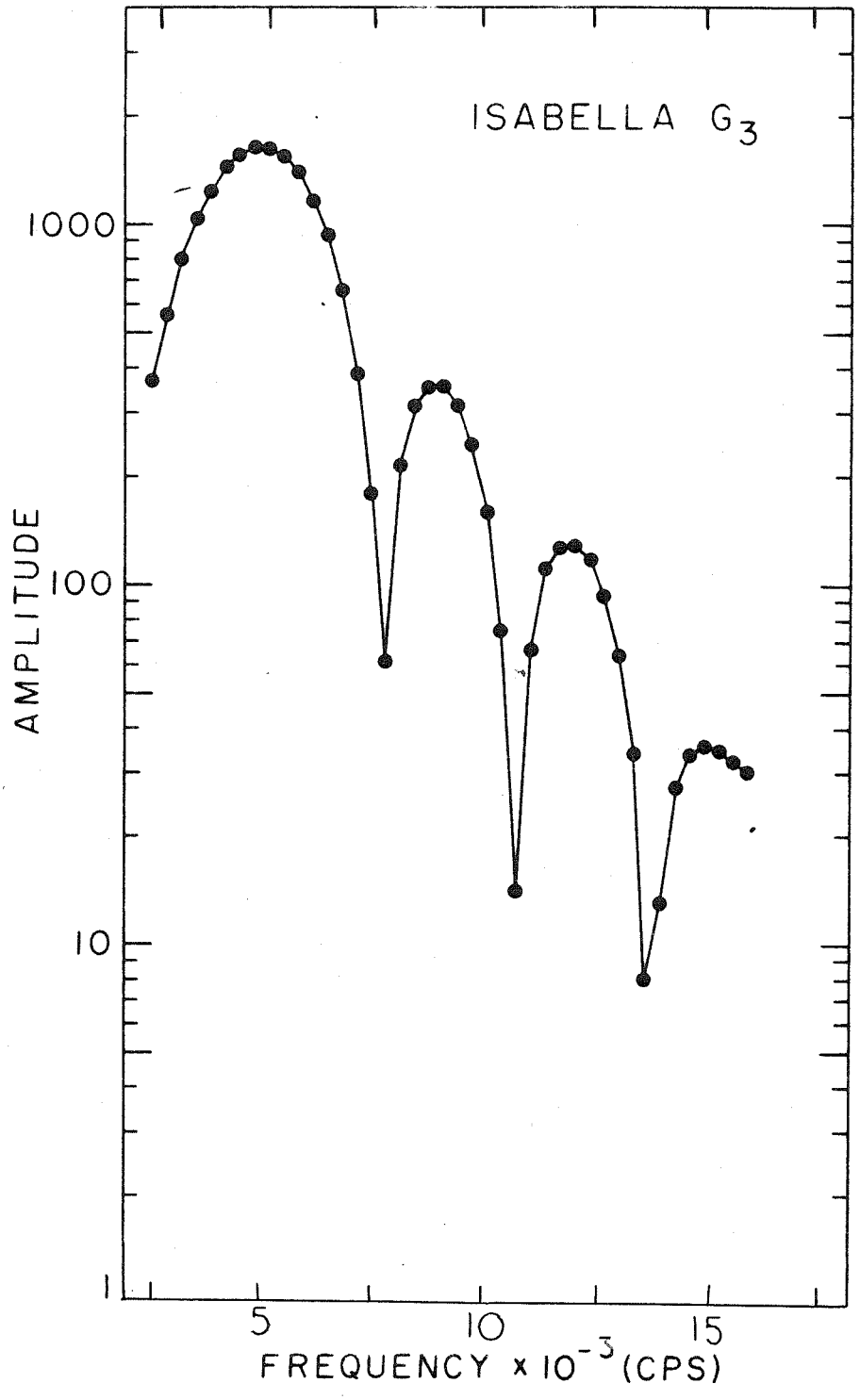
ISABELLA G_3
1000
100
10
1
AMPLITUDE
5
10
15
FREQUENCY x 10^{-3} (CPS)

Fig. 32

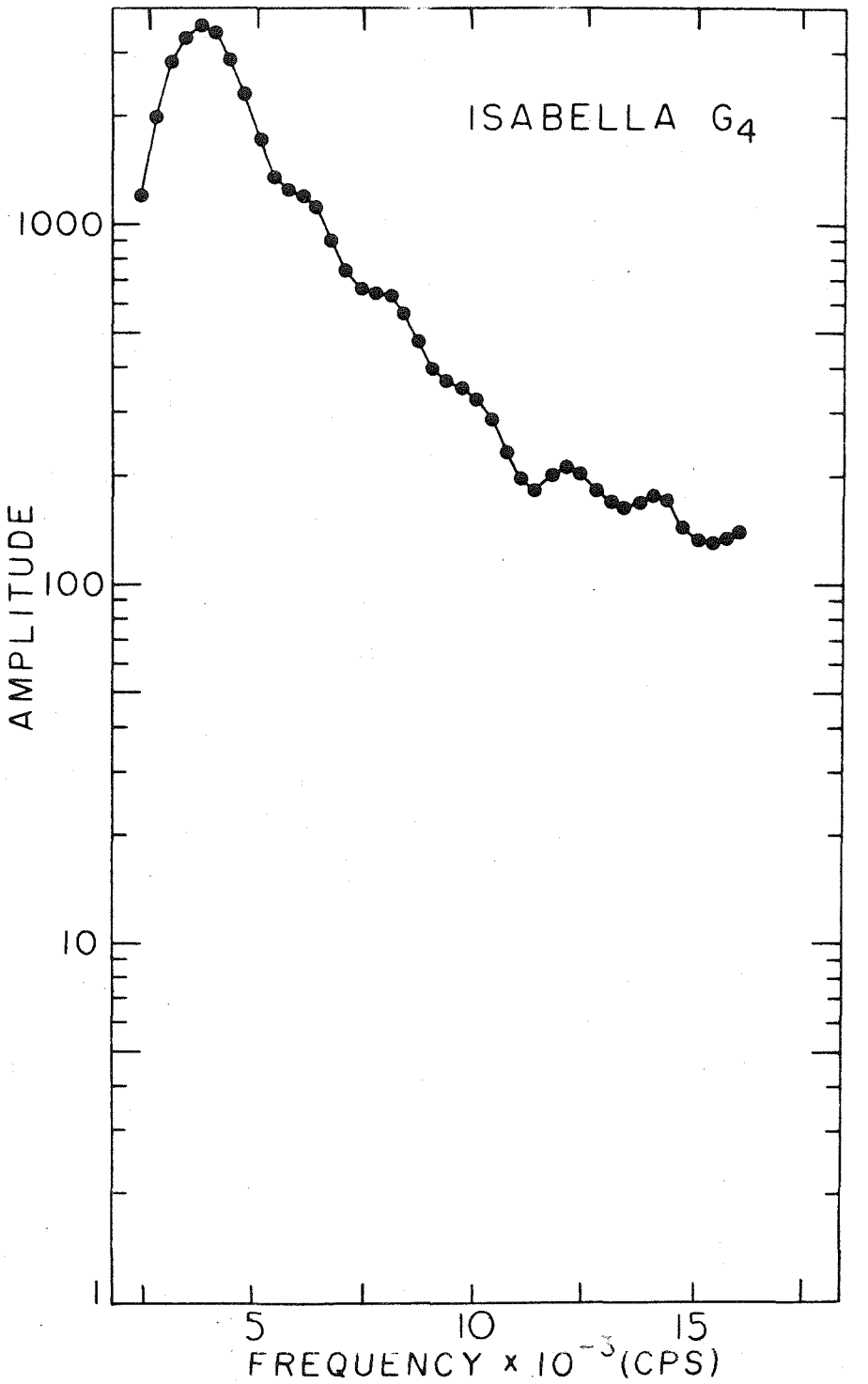
ISABELLA G_4
1000
100
10
1
AMPLITUDE
5
10
15
FREQUENCY x 10^{-3} (CPS)

Fig. 33

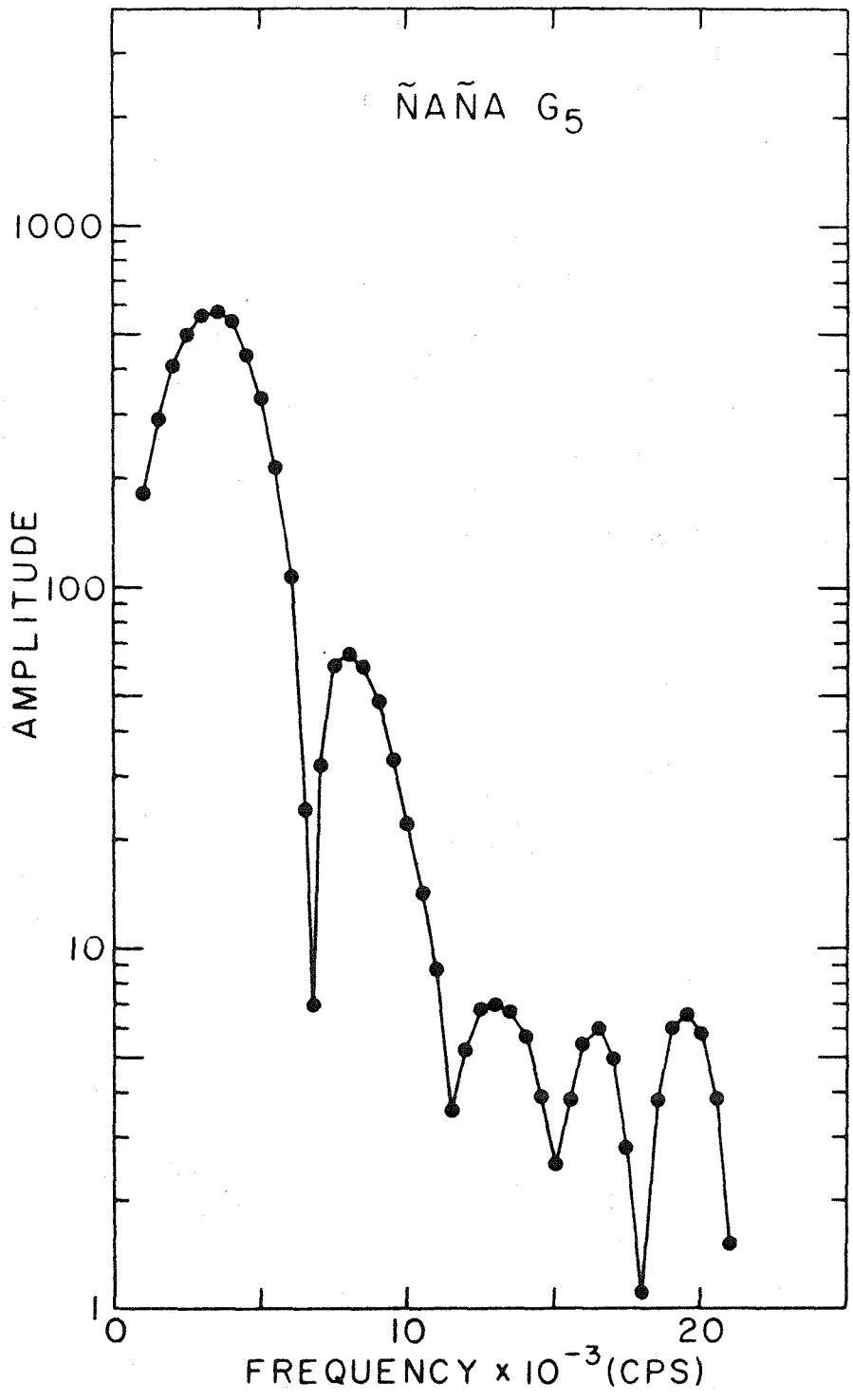

Fig. 34

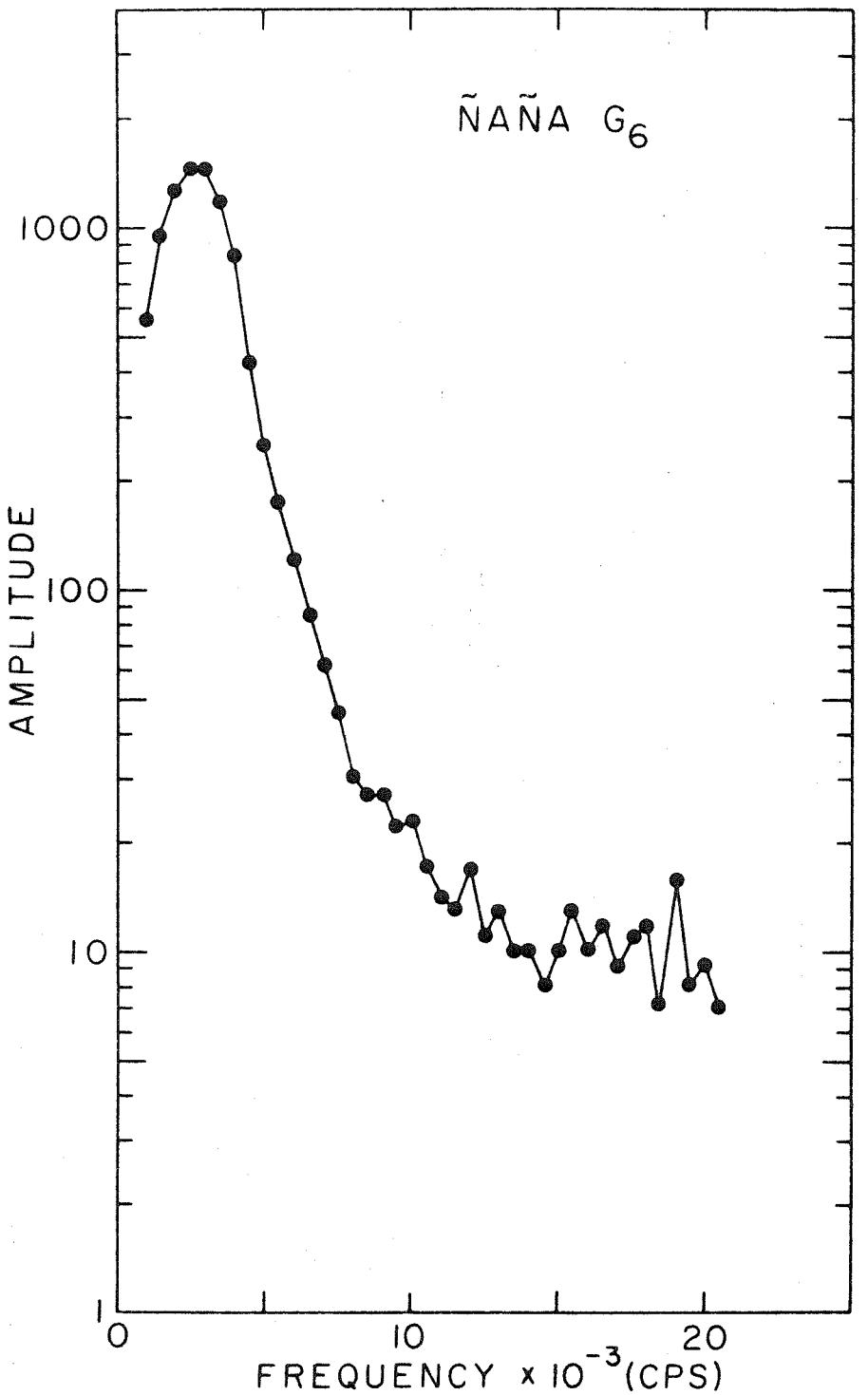

Fig. 35

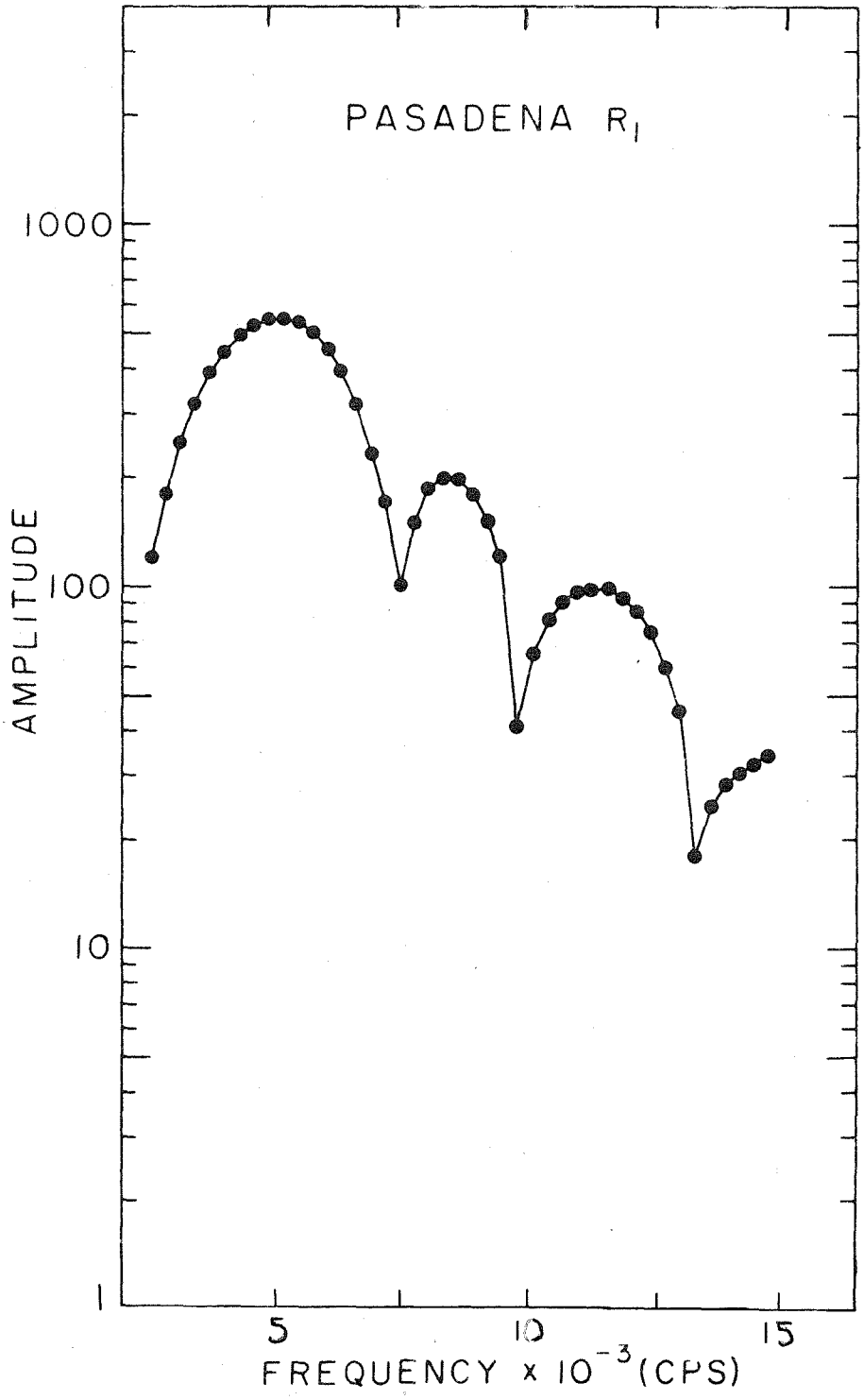
PASADENA R_1
1000
100
10
1
AMPLITUDE
5
10
15
FREQUENCY x 10^{-3} (CPS)

Fig. 36

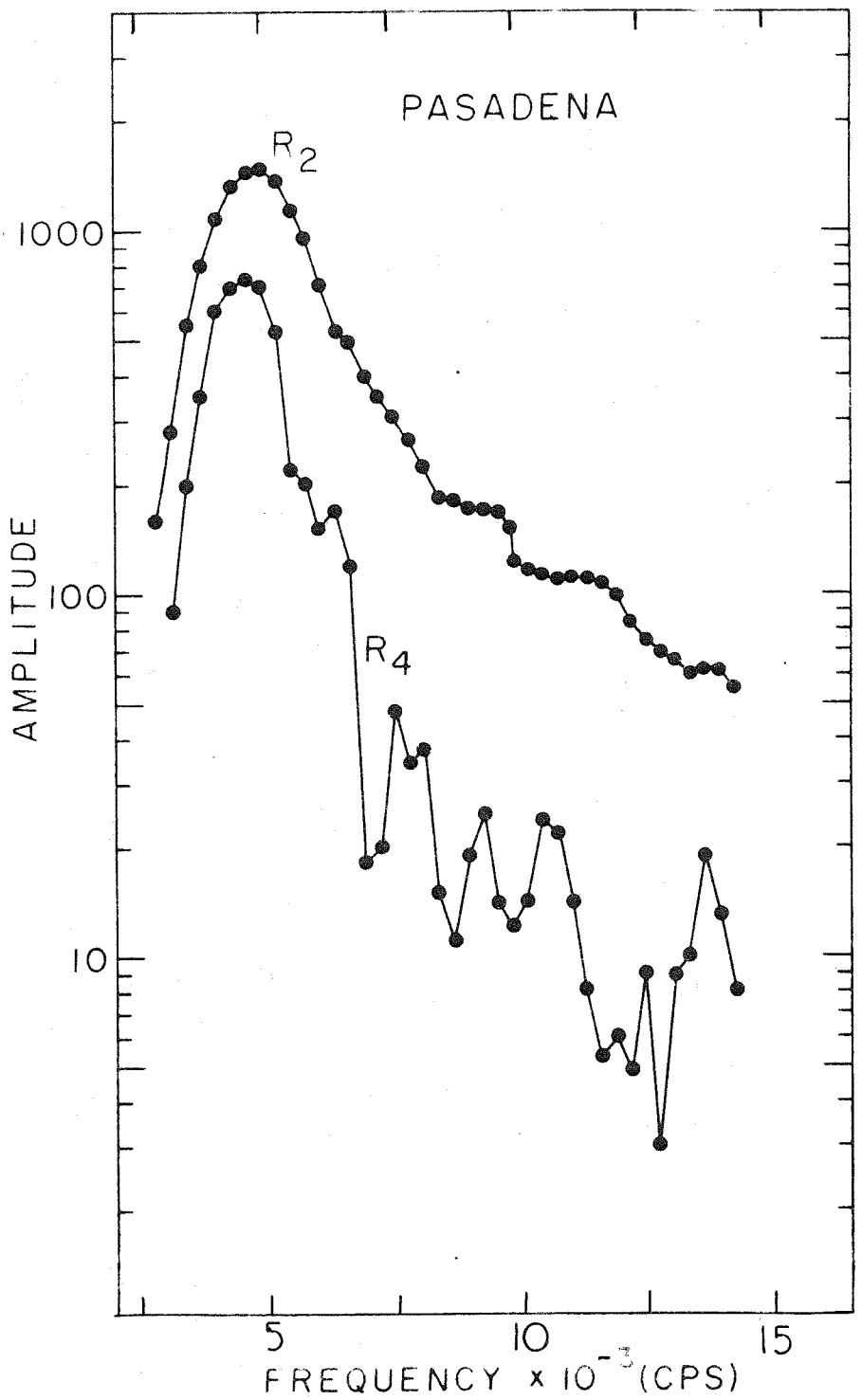
PASADENA
R_2
R_4
1000
100
10
AMPLITUDE
5
10
15
FREQUENCY x 10^{-3} (CPS)

Fig. 37

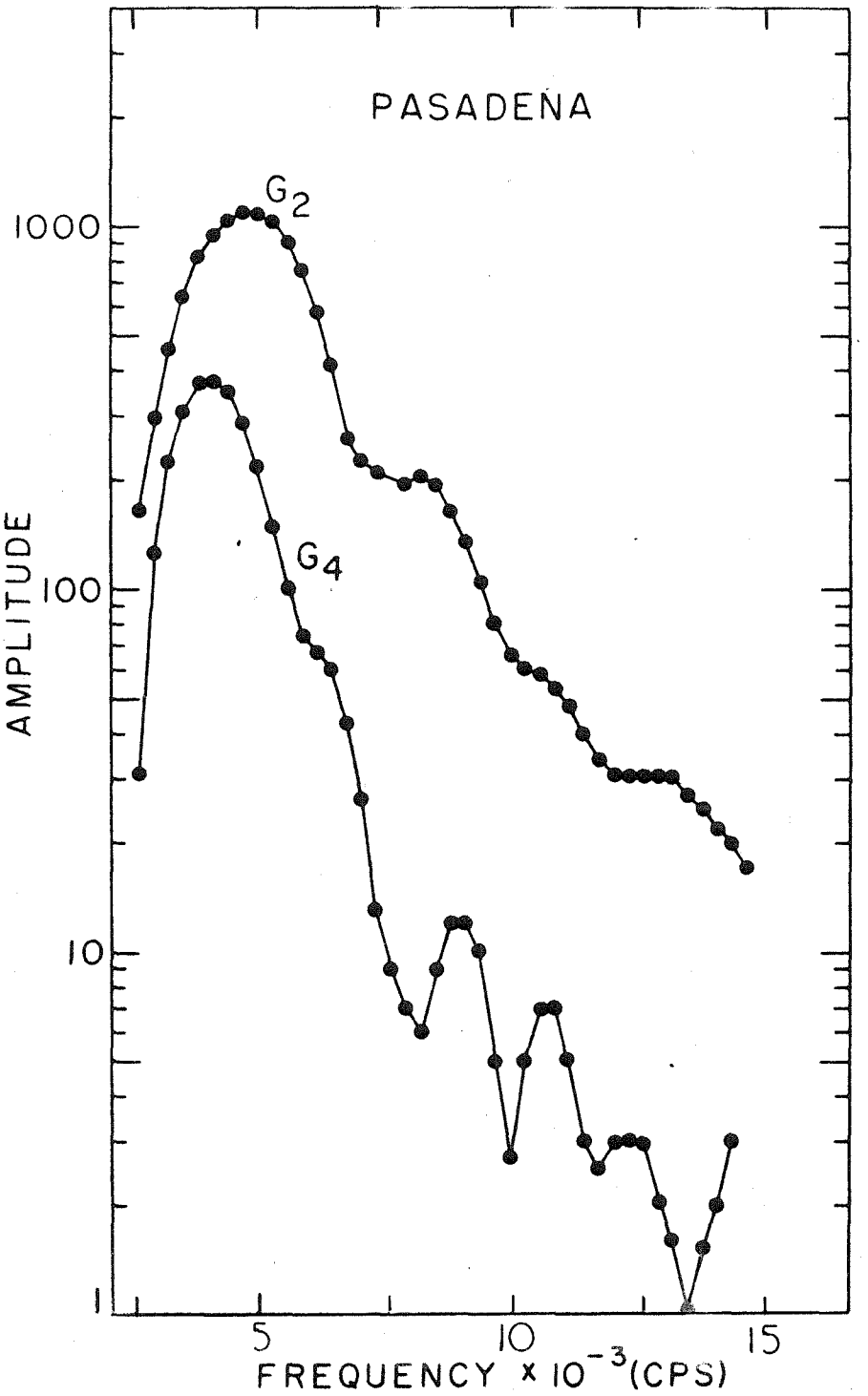
PASADENA
G2
G4
1000
100
10
1
AMPLITUDE
5
10
15
FREQUENCY x 10^-3 (CPS)

Fig. 38

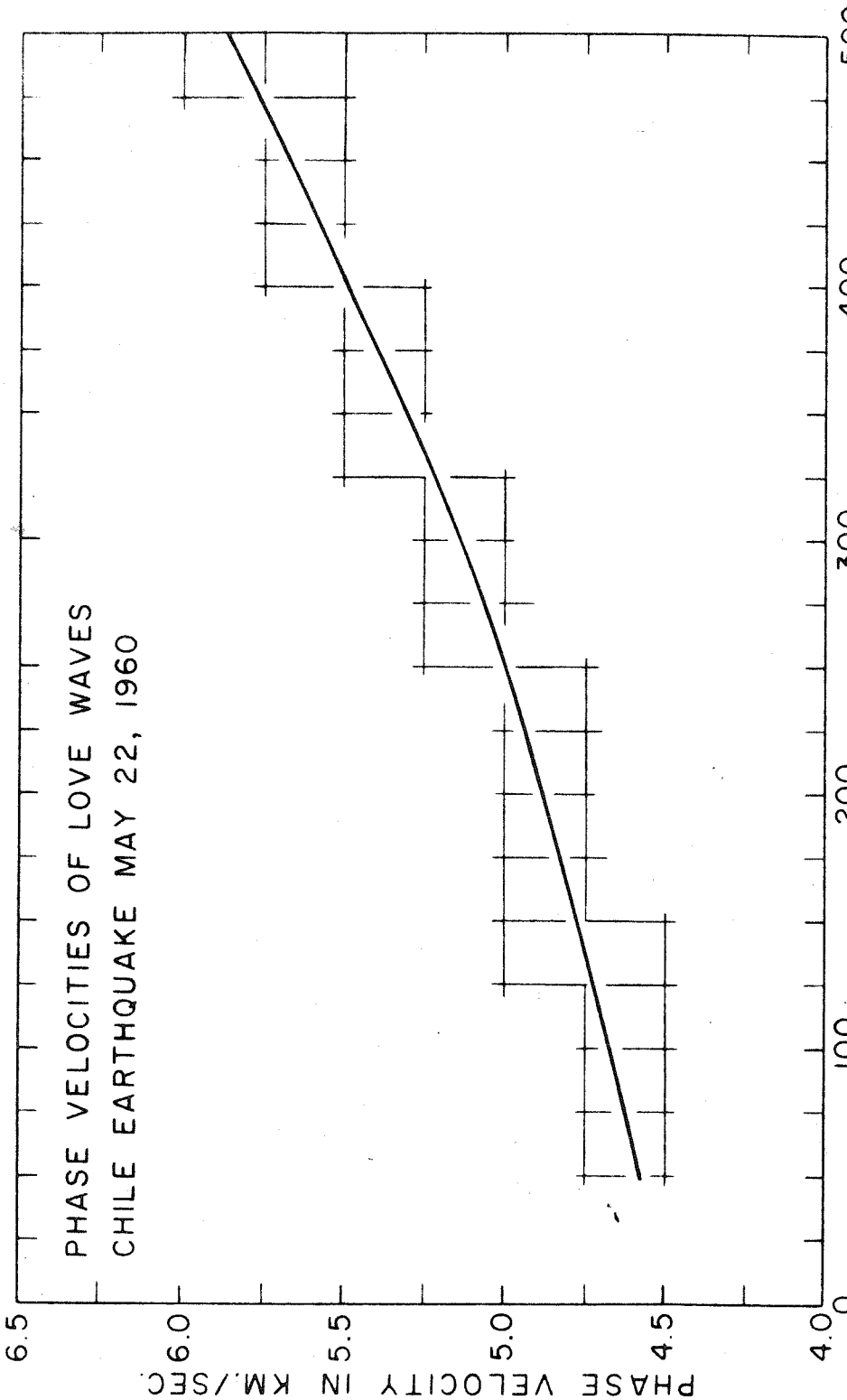
PHASE VELOCITIES OF LOVE WAVES
CHILE EARTHQUAKE MAY 22, 1960
PHASE VELOCITY IN KM./SEC.
6.5
6.0
5.5
5.0
4.5
4.0
0
100
200
300
400
500
PERIOD IN SECONDS

Fig. 39

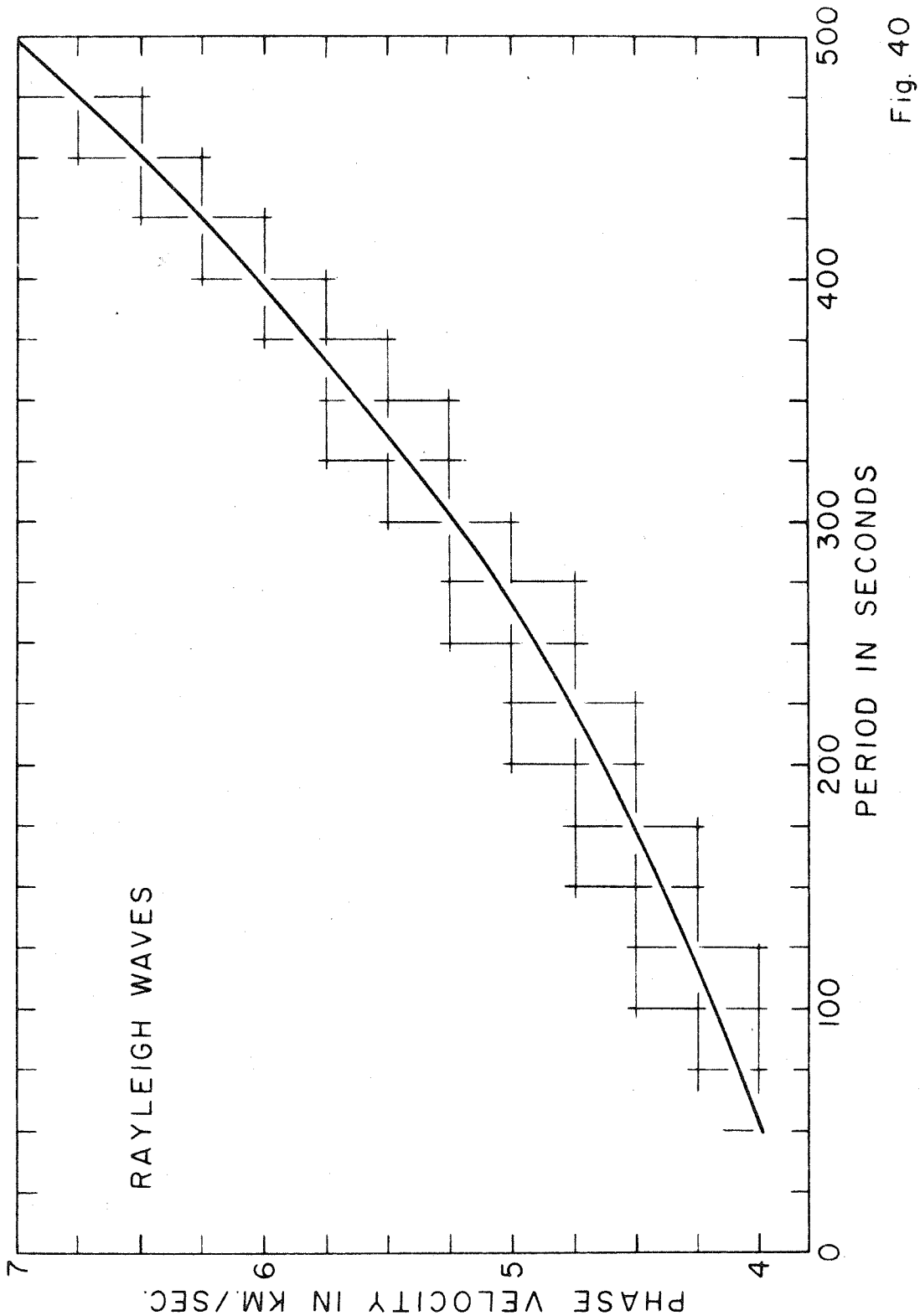
RAYLEIGH WAVES
PHASE VELOCITY IN KM./SEC.
7
6
5
4
0
100
200
300
400
500
PERIOD IN SECONDS

Fig. 40

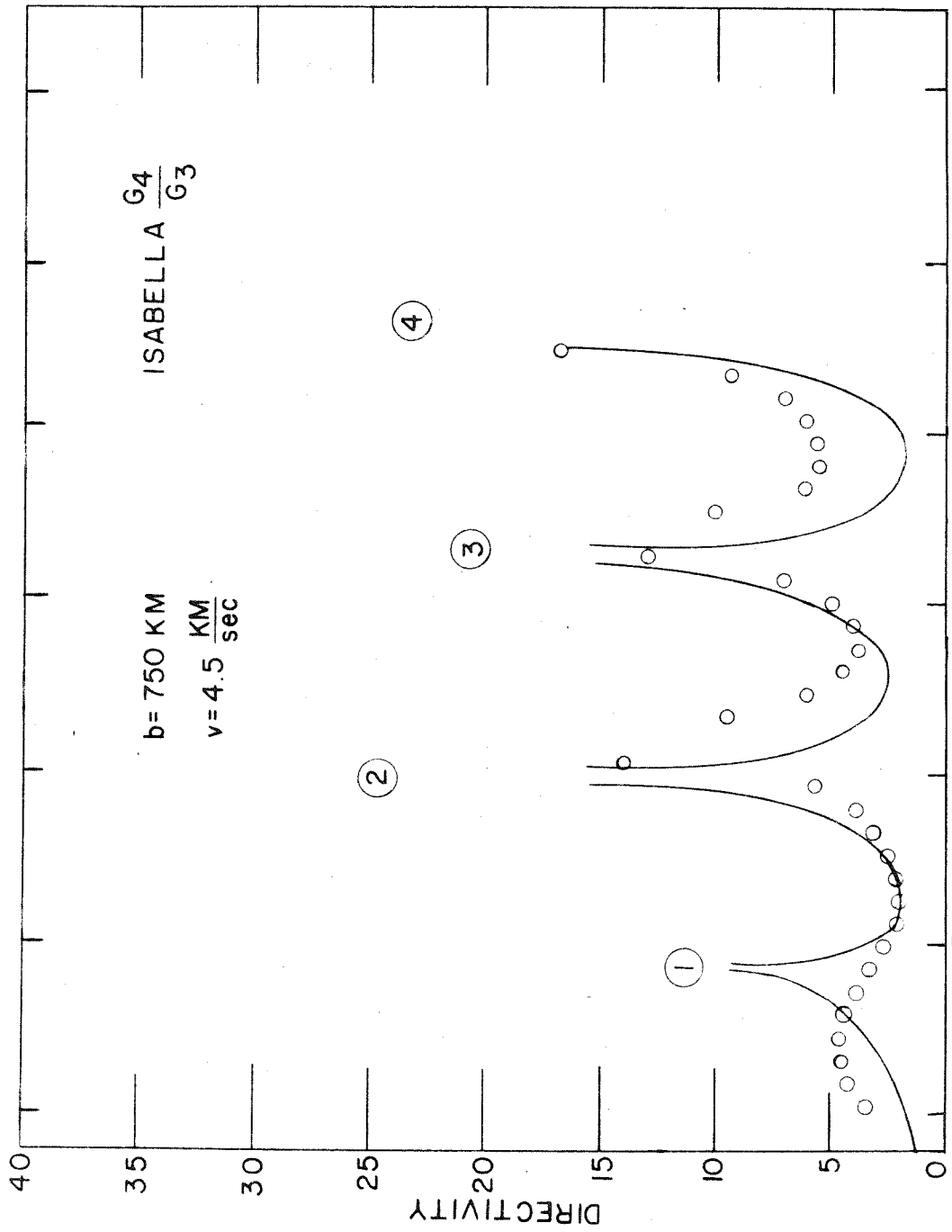
ISABELLA $\frac{G_4}{G_3}$
b= 750 KM
v= 4.5 $\frac{KM}{sec}$
DIRECTIVITY
FREQUENCY x 10^{-3} (CPS)
0
5
10
15
20
25
30
35
40
1
2
3
4

Fig. 41

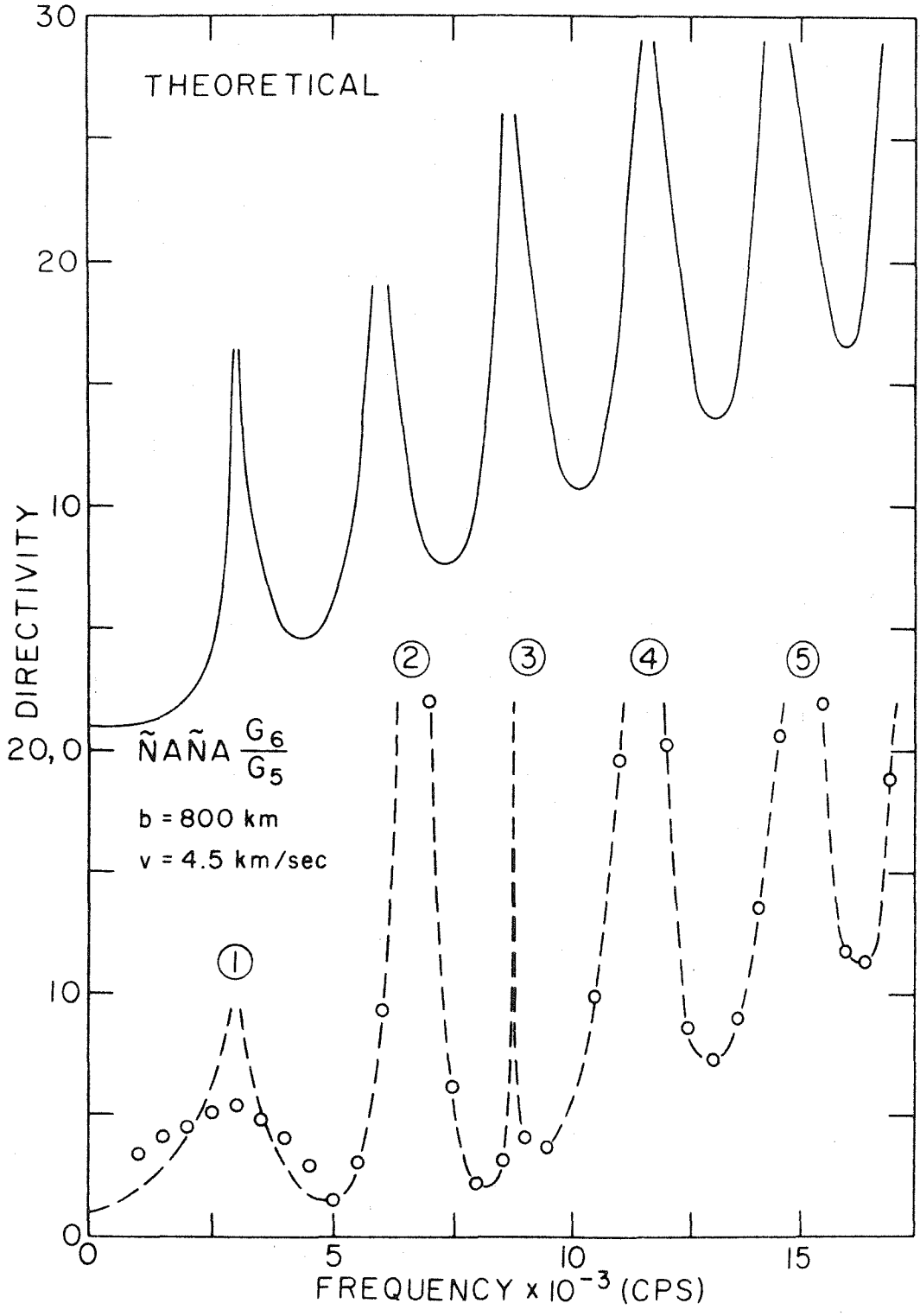
30
20
10
20,0
10
0
0
5
10
15
THEORETICAL
ÑAÑA $\frac{G_6}{G_5}$
b = 800 km
v = 4.5 km/sec
DIRECTIVITY
FREQUENCY x 10^{-3} (CPS)
①
②
③
④
⑤

Fig. 42

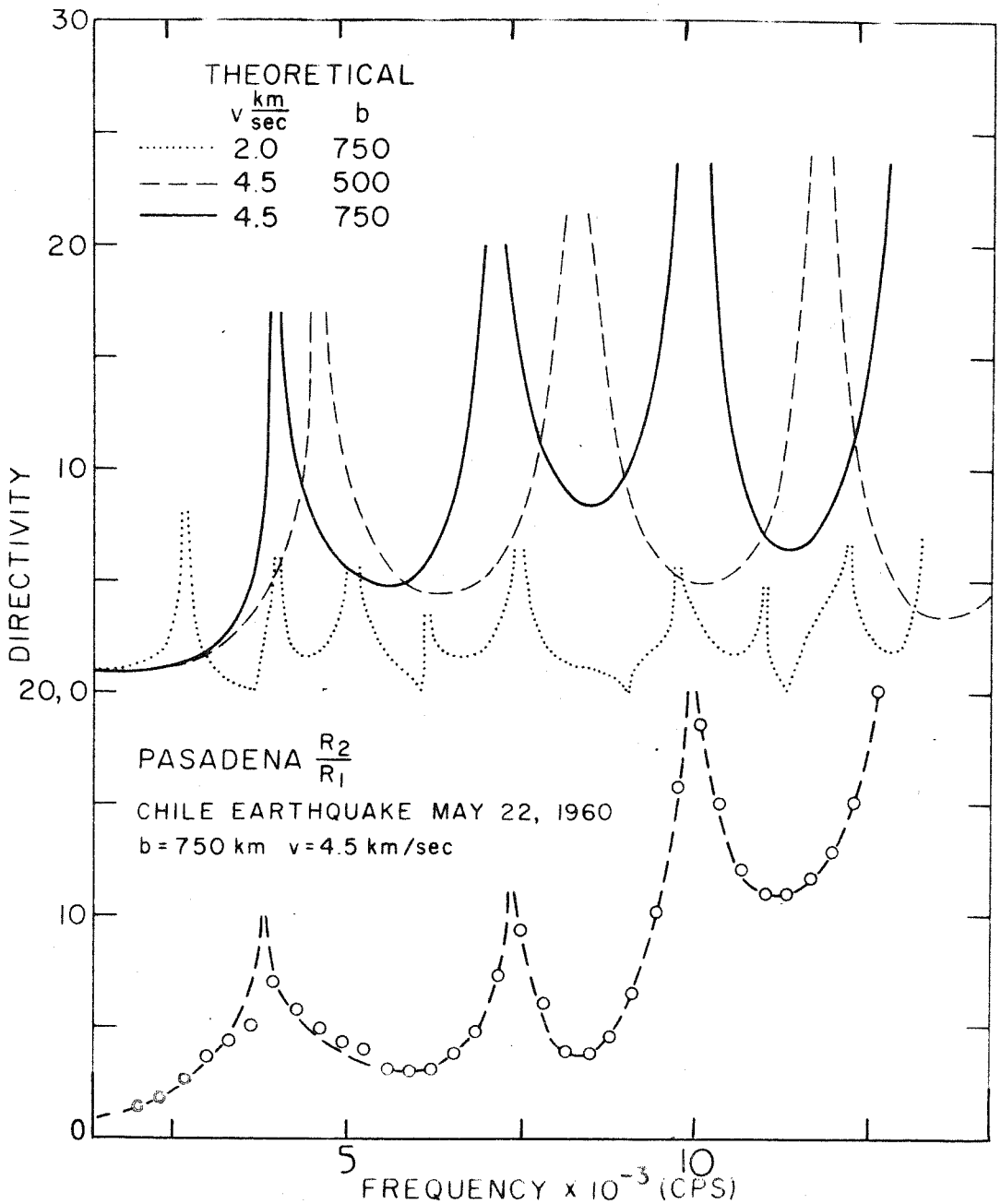
30
20
10
20,0
10
0
DIRECTIVITY
THEORETICAL
v km/sec
b
2.0 750
4.5 500
4.5 750
PASADENA R2/R1
CHILE EARTHQUAKE MAY 22, 1960
b = 750 km v = 4.5 km/sec
5
10
FREQUENCY x 10^-3 (CPS)

Fig. 43

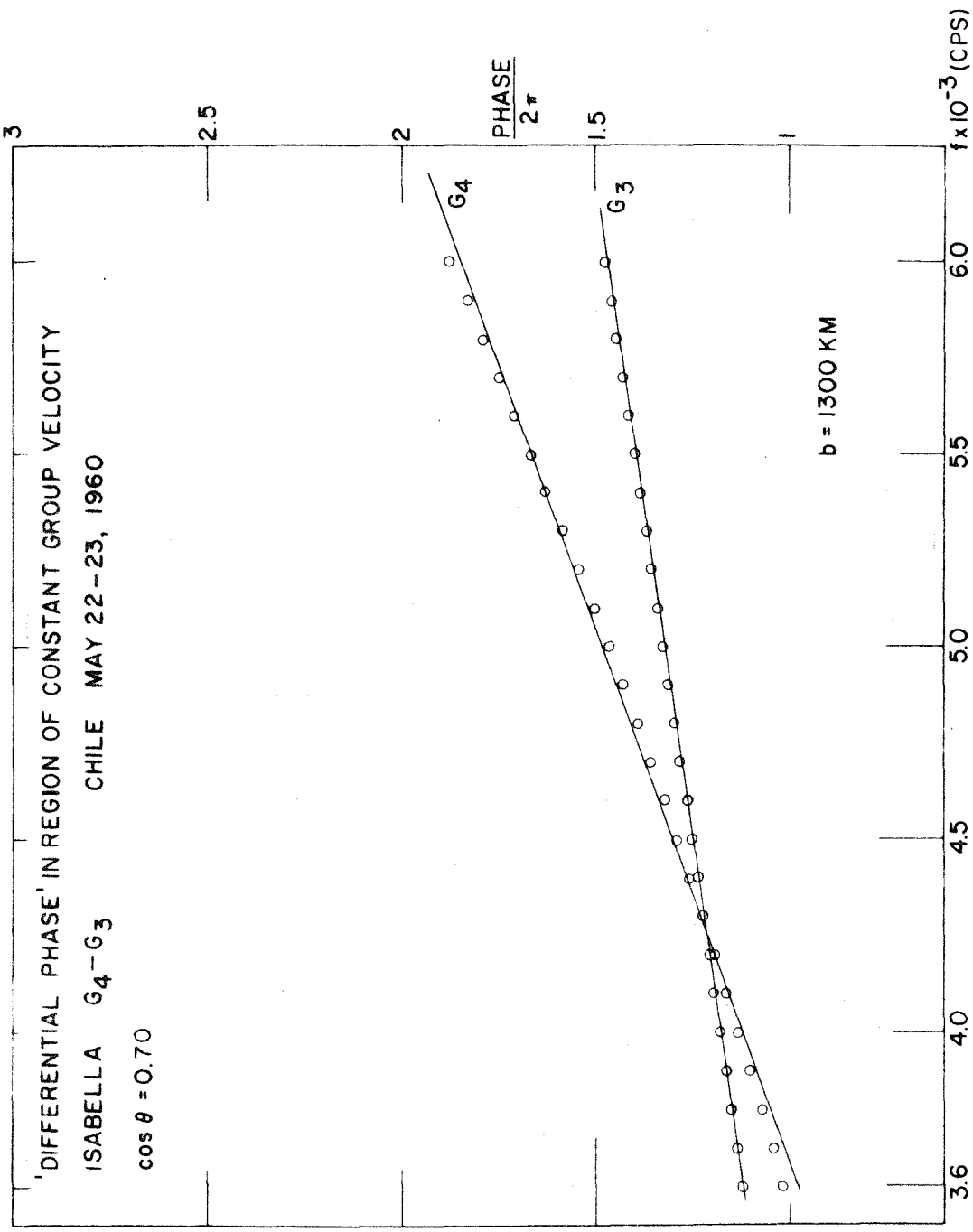
'DIFFERENTIAL PHASE' IN REGION OF CONSTANT GROUP VELOCITY
ISABELLA G_4-G_3 CHILE MAY 22-23, 1960
$\cos\theta = 0.70$
G_4
G_3
b = 1300 KM
PHASE / 2π
3
2.5
2
1.5
1
$f \times 10^{-3}$ (CPS)
T (Sec.)
3.6 4.0 4.5 5.0 5.5 6.0
277.8 250 222.2 200.0 181.8 166.6

Fig. 44

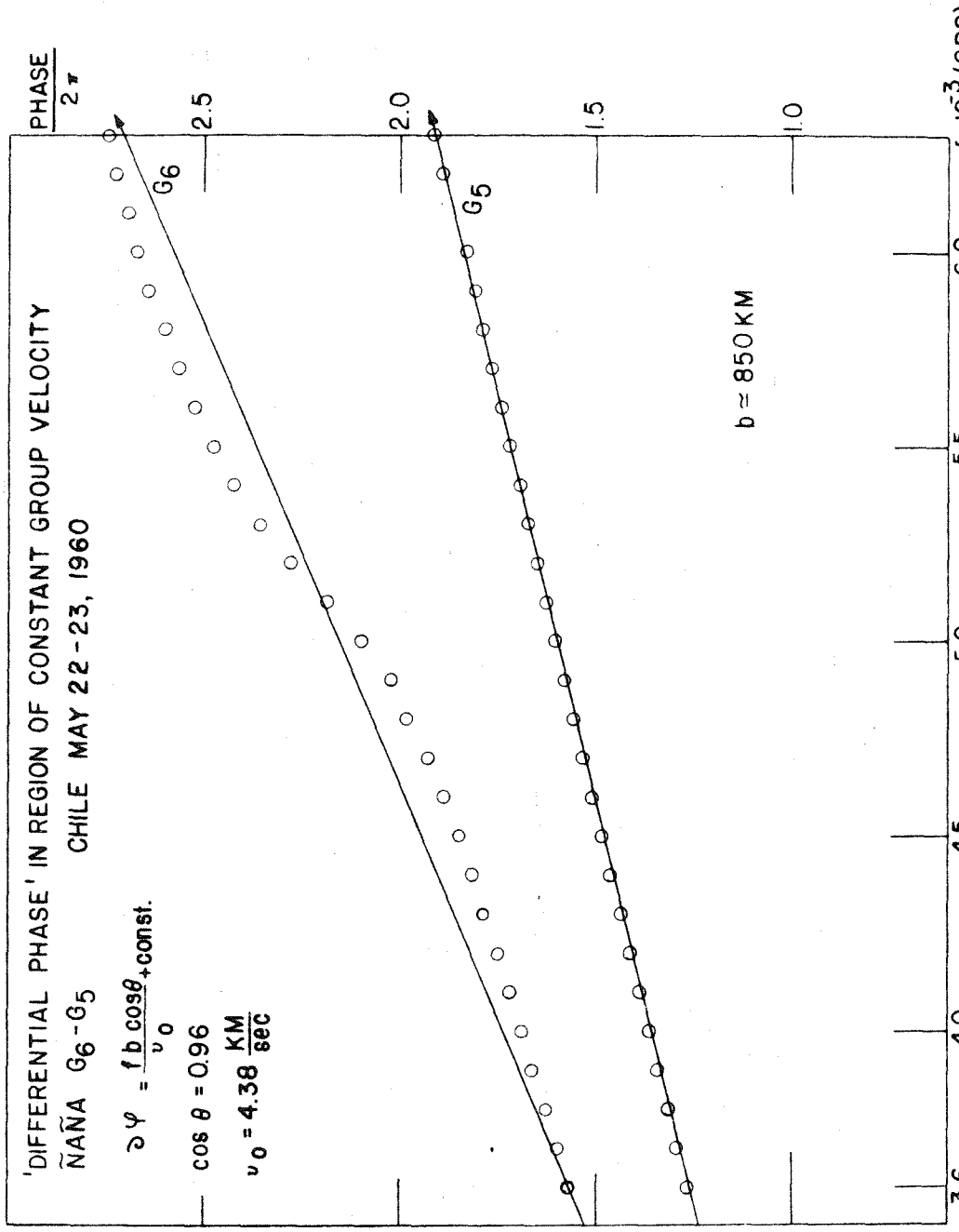
'DIFFERENTIAL PHASE' IN REGION OF CONSTANT GROUP VELOCITY
ÑAÑA G6-G5 CHILE MAY 22-23, 1960
∂φ = f b cosθ/υ0 + const.
cos θ = 0.96
υ0 = 4.38 KM/sec
PHASE/2π
G6
G5
b ≈ 850 KM
2.5
2.0
1.5
1.0
3.6
4.0
4.5
5.0
5.5
6.0
f x10-3 (CPS)
277.8
250
222.2
200
181.8
166.6
T (Sec.)

Fig. 45

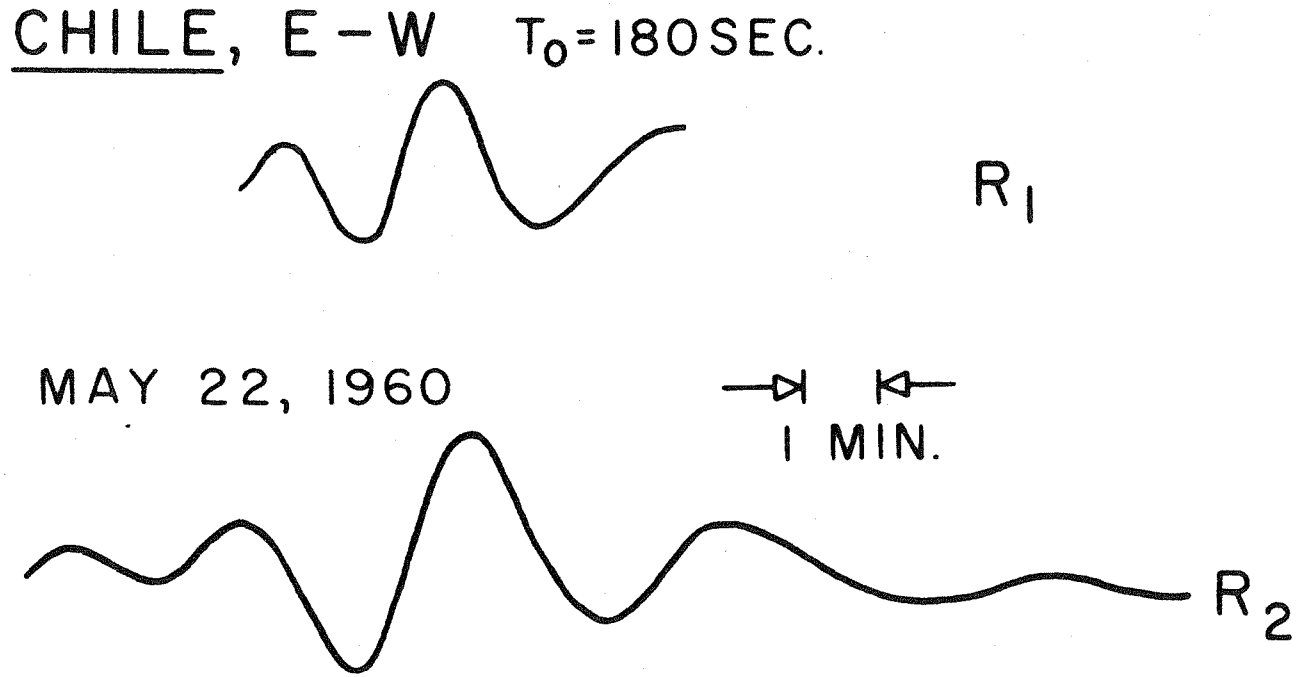

MANTLE RAYLEIGH WAVES
LOW MAGNIFICATION STRAIN

Fig. 46

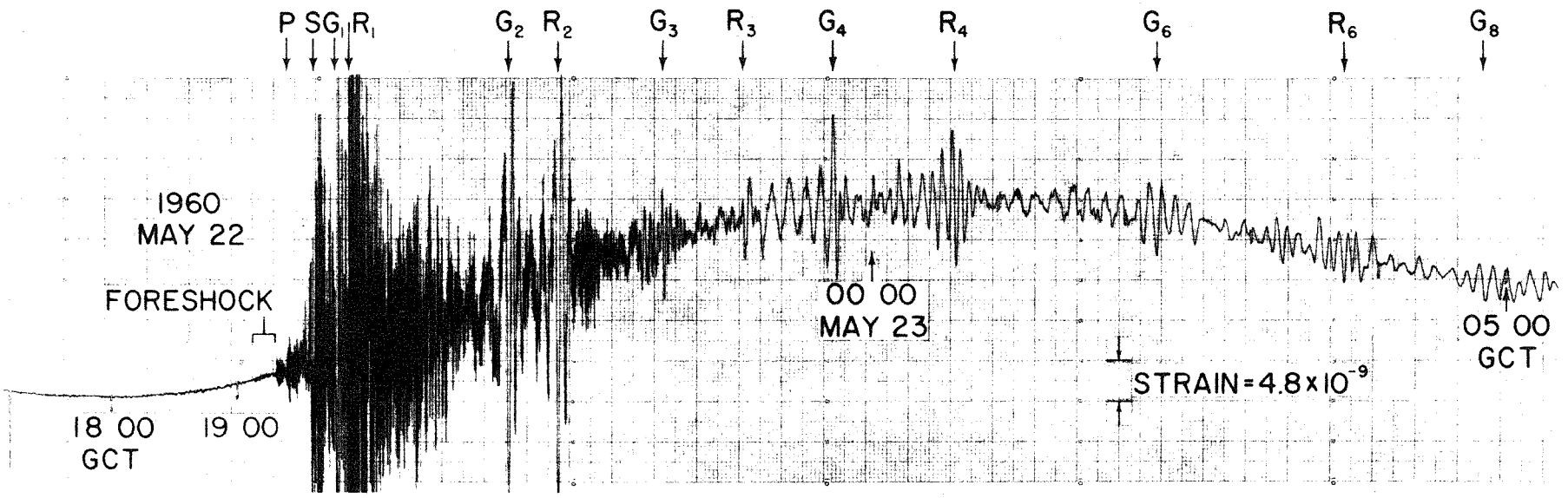

ISABELLA, CALIF. FUSED QUARTZ STRAIN SEISMOGRAPH.

Fig. 47

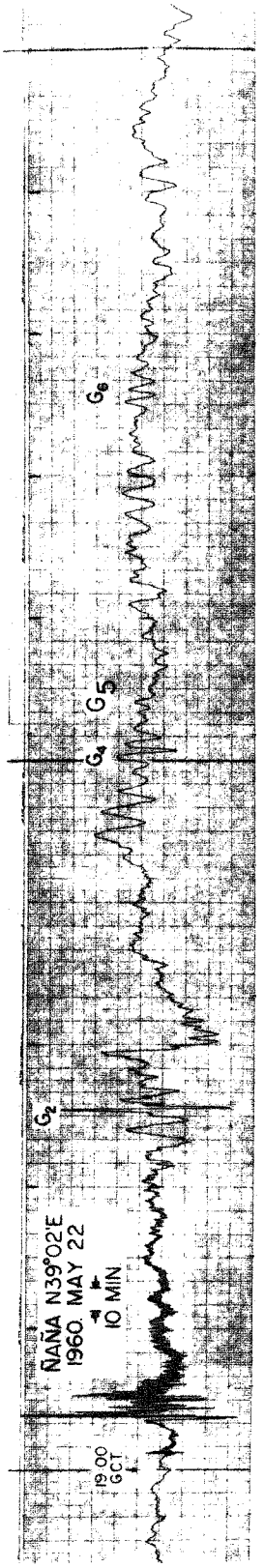

Fig 48

LIST OF SYMBOLS

a_j defined in equation 1-79

b the horizontal extension of the fault-plane

B_m cylinder-function of order m

$$c_1 = c_3 \frac{\sqrt{\gamma^2-1}}{\gamma}$$

$$c_2 = c_3 \frac{\sqrt{\gamma^2-1}}{\gamma^2}$$

$$c_3 = \frac{1}{16} \frac{\gamma}{1 + \frac{1}{3}(\gamma^2-1)^{-\frac{1}{2}}(\gamma^2-\frac{1}{3})^{-\frac{1}{2}}}$$

$$c_4 = c_3 \frac{\sqrt{\gamma^2-\frac{1}{3}}}{\gamma}$$

$$c_1' = c_1 \left(\frac{2}{\pi\gamma}\right)^{\frac{1}{2}}$$

$$c_2' = c_2 \left(\frac{2}{\pi\gamma}\right)^{\frac{1}{2}}$$

$$c_3' = c_3 \left(\frac{2}{\pi\gamma}\right)^{\frac{1}{2}}$$

$$c_4' = c_4 \left(\frac{2}{\pi\gamma}\right)^{\frac{1}{2}}$$

$$c_5' = c_1 \gamma^{\frac{1}{2}}(\gamma^2-1)^{-\frac{1}{2}} C_R^{-\frac{1}{2}}$$

$$c_6' = 2c_1 \pi \gamma^{-\frac{1}{2}} C_R^{-3/2}$$

c extension of the fault in the direction of the y axis

C phase-velocity of a surface-wave

$C_s=\beta$ shear-wave velocity

C_R Rayleigh-wave velocity

C_L Love-wave velocity

$d_1 = \frac{(\gamma^2-1)^{\frac{1}{2}}}{\gamma}$

$d_2 = \frac{(\gamma^2-\frac{1}{3})^{\frac{1}{2}}}{\gamma}$

D_L defined in equation 2-7

D the Directivity-function

$E_1 = \frac{\gamma^2}{\gamma^2-\frac{1}{2}}$

$E_2 = \frac{\gamma^2-\frac{1}{2}}{(\gamma^2-1)^{\frac{1}{2}}(\gamma^2-\frac{1}{3})^{\frac{1}{2}}}$

$F(K) = (2K^2-K_\beta^2)^2 - 4K^2\left(K^2-K_\alpha^2\right)^{\frac{1}{2}}\left(K^2-K_\beta^2\right)^{\frac{1}{2}}$

f frequency

$g_r(\omega)$ the radial layering-function for the Rayleigh-waves

$g_\theta(\omega)$ the azimuthal layering-function for the Rayleigh-waves

$g_z(\omega)$ the vertical layering-function for the Rayleigh-waves

$G(\omega)$ defined in equation 2-25

$h(h_1,h_2)$ vertical extension of the source measured downward from the free-surface

H vertical extension of a layer on top of a half-space

$H_m^{(1)}$, $H_m^{(2)}$ Hankel-functions of order m

$i = \sqrt{-1}$

j a running index number

J_m Bessel-function of the first kind of order m

K wave-number

K_α longitudinal wave-number in the half-space

K_β shear wave-number in the half-space

K_n n^{th} root of the Rayleigh-wave characteristic equation

$_nK$ n^{th} root of the Love-wave characteristic equation

$K_1 = \frac{\omega}{\beta_1}$ shear wave-number in the layer

$K_2 = \frac{\omega}{\beta_2}$ shear wave-number below the layer

$\vec{L}(L_x, L_y, L_z)$ a simple-force representation of the source

L , $L(\omega)$ magnitude of $\vec{L}$, the source-function

M, m, n integers

N_o defined in equation 2-23

$N_1 = C_1\sqrt{\frac{2\gamma}{\pi(\gamma^2-1)}}$

$N_2 = C_2\sqrt{\frac{2\gamma}{\pi(\gamma^2-1)}}$

$N_3 = C_3\sqrt{\frac{2\gamma}{\pi(\gamma^2-1)}}$

P_n the polar phase-shift of surface-wave of order n

p	a parameter of the source defined in equation 2-31
Q^{-1}	the dimensionless dissipation parameter of the Earth
r, r_o	radial coordinate in the xy-plane
(s,q)	the cartesian components of the wave-number vector
t	time
T	period
(u_x,u_y,u_z)	components of the displacement-vector in cartesian coordinates
(u_r,u_θ,u_z)	components of the displacement-vector in cylindrical coordinates
(U_r,U_θ,U_z)	the integrated Rayleigh-wave displacement
$(U_r,U_\theta,0)$	the integrated Love-wave displacement
U_g	group-velocity
U_o	a constant value of the group-velocity
U_m	a stationary value of the group-velocity
v, v_f	the rupture-velocity
x,y,z	cartesian coordinates
ζ	a complex number
$\alpha_1 = \sqrt{\frac{1}{\beta_1^2} - \frac{1}{c_L^2}}$	
$\alpha_2 = \sqrt{\frac{1}{c_L^2} - \frac{1}{\beta_2^2}}$	
$\bar{\alpha}$	defined in section 2.6

α dilatational velocity in the half-space

$\alpha_o = 6.10^{-4}\ \text{sec}^{-1}$

β shear-velocity in the half-space

β_1 shear-velocity in the layer

β_2 shear-velocity below the layer

$\overline{\beta}$ defined in section 2.6

$\gamma = \frac{1}{2}\sqrt{3+\sqrt{3}} = 1.087664$

Γ_o the radius of the Earth

$\delta(t)$ the Dirac delta-function

δ dip angle

δ_o the initial phase

Δ_n distance along a great circle travelled by a surface-wave of order n

$_mF_o(K_n)$ defined in equation 1-83

$\zeta = \frac{\mu_2}{\mu_1}$

$Z_R = \frac{\omega c}{2C_R} \sin\theta_o$ $\qquad Z_L = \frac{\omega c}{2C_L} \sin\theta_o$

η integration-variable in the y-direction

θ, θ_o polar angle on the free-surface

ϑ defined in equation 1-32

Θ defined in equation 2-30

Θ_1, Θ_2 defined in equation 1-55

$\bar{\lambda}$ Lame parameter

λ wave length

Δ_1^R, Δ_2^R defined in equation 1-76

Δ_1^L, Δ_2^L defined in equation 2-20

μ rigidity in the half-space

μ_1 rigidity in the layer

μ_2 rigidity below the layer

$\nu = \sqrt{K^2 - K_\alpha^2}$ $\qquad \nu' = \sqrt{K^2 - K_\beta^2}$

$\nu_1 = \sqrt{K^2 - K_1^2}$ $\qquad \nu_2 = \sqrt{K^2 - K_2^2}$

ξ integration-variable in the x direction

σ extension of fault-plane in the y-direction

τ defined in equation 2-29

$\gamma = \frac{\omega b}{2c_R} \cos \theta_o$

φ_n defined in equation 3-7

φ_R defined in equation 1-41

φ_L defined in equation 2-19

$\partial_1 \varphi$ differential-phase of the first order

$\partial_2 \varphi$ differential-phase of the second order

$\phi_{1,2}$ longitudinal potential function

$\chi = tg^{-1} \frac{q}{s}$

$X_R = \frac{\omega b}{2C_R} \left(\frac{C_R}{v} - \cos \theta_o\right)$ $\qquad$ $X_L = \frac{\omega b}{2C_L} \left(\frac{C_L}{v} - \cos \theta_o\right)$

Ψ_R defined in equation 1-52

$\vec{\Psi}$ vector-potential function

Ω defined in section 2.6

ω (ω_1, ω_2) angular frequency

$\bar{\omega}$ average value of over a spectral-window

$$\gamma_1 = \frac{\gamma^2}{\gamma^2 - \frac{1}{2}} \sqrt{\frac{\gamma^2 - 1}{\gamma^2 - \frac{1}{3}}} = 0.8038$$

$$\gamma_2 = \frac{\gamma^2 - \frac{1}{2}}{\gamma^2 - \frac{1}{3}} = 0.8003$$

$\bar{\gamma}_L$ Love-wave absorption-coefficient

$\bar{\gamma}_R$ Rayleigh-wave absorption-coefficient

Q_1^R, Q_2^R Defined in equation 1-67

Q_1^L, Q_2^L Defined in equation 2-15, 2-16

τ_R, τ_L Defined in equation 1-68, 2-14

$\bar{\sigma}$ Dimension of fault in the dip direction (figs. 6, 22)

REFERENCES

1. Lamb, H. 1916. On waves due to a travelling disturbance. Phil. Mag., V 13, pp. 386-399, pp. 539-548.

2. Sezawa, K. 1929. Generation of Rayleigh-waves from a sheet of internal sources. Bull. Earth. Res. Inst., Tokyo University, V. 7, pp. 417-435.

3. Knopoff, L. and F. A. Gilbert. 1959. Radiation from a strike-slip fault. Bull. Seis. Soc. Amer., V. 49, pp. 163-178.

4. Yanovskaya, T. B. 1958. On the determination of the dynamic parameters of the focus hypocenter of an Earthquake from records of surface waves, I. Izv. Geophys. Ser., pp. 289-301.

5. Morse, P. M. and H. Feshbach. 1953. Methods of Theoretical Physics, part II. McGraw-Hill Book Company, New York.

6. Ewing, M., W. Jardetzky and F. Press. 1957. Elastic waves in layered media. McGraw-Hill Book Company, New York

7. Sneddon, J. 1950. Fourier Transforms. McGraw-Hill Book Company, New York.

8. Pekeris, C. L. 1955. The seismic surface pulse. Proc. Nat. Acad. Sci., V 41, pp. 469-470.

9. Ryshik, I. M. and I. S. Gradstein. 1957. Tables of series, products and integrals. Veb Deutscher verlag der Wissenschaften, Berlin.

10. Benioff, H. 1955. Mechanism and strain characteristics of the white wolf fault as indicated by after-shock sequence. Calif. Dept. Nat. Resources, Div. Mines, Bull. 171, pp. 199-202.

11. Gutenberg, B. 1955. Magnitude determination for larger Kern County shocks 1952. Effects of station azimuth and calculation methods. Calif. Dept. Nat. Resources, Div. Mines, Bull. 171, pp. 171-175.

12. Pekeris, C. L. 1948. Theory of propagation of explosive sound in shallow water. Geol. Soc. Amer. Memoir 27.

13. Newlands, M. 1954. Lamb's problem with internal dissipation I. Jour. Acou. Soc. Amer., V. 26, pp. 434-448.

14. Gutenberg, B. and C. F. Richter. 1934. On seismic waves. First paper, Ger. Beit zur Geoph., V. 43.

14a. Gutenberg, B. and C. F. Richter. 1936. On seismic waves. Third paper, Ger. Beit zur Geoph., V. 47.

15. Benioff, H. 1958. Long waves observed in the Kamchatka Earthquake of November 4, 1952. Jour. Geoph. Res., V. 63.

16. Sato, Y. 1958. Attenuation, dispersion and the wave-guide of the G-wave. Bull. Seism. Soc. Amer., V. 48, pp. 231-251.

17. Press, F. 1959. Some implications on Mantle and Crustal structure from G-waves and Love-waves. Jour. Geophys. Res., V. 64, pp. 565-568.

18. Gutenberg, B. 1959. The asthenosphere low-velocity layer. Annali di Geofisica, V. 12, pp. 439-460.

19. Aki, K. 1960. Study of Earthquake mechanism by a method of phase equalization. Jour. Geophys. Res., V. 65, pp. 729-740.

20. Harkrider, D. 1960. Private communication.

21. Brune, J. N. 1961. Radiation pattern of Rayleigh waves from the southeast Alaska Earthquake of July 10, 1958. Symposium on fault plane studies (in press).

22. Brune, J. N., J. E. Nafe and L. E. Alsop. 1961. Polar phase shift of surface waves on a sphere (in press).

23. Yanovskaya, T. B. 1958[a]. The dispersion of Rayleigh waves in a spherical layer. Izv. Geophys. Ser., pp. 801-817.

24. St Amand, P. 1961. Private communication to Dr. Frank Press.

25. Benioff, H., F. Press and S. Smith. 1961. Excitation of the free oscillations of the Earth by Earthquakes. Jour. Geophys. Res., V. 66, pp. 605-619.

26. Healy, J. H. and F. Press. 1960. Two-dimensional seismic models with continuously variable velocity-depth and density functions. Geophysics, V. 25, No. 5.